Australian National University

Doctoral Thesis

Complex polarization manipulation with dielectric metasurfaces

---

By:
Shaun Lung

A thesis submitted in fulfillment of the requirements for the degree of Doctor of Philosophy

in the

ARC Centre of Excellence for Transformative Meta-Optical Systems
Department of Electronic Materials Engineering

July 18, 2022

Declaration of Authorship

I, Shaun Lung, declare that this thesis titled, "Complex polarization manipulation with dielectric metasurfaces" and the work presented in it are my own. I confirm that:

- This work was done wholly or mainly while in candidature for a research degree at this University.
- Where any part of this thesis has previously been submitted for a degree or any other qualification at this University or any other institution, this has been clearly stated.
- Where I have consulted the published work of others, this is always clearly attributed.
- Where I have quoted from the work of others, the source is always given. With the exception of such quotations, this thesis is entirely my own work.
- I have acknowledged all main sources of help.
- Where the thesis is based on work done by myself jointly with others, I have made clear exactly what was done by others and what I have contributed myself.

Signed:

Date:

AUSTRALIAN NATIONAL UNIVERSITY

Abstract

Research School of Physics
Department of Electronic Materials Engineering

Doctor of Philosophy

Complex polarization manipulation with dielectric metasurfaces

by Shaun Lung

Metasurfaces are an important, developing part of modern optics. They consist of surface structures designed to shape the incident light beams through arrays of sub-wavelength nano-resonators. In this thesis, I focus on the manipulation and sensing of classical and quantum light using dielectric metasurfaces, comprising of dielectric materials such as amorphous silicon on glass. Dielectric metasurfaces are of exceptional interest due to the minimal material losses as compared to their plasmonic counterparts, for which material losses are an intrinsic part. In particular, polarization of light is of great interest in many aspects of both quantum and classical experiments, extending itself to uses such as communication, quantum communication, and quantum computation, and oft times, particular polarization manipulations are implemented using mechanically complex, space-intensive bulk optics. This is problematic for cases demanding high precision and compactness, such as fundmental quantum optical experiments, space-based installations, and quantum communications. It is thus that in the course of this thesis, I explore a fundamentally new form of polarization manipulation using metasurfaces. This new polarization manipulation concept is known as complex birefringence, and is capable of performing heretofore impossible forms of polarization transformation in a single, monolithic structure. Throughout this thesis, I develop an analytical framework utilizing an optimally minimal amount of loss, and explore it through experimental and numerical methods that this concept can implement truly arbitrary control over polarization in classical and quantum cases, and further demonstrate that this concept may be extended to a new form of polarization monitoring that allows for rapid and highly sensitive response. Finally, I extend similar concepts to the concept of singleshot polarimetry, overcoming challenges that previous approaches had considered fundamental weaknesses.

Acknowledgements

To my parents, Lung Yaw Wuu, and Fiona Lung, without whom I would not be the person I am today: Thank you. Your love and support has brought me here, to where I am today, and I could not have done it without you. To my friends, thank you. You've helped keep my spirits up as I continued through my PhD, and at times, distracted me when it was necessary. Without any of you, I would not have made it through.

Thank you, Prof. Andrey A. Sukhorukov. As my primary supervisor, you have never been anything less than fully supportive and willing to help me learn, even when I made mistakes and came up short. Your uncompromising pursuit of excellence and guidance has been an example for me to follow, and I am deeply grateful for all the help and support that you've given me.

Thank you, Prof. Dragomir Neshev. Your leadership and superb management of the experimental group have only allowed my work to flourish. The mutual respect and support that you have cultivated created an ideal atmosphere for me to work free of stress, and I have only benefited from my time with the group.

And to all of my collaborators and colleagues, thank you. Kai Wang, Jihua Zhang, Matthew Parry, Khosro Z. Kamali, Sergey Kruk, Mohsen Rahmani, Frank Setzpfandt, to name but a few, not to mention the myriad people who I have worked with and learned from over the course of my PhD. From each and all of you, I have learned something, and it has been an eye-opening experience.

List of Publications

[1] Shaun Lung, Kai Wang, and Andrey A Sukhorukov. "Complex Birefringence with Dielectric Metasurfaces for Unconventional Polarisation Control". In: *CLEO: Applications and Technology*. Optical Society of America. 2018, JW2A–99.

[2] Shaun Lung, Kai Wang, Khosro Zangeneh Kamali, Mohsen Rahmani, Dragomir N Neshev, and Andrey A Sukhorukov. "Complex-birefringent waveplates with metasurfaces (Conference Presentation)". In: *High Contrast Metastructures VIII*. Vol. 10928. International Society for Optics and Photonics. 2019, p. 109280V.

[3] Nicolas Pedersen, Kai Wang, Shaun Lung, and Andrey A Sukhorukov. "Optimal Single Metagrating for Robust Polarization Measurements". In: *2019 Conference on Lasers and Electro-Optics (CLEO)*. IEEE. 2019, pp. 1–2.

[4] Nicolas Pedersen, Kai Wang, Shaun Lung, and Andrey A Sukhorukov. "Robust Polarimetry with a Single Metagrating". In: *European Quantum Electronics Conference*. Optical Society of America. 2019, eh_2_1.

[5] Shaun Lung, Nicolas RH Pedersen, Kai Wang, Khosro Zangeneh Kamali, Frank Setzpfandt, and Andrey A Sukhorukov. "Optical metagrating for one-shot polarization measurements". In: *SPIE Micro+ Nano Materials, Devices, and Applications 2019*. Vol. 11201. International Society for Optics and Photonics. 2019, p. 1120111.

[6] Andres Vega, Kai Wang, Shaun Lung, Daniel E Jones, Michael Brodsky, Thomas Pertsch, Frank Setzpfandt, and Andrey A Sukhorukov. "Discerning Polarization Objects using Non-local Measurements with Metasurfaces". In: *CLEO: QELS_Fundamental Science*. Optical Society of America. 2020, FM1C–7.

[7] Shaun Lung, Kai Wang, Khosro Zangeneh Kamali, Mohsen Rahmani, Dragomir N Neshev, and Andrey A Sukhorukov. "Arbitrary Transformation of Two-Photon Polarization States with Metasurfaces". In: *2020 Conference on Lasers and Electro-Optics (CLEO)*. IEEE. 2020, pp. 1–2.

[8] Shaun Lung, Jihua Zhang, Kai Wang, Khosro Zangeneh Kamali, Mohsen Rahmani, Dragomir N Neshev, and Andrey A Sukhorukov. "Optimal Monitoring of Deviations from Target Polarization with Metasurfaces". In: *Conference on Lasers and Electro-Optics/Pacific Rim*. Optical Society of America. 2020, C2E_2.

[9] Shaun Lung, Jihua Zhang, Kai Wang, Dragomir N Neshev, and Andrey A Sukhorukov. "Experimental Monitoring of Polarization Perturbations with Metasurfaces". In: *2021 Fifteenth International Congress on Artificial Materials for Novel Wave Phenomena (Metamaterials)*. IEEE. 2021, pp. 232–234.

[10] Shaun Lung, Kai Wang, Khosro Zangeneh Kamali, Jihua Zhang, Mohsen Rahmani, Dragomir N Neshev, and Andrey A Sukhorukov. "Complex-birefringent dielectric metasurfaces for arbitrary polarization-pair transformations". *ACS Photonics* 7.11 (2020), pp. 3015–3022.

[11] Shaun Lung, Jihua Zhang, Kai Wang, Mohsen Rahmani, Dragomir N Neshev, and Andrey A Sukhorukov. "Realtime monitoring of polarization statedeviations with dielectric metasurfaces". *(In preparation)* (2021).

[12] Shaun Lung, Nicolas RH Pedersen, Kai Wang, Frank Setzpfandt, and Andrey A Sukhorukov. "Complex-birefringent dielectric metasurfaces for arbitrary polarization-pair transformations". *(In preparation)* (2021).

Contents

Declaration of Authorship iii

Abstract v

Acknowledgements vii

List of Publications ix

Contents xi

1 Introduction 1
- 1.1 An overview of polarization and metasurfaces . . . 2
- 1.2 Design and fabrication of metasurfaces . . . 9
- 1.3 Scope of thesis . . . 14

2 Complex birefringence 17
- 2.1 Complex birefringence from Singular Value Decomposition . . . 18
- 2.2 Tailored loss for polarization pair transformation . . . 23
- 2.3 Dielectric metasurface design and fabrication . . . 25
- 2.4 Experimental realization of complex birefringence . . . 29
- 2.5 Summary . . . 34

3 Transformation of biphoton states 37
- 3.1 Biphoton states . . . 40
- 3.2 Complex birefringence for transformation of biphoton states . . . 44
- 3.3 Summary . . . 48

4 Polarization monitoring 51
- 4.1 Concept for polarization monitoring . . . 53
- 4.2 Designining metasurfaces for polarization monitoring . . . 55
- 4.3 Experimental demonstration for polarization monitoring . . . 57
- 4.4 Chirality in dielectric metasurfaces . . . 62
- 4.5 Tunable metasurfaces for polarization monitoring . . . 65
- 4.6 Summary . . . 66

5 Robust polarization measurements 69
- 5.1 Theory for single-shot polarimetry . . . 71
- 5.2 Numerical design procedure . . . 75
- 5.3 Robustness of reconstruction . . . 76

5.4 Fabrication 78
5.5 Experimental characterization 79
5.6 Summary 82

6 Conclusion **83**

A Experimental characterization of the metasurface polarization transfer matrix **87**

Chapter 1

Introduction

Light is an utterly fundamental part of the human experience —underpinning our relationship with our life-giving sun, enabling agriculture and civilization, and now powering our world-spanning communications networks. Ever since the first fire was kindled, ways to produce, control, and alter light have been a steadfast pursuit of humanity, from questions as seemingly innocuous as 'why do things look different when underwater' to the colour of the sunset to the entirely *new* aspects of life we have created from the answers; from telescopes, to movies, to X-rays.

Metasurfaces are merely the latest development in this endless exploration. Comprised as they are as arrays of carefully engineered optical resonators on some substrate, they offer unprecedented control over light, governed by extensions of the concept of Mie scattering. First formalized as a solution of the Maxwell equations by Gustav Mie [1], Mie scattering describes the scattering of electromagnetic plane waves by homogenous spheres, arising from induced resonances, and metasurfaces are an extension of this theoretical framework into *designed* materials. And of course, within Mie scattering lies the answer to the brilliant colours of the sunset: Rayleigh scattering, the process by which a sunset gains its distinctive hues, is a close relative to Mie scattering for the scattering of light by particles *much* smaller than the wavelength of the light.

Mie scattering, and its extension into more general forms beyond scattering by a simple sphere, is predicated on the existence of structures with dimensions on the order of the wavelength of incident waves. With the increasing sophistication of semiconductor fabrication, it has become all but trivial to manufacture structures on the scale of nanometers, with $7nm$ transistors already in mass production, and $5nm$ and $3nm$ on the horizon [2]. Considering that the visible range of light spans the $380-750nm$ range, an entire two orders of magnitude above what is possible to manufacture, it becomes clear that Mie scattering and its related forms are readily adapted as tools which we might reach for to manipulate light.

In this thesis, I conceptualize a novel framework with which the manipulation and transformation of light, whether quantum or classical, can be accomplished, and demonstrate through physical experiments that this concept is both practical to implement and applicable to a broad range of usecases in both fundamental research and sensing applications. In particular, I focus on the manipulation of polarization

using a novel concept which has been termed as complex birefringence, implemented via dielectric metasurfaces. This framework is developed first in theory, then through relevant application of experimental characterization and analysis supplemented by numerical simulation as needed.

1.1 An overview of polarization and metasurfaces

Metasurfaces are an important, developing part of modern optics. They consist of surface structures on scales comparable to the wavelength of light designed to control the properties of light incident on them. These structures act as nano-antennas that resonate with incident light to produce varying interactions, the properties of which may be varied by altering their physical properties such as size, shape, and orientation. In particular, recent advances in design and fabrication of all-dielectric metasurfaces, which do not suffer plasmonic losses and are highly transparent in contrast to metallic structures, have led to demonstrations of very efficient polarization manipulation combined with arbitrary phase shaping.

Polarization is a particularly important property of light, one that I will deal with extensively throughout my thesis. Light is, of course, well-known to be a wave having been considered such since the 1600s [3] —its quantum nature is, of course, a more recent realization. A well known feature of waves is their polarization, the property of a wave to oscillate perpendicular to its direction of propagation in isotropic media. Light is, of course, no exception, and the polarization of light sees extensive use in nearly all parts of everyday life, from sunglasses, to the LCD screen you are almost certainly reading this text on, to materials analysis and quality checking of a vast array of manufacturing.

Polarization in light is denoted using the direction of its electric field, typically in terms of its orthogonal components. Interactions with physical media can attenuate, filter, and shift the types of polarization, and in physics, we are familiar with bulk optical components such as polarizers and waveplates, or more generally, phase retarders of various stripes. In Fig. 1.1(a) we see a visualization of unpolarized light filtered to a linear, diagonal polarization, and then rotated into a circular polarization by a quarter-waveplate. Furthermore, an important visualization tool for polarization is the Poincaré sphere, as seen in Fig. 1.1(b), wherein a particular polarization may be represented in terms of its orthogonal basis components, known as the Stokes parameters, as points within a spherical volume, or more commonly, arrows terminating at the respective points. This conveys full information about the polarization state in the *direction* of the point, as well as the degree of polarization in the radius of a given point.

It should be no surprise that polarization has seen consistent interest over the years, whether it be in extending our capabilities or utilizing it to solve an ever-increasing breadth of problems. As such, new ways to control polarization sees equally consistent interest, and in 2001 came arguably the first attempt to

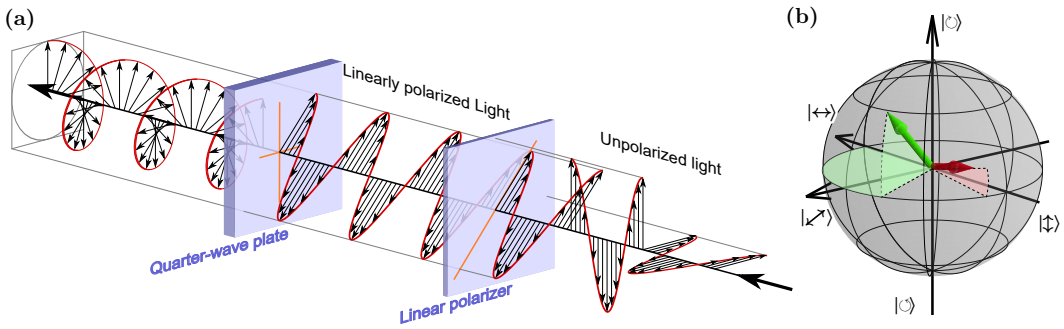

FIGURE 1.1: Polarization and its representation on a Poincaré sphere. (a) Adapted from Wikipedia [4]. A visualization of polarization of light, showing the electric field oscillation of light beginning with unpolarized light (right) that is restricted to a linear polarization, then rotated to a circular polarization. (b) Representations of polarization by arrows within a Poincaré sphere, with polarization properties represented by the radial length, azimuthal, and polar angles. The degree of polarization is represented by the length of the arrow, with fully polarization on the surface of the sphere (green) and partial polarization not reaching the surface (red).

control polarization using sub-wavelength structures. This first attempt, formulated theoretically and demonstrated in experiment, utilized a specific formulation of geometric phase, the Pancharatnam-Berry (PB) phase, as opposed to propagation phase. Geometric phase is the process by which some oscillatory function, such as a light wave, proceeds through an adiabatic cycle and accumulates a phase difference. In modern optics, two familiar examples exist: waveplate arrangements, and fiber paddle polarization controllers. Fiber paddle polarization controllers comprise laser light passed through a single mode optical fiber which is mechanically bent in several locations so as to induce a phase shift in the light exiting the fiber, thus controlling its polarization. This first attempt of polarization control using a grating by Bomzom et al.[5], however, utilized a metallic spiral grating with spatial variance, shown in Fig. 1.2, to convert circularly polarized light to an azimuthally polarized beam. Of course, this was only the beginning.

From gratings, attention turned to arrays comprised of nano-resonators. Comprised of arrays of individual pixels, each of which may be customized to the designer's liking, the nigh-infinite degrees of freedom, in turn, revealed an entirely new design space to explore. Each individual pixel, comprised of an individual nano-resonators (also referred to as nano-antennas) are subwavelength structures resonating with incident light, each one offering individual control over incident light. Analytically, they are best described using Mie theory.

Formulated by Gustav Mie as a solution to Maxwell's solutions, Mie scattering is a crucial part of metasurface design and analysis. While the initial solutions formulated by Mie applied only to scattering by isotropic spheres, the principle may be extended to other shapes, largely through numerical means as opposed to exact

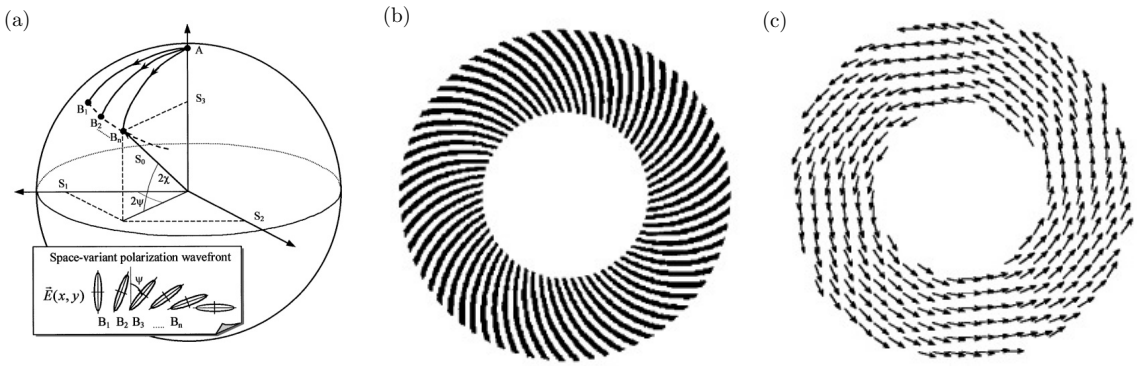

FIGURE 1.2: From Ref. [5]. Berry phase for polarization manipulation. (a) Demonstration of space-variant polarization-state manipulations on a Poincaré sphere. Inset, resultant local polarization ellipse. (b) Magnified geometry of the grating for converting circular polarization into azimuthal polarization and (c) experimental measurement of the local azimuthal angle φ.

analytical solutions due to the practical difficulty of solving the equations involved in complex geometries. By considering a particle as a collection of elementary charges, it is reasonably intuitive that these charges may readily be excited by an incident electromagnetic wave, creating resonances within the structure. These resonances, typically dipolar and confined within the particle, in turn re-radiate the incident electromagnetic wave, and the superposition of these re-radiated waves comprise the scattered light. In Fig. 1.3, we see some examples of these multipolar moments, generated in two classes of material —plasmonic, and dielectric.

These two categories of materials and types of resonances define the two major types of metasurfaces. Plasmonic metasurfaces consist of metasurfaces made out of metallic materials, typically gold or silver, with permittivities $\epsilon < 0$ and structured on a scale on the order of the intended wavelength of light to affect the desired scattering properties. They are characterized by the eponymous surface plasmons, with the resonances confined largely near the surface of the structures. The high negative permitivitty of the component materials are both the strength and the weakness of plasmonic metasurfaces, allowing for *extremely* thin layers to accomplish the same tasks, but coming at a substantial cost of high absorption loss inherent to the material, resulting in a large degree of fundamental loss simply to use these types of metasurfaces [7, 8]. Dielectric metasurfaces, by contrast, utilize materials with near-zero absorption losses and consequently do not suffer from such losses. It is on this latter class of metasurface that my thesis will focus.

Comprised as they are of high-contrast dielectric materials such as amorphous silicon, dielectric metasurfaces have near to zero absorption loss. With positive electric permittivities, they host internal resonances in contrast with the surface plasmons of plasmonics, these internal resonances that afford full phase control in

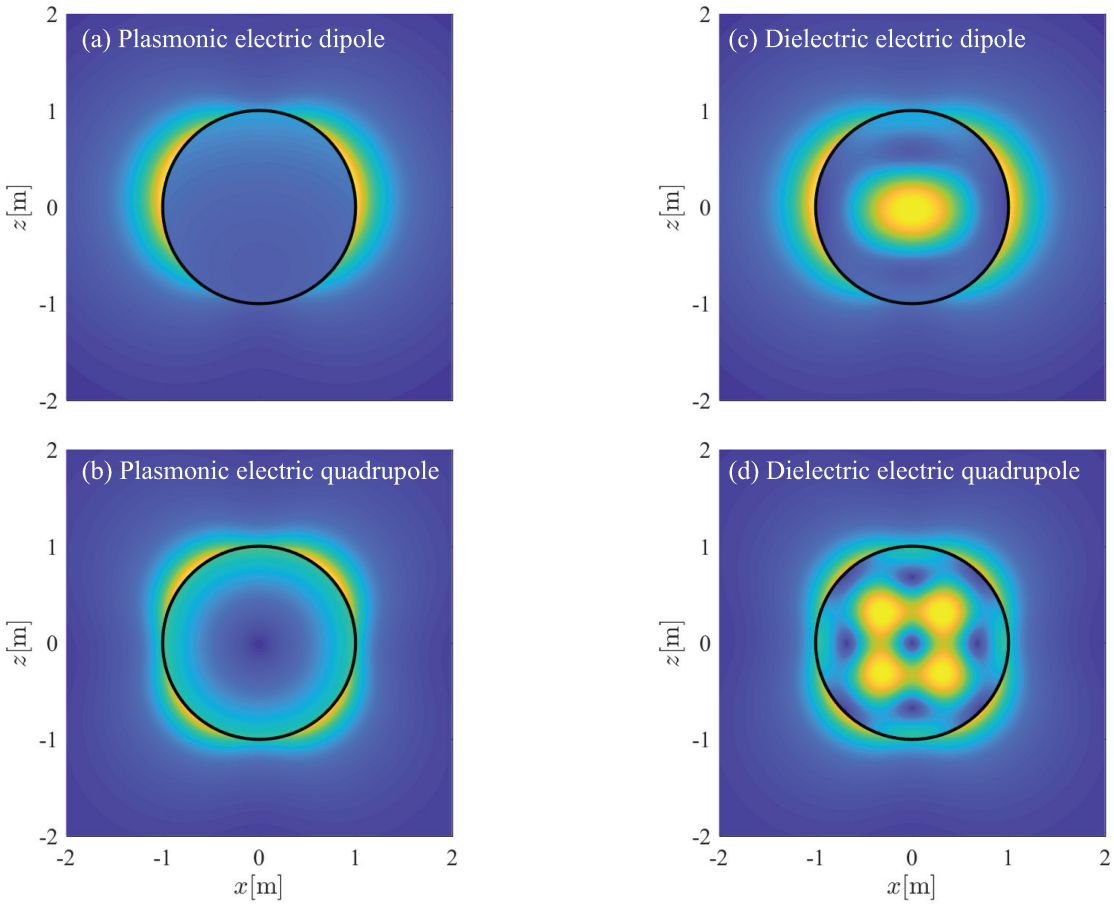

FIGURE 1.3: From Ref. [6]. The amplitude of the near-field electric field distribution for a sphere of radius $r = 0.75$ at: (a) $\epsilon_1 \approx -3.5$; (b) $\epsilon_1 \approx -1.754$; (c) $\epsilon_1 \approx 32.9$; and (d) $\epsilon_1 \approx 57.93$. These resonances correspond to the first two plasmonic and dielectric resonances, i.e., (a,c) dipole and (b,d) quadrupole, respectively. These values are labelled in meters, but may be considered to be in arbitrary units due to the scale-invariance of the Maxwell equations.

transmission [9]. This control arises purely from the resonances of the subwavelength structures, and thus exclusively from structural details of the nano-resonators comprising the metasurfaces. Conventional dielectic metasurfaces comprise of some number of discrete, geometrical nano-resonators arranged on the substrate, and can even include multi-layered structures with non-trivial physical symmetries.

Subsantial interest in the use of machine learning networks and blackbox optimization techniques have also delved into the use of periodic but highly nontrivial geometries implemented as dielectric structures with which to manipulate light [10]. These are inevitably designed using computational simulations and numerical, adjoint-based approaches collectively known as topological optimization, resulting in extremely non-intuitive geometries and dynamics[11]. Such topologically optimized metasurfaces allow for the exploration of previously inaccessible design

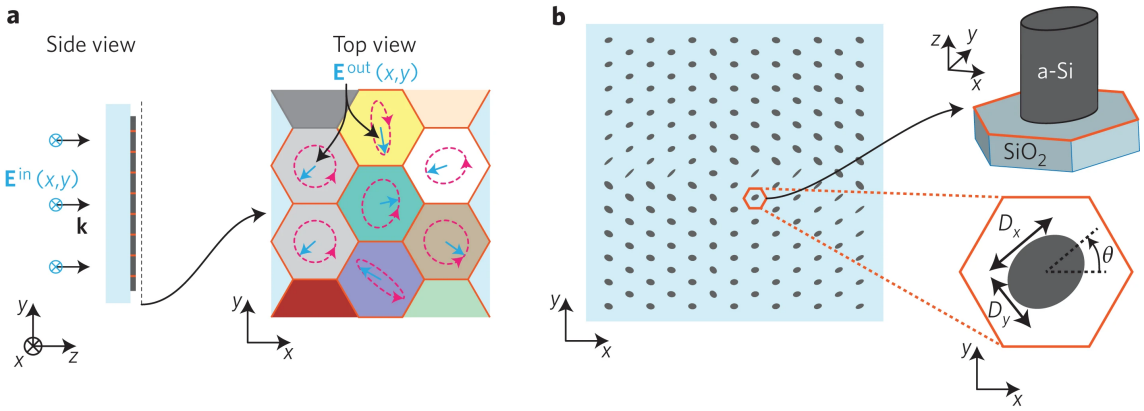

FIGURE 1.4: From Ref. [9]. Representative figure of metasurfaces. (a) Schematic side and top views of a metasurface utilizing hexagonal unit cells. The incident electromagnetic wave $\mathbf{E}^{in}$ resonates with each unit cell according to the (b) physical parameters D_x, D_y, θ of the elliptic cylinder resonators. The metasurface shown schematically has inhomogenous pixel shapes, thus resulting in varying alterations to the transmitted light $\mathbf{E}^{out}$, according to each individual pixel.

spaces, allowing in particular relatively easy design of multi-functional metasurfaces.

More conventional metasurfaces comprise geometrically simple nano-resonators such as simple cuboidal or elliptical posts, the effects of which are characterized by the real-valued phase difference accumulated along orthogonal axes, defined as the ordinary (ϕ_o) and extraordinary (ϕ_e) axes. Effectively, each nano-resonator acts as a waveplate of arbitrary phase shifts, controlled exclusively by its physical parameters —no material birefringence is necessary. Additionally, each nano-resonator, hosting its own multipolar resonance, may be coupled by near-field interactions to neighbouring resonators, allowing for further control of the scattering properties. This is visually illustrated in Fig. 1.4, where the output polarization ellipses of each individual nano-resonator are shown, demonstrating the customizability of any given metasurface. This flexibility in construction naturally provides unprecedented freedom for the modification of transmitted polarization, since the designs are not bound by the starkly limited variety of birefringent material that may be usefully fabricated, opening paths towards entirely novel types of phase control such as gradient phase control [12], metalenses [13], holograms [14] and so forth, which would have previously been entirely impossible with conventional birefringent media [15].

As my thesis focuses primarily on the manipulation of polarization using metasurfaces, it is useful to consider some of the similarities and differences between classical and quantum light. The quantization and addressing of light as photons naturally introduces the notion of quantum mechanics, but it is no surprise that the quantum nature of light, straddling the duality of particle and wave, shares much in common with classical light. Indeed, classical light fields can and have been used to

mimic the properties of *quantum* fields, allowing quantum experiments to be verified and tested using classical techniques, going so far as to result in classical expression of entanglement, a concept which seems utterly intertwined with quantum mechanics [16]. Furthermore, quantum two-level systems can be analogously expressed using polarization states of light, such as a spin 1/2 system. This extends further still to the concept of quantum computing using light; with polarization being comprising the equivalence of a two-level system, it is possible to define a qubit using two orthogonal polarizations. This depth of expression using polarization arises from its nature as a multiply parametric quantity, a concept is discussed further in Chapter 4. With multiple orthogonal bases freely available using the polarization degree of freedom, it constitutes a SU(2) rotation group, and as such, may map to any similar system, with the polarization states of light forming a full Hilbert space. We may choose, for example, the horizontal ($|H\rangle$) and vertical ($|V\rangle$) polarization states, with the three Pauli matrices

$$\sigma_1 = \begin{bmatrix} 0 & 1 \\ 1 & 0 \end{bmatrix}, \quad \sigma_2 = \begin{bmatrix} 0 & -i \\ i & 0 \end{bmatrix}, \quad \sigma_3 = \begin{bmatrix} 1 & 0 \\ 0 & -1 \end{bmatrix}$$

comprising the operators which generate the group. Of course, the choice of polarization basis states are arbitrary and may be freely chosen.

Beyond even the already vast utility of classical light as an analogy to quantum mechanical systems, quantum light is, of course, a hotly researched field. Even within quantum regimes, polarization remains a critical property that may be exploited, such as in general entanglement schemes, in which polarization is a commonly used degree of freedom, or in quantum cryptography, where the polarization of single photons is used to convey information. With the sheer flexibility of light-matter interactions, metasurfaces comprise a potent tool with which to manipulate said quantum light, and while a detailed accounting is beyond the scope of this thesis, some examples of applications of metasurfaces with quantum experiments are shown in Fig. 1.5.

We see, first of all, key schematics for the notion of photon entanglement manipulation with Fig. 1.5(a,d) in vastly different ways. In (a) is an illustration a standard experimental setup for Type-II Spontaneous Parametric Down Conversion (SPDC) production and selection of polarization entangled photon pairs, and in (d) is a conceptual sketch of the entanglement between the spin and optical angular momentum modes of a *single* photon. Entangled photons are a key aspect of many quantum-optical experiments and uses, and will be explored further in Chapter 3. In Fig. 1.5(b) is another demonstration of the breadth of capabilities metasurface platforms offer, in this case macroscopic quantum vacuum engineering utilizing the metasurface to break vacuum fluctuation symmetry. Yet another example is shown in Fig. 1.5(c), showing past works on singleshot polarimetry with metasurfaces. In Chapter 5, I will present my own approach to this problem, building on and improving existing techniques. Finally, in Fig. 1.5(e), we see a generic sketch of the concept of quantum qubits mediated by interference at a surface. With qubits

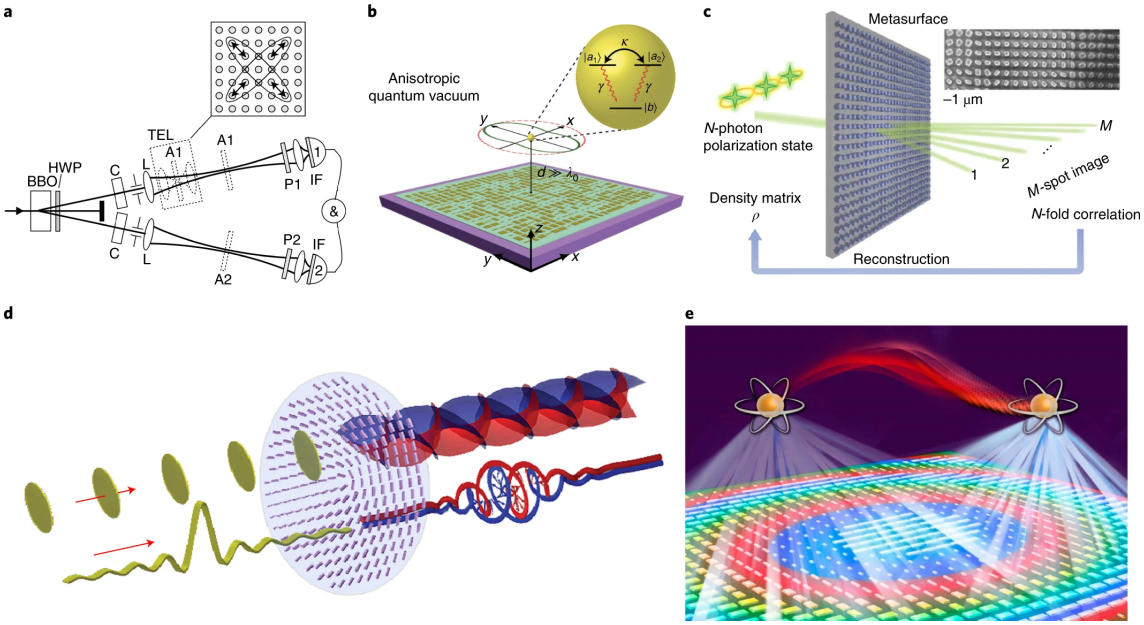

FIGURE 1.5: Figure adapted with permission from Ref [17], subfigures originally taken from Refs [18, 19, 20, 21, 22]. Examples of applications of metasurfaces with quantum light. (a) Photon entanglement transmitted through a plasmonic metasurface. (b) Metasurface-enabled long-distance quantum interference. (c) Quantum optical state reconstruction based on a metasurface. The top-right inset shows a scanning electron microscope image of the fabricated all-dielectric metasurface with a scale bar of $1\mu m$. (d) Quantum entanglement of photon orbital angular momentum and spin using metasurfaces. (e) Quantum entanglement between atomic qubits mediated by a metasurface.

as the quantum analogue of bits in conventional computing, quantum computing is a burgeoning field with much to explore, promising incredible improvements for certain classes of problems.

The exploration of quantum light is a field that has seen an enormous amount of interest in recent years, and despite that, there remains a wealth of capability and applications waiting to be realized. Many of these aspects will be discussed during the course of this thesis, with a focus towards more fundamental building blocks of more elaborate experiments and research. In many cases, there are strong conceptual crossovers and commonalities between classical and quantum light, and accordingly, I shall be drawing inspiration from these grey areas.

Regardless of the nature of light, whether quantum or classical, manipulation and measurement of polarization in light is an utterly fundamental aspect of life and physics, seeing a wealth of diversity in use ranging from astronomy [23], to seismology [24], biology [25, 26], materials science [27], quantum optics [28], and so forth. The list is near endless, and growing with every day that passes.

1.2 Design and fabrication of metasurfaces

Theoretical design notions aside, it is of course necessary to ground any such theory in practical, experimental work. As mentioned in the previous section, the key enabling factor that has seen metasurfaces explode into viability has been the relative availablility of precision, nanometer scale fabrication, and at the same time, this same availability is arguably one of the primary handicaps suffered by metasurfaces. This unavoidable reliance on precision manufacturing techniques presents its own problems, which will be discussed in this section.

The first problem is the scale on which metasurfaces exist. While the Maxwell equations describing electromagnetic waves, and by implication Mie theory, are scale-invariant, the fact that metasurfaces exist on a similar scale as the wavelength of light presents practical issues. Notably, near-field interactions of the resonances between the adjacent nanostructures comprising the metasurface can be non-negligible, resulting in second order effects. These effects are equally non-trivial to solve analytically, and require the application of numerical simulations to investigate. I will, throughout this thesis, describe and adapt existing techniques for the purposes of simple but highly flexible design processes, with a more in-depth examination in Chapter 4, especially as pertains to the potential for creating asymmetry from symmetric structures.

The second problem similarly relates to the scale of metasurfaces, and how this scale affects the potential design space. With metasurfaces depending on fabrication of structures on the scale of tens of nanometers, and thus, the precision which metasurfaces can be designed and used is bounded by those fabrication techniques. While industry silicon designs are indeed achieving nanometer-scale precision, such techniques are largely proprietary and unavailable for our use. It becomes prudent, therefore, to consider what *is* available for practical usage in metasurface fabrication.

Fabrication of metasurfaces involves, in general, some form of deposition of a resist layer onto a base material, followed by patterning of the resist layer, and finally, removal of the material not shielded by the patterned resist to achieve the designed structure. This may occur in a number of permutations depending on the desired metasurface, including multiple layers of patterning and etching, and with various different types of materials and substrates. Numerous methods of patterning and etching exist, each with benefits and drawbacks.

Industrial efforts are on the cusp of mass fabrication of metasurfaces, with considerable effort and increasing investments towards the commerical development thereof, seeing interest in both established industry and in startup companies [29, 30]. Following in the footsteps of these commerical efforts, we may consider the industrial fabrication of silicon and other semiconductors as the closest analogue. Such industrial fabrication efforts typically utilize photolithography, a process which in general involves the creation of an opaque, negative-pattern mask which is used to transfer the pattern to photoresist. This patterned photoresist acts

as a protective shield, allowing the material beneath it to be safely etched into that pattern. The specifics vary from process to process, with different functional devices possessing substantially different characteristics [31], some of which are shown in Fig. 1.6, however, all of these retain the same fundamental workflow of preparing an opaque mask which is used to pattern the photoresist. This is both the strength and the critical weakness of photolithography: the mask is non-trivial to prepare, and while it results in highly reproducible and consistent patterning, it substantially limits the flexibility of the lithography step. This is favoured in industrial fabrication processes, however, it is not suitable for our purposes.

By contrast, in small-scale, laboratory prototyping, the primary method utilized is Electron Beam Lithography (EBL)[32]. EBL utilizes a directed electron beam to draw patterns on the surface in question, allowing for arbitrary patterns up to the intrinsic resolution limits of 3 to $5nm$[33]. However, this resolution limit is naturally subject to equipment limitations, with similar equipment-specific caveats applying to the repeatability and maximum surface area of any given patterning. In return, with the potential for *arbitrary* patterning, EBL allows for rapid and unconstrained prototyping, allowing for fast development cycles in fabricating and testing new designs. These advantages make EBL the primary process used in developing metasurfaces, though it is likely that any commercial production will fall back to other techniques such as conventional photolithography. Nevertheless, the practicalities of fabrication techniques dictate limitations on the minimum structural features of any metasurface design. Accordingly, my work throughout this thesis necessarily incorporates such considerations, with care taken to ensure that the metasurfaces thus designed are fabricatable in practical terms. Some of the measures taken include suiting minimum feature size to the minimum resolution of the fabrication processes, and similarly, ensuring that there the minimum clearance between features is met.

Numerical modelling is heavily used in the field of metasurface research to predict and design properties of a given structure before fabrication. Correspondingly, a great deal of work has been dedicated towards efficient methods to solve this problem, producing a variety of computational tools with which to perform such tasks. Among them are general solvers for Maxwell's equations such as the Finite-Difference Time Domain (FDTD)[34], Finite Integration Technique (FIT)[35] and Finite Element Method (FEM)[36], as well as more constrained methods such as Rigorous Coupled-Wave Analysis (RCWA)[37], which is limited to the scattering of periodic, dielectric structures. These tools may be distinguished, in general, by their algorithmic approaches to the discretization in the spatial and temporal dimensions of the task as well as different solution goals, and some of these approaches are illustrated in Fig. 1.7. A more detailed accounting of these differences and approaches is beyond the scope of this thesis.

These modelling tools are typically employed as an optimization step during the design process, which is naturally *intermediate* step, one which is preceded by establishing optimization targets. Logically, one must first establish the

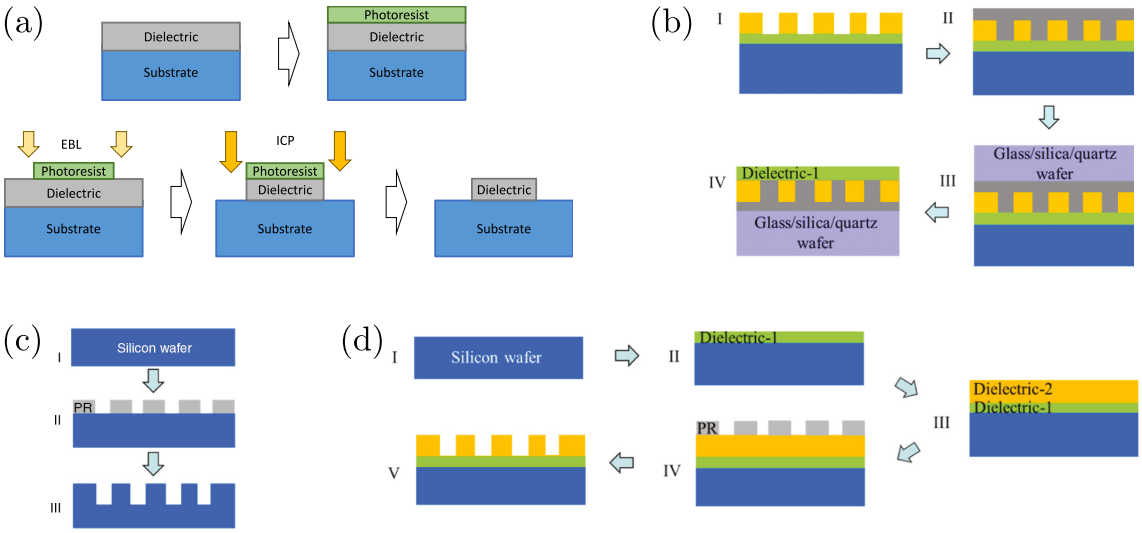

FIGURE 1.6: Schematic illustration of several metasurface fabrication techniques, demonstrating several different use-cases and final structures. (b, c, d) adapted from Ref [31]. (a) Electron beam lithography followed by Inductive Coupled Plasma etching for small-scale fabrication (b) Metasurface-based devices demonstrated on 12-inch glass wafer using immersion scanner and layer transfer process. (c) Metasurface-based devices demonstrated using immersion scanner and direct etching on 12-inch Si wafer. (d) Metasurface-based devices demonstrated using an immersion scanner on 12-inch Si wafer with a dielectric layer on top.

desired properties and general structure of the metasurface before performing the optimization step, which typically calls for an analytical design phase, during which a number of factors must be considered. An alternative design paradigm does exist in the form of inverse design optimization, wherein the desired performance is specified and large-scale numerical modelling is used to generate a suitable structure [39, 40]. Focusing instead on the conventional pathway that is utilized in this thesis, my methodology encompasses several concerns, theoretical and practical both, and addresses them in such a manner as to produce optimal designs which maximize transmission while maintaining the full capabilities of the target design via careful, analytical construction of the design parameters as well as a multistep optimization process.

A particular pitfall of numerical optimization designs in the context of metasurface design is that metasurfaces are highly multivariate, with an exceptionally large number of parameters specifying the metasurface properties. For something as simple as a metasurface comprising two types of cuboidal pixels, as are demonstrated in Chapter. 2, a multivariate optimization with a dimensionality of 6 must be performed. Approaches such as topological optimization, which will be discussed later, possess even large variable spaces, resulting in what is known as the curse of dimensionality [41]. The volume of the space to be optimized over increases

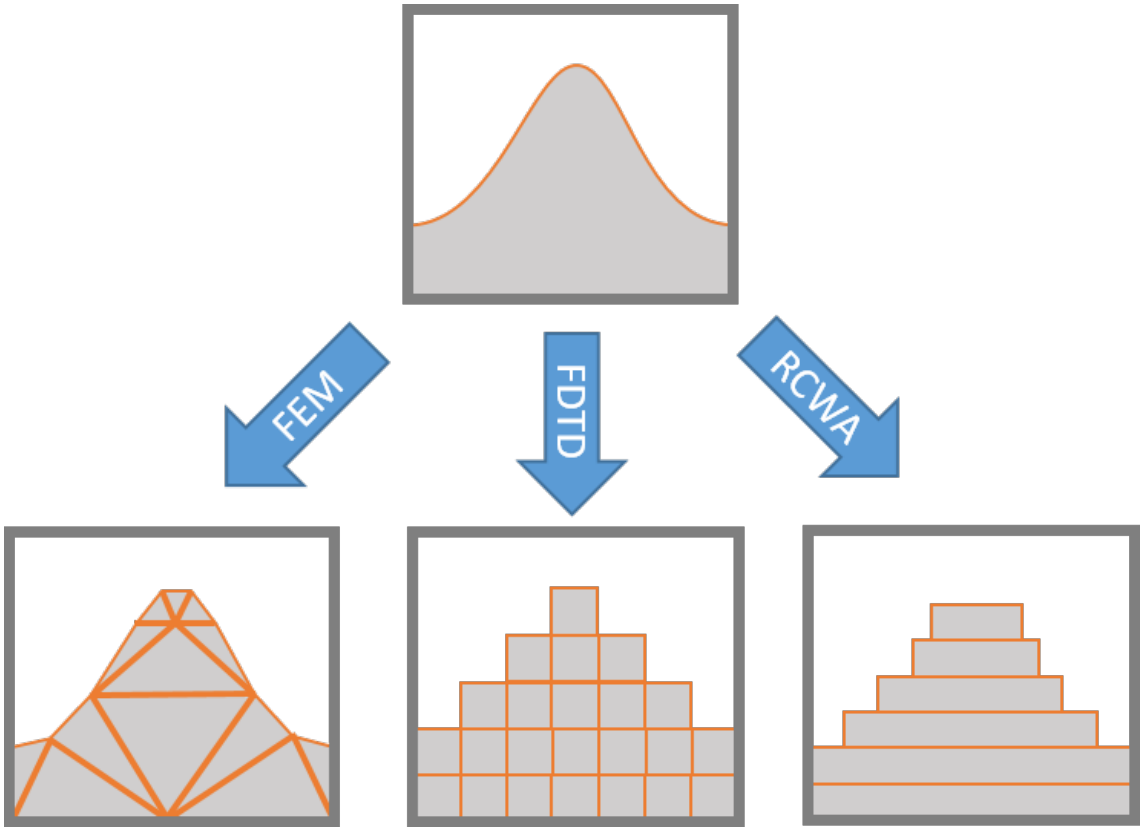

FIGURE 1.7: Figure adapted from *JCMwave* [38]. Visual representation of approaches taken by several electrodynamic solvers. (a) Finite Element Method, decomposing a geometry into an unstructured or irregular grid. (b) Finite-Difference Time Domain, decomposing the geometry into a regular grid. (c) Rigorous Coupled-Wave Analysis, which decomposes the geometry into layers.

proportional to the exponent of the number of variables, resulting in exponentially increasing demands on computational resources. This is problematic even with relatively limited dimensional spaces as encountered in this thesis, with singular numerical simulations taking timespans on the scale of minutes. Furthermore, simple optimization algorithms such as gradient descent can be problematic in such multivariate environments, where local minima are common, resulting in failures to locate global optimum solutions.

As such, a more judicious design process becomes necessary. An analytical design may be used to constrain the design space of the metasurface, and with a relatively coarse search, the optimization space constrained yet further. This approach therefore hinges on the theoretical design approach, which is, in turn, informed by the practical capabilities of fabrication available. As discussed earlier, expecting a perfect replication of designed structures in a given fabrication is not reasonable, absent highly specialized fabrication runs which are not necessarily available for a prototyping stage. There are two ways by which this was addressed

throughout the course of my thesis: error-tolerant designs and adaptable design goals.

In this thesis, error-tolerance refers to the robustness of a metasurface against fabrication and experimental error. In general, knowing the ideal parameters to achieve a given goal with a metasurface, it is possible to quantify how that metasurface will respond to perturbations from that set of designed parameters. With that quantification, it is thus possible to treat this error-tolerance as a property which may both be defined in terms of other quantities, as well as a goal that can be optimized towards in both theoretical and numerical design phases. By designing metasurfaces with this robustness in mind, it is thus possible to mitigate the flaws in physical fabrication processes. This will be addressed in more detail in Chapter 5.

Adaptable design goals are another way in which fabrication concerns may be mitigated. Fabrication flaws result in largely unpredictable deviations of any given metasurface's optical properties from the theoretical design, however, if the deviation is not overtly catastrophic, it remains eminently reasonable to expect that the fabrication can still approximate the original design intent. If the intention is merely to demonstrate some principle of action as opposed to a *specific* scenario, then it is sufficient to consider cases that are close to the original design, and a perfect replication may be sought after as a later, secondary goal when some specific performance is desired. My thesis employs this principle to demonstrate the fundamental concepts without constraining the design space too far.

In more general terms, metasurface design may be approached in several ways. The first is as a strict replacement to one or more bulk-optical components; most trivially, a uniform metasurface may act as a compact, exact replacement for a waveplate [9], or indeed, a basic metalens may be used as a replacement for a lens [15]. In and of itself, such advances already offer benefits in the form of a great reduction in general size and weight, which is useful for applications such as miniaturization and physical robustness of sensing setups, however, this barely scratches the surface. With the versatility of metasurfaces and the complex optical transformations that can be attained, they can also act as replacements for *multiple* bulk optical elements, compressing an entire optical circuit segment into a single element.

Considering a metasurface to be a strict replacement invites a particular design methodology: one may naively tackle its design by considering the metasurface in strict terms of the optical components it is replacing. For example, working in the polarization regime, one may consider the mathematical Jones matrices of the elements to be replaced, combine them, and simply design a metasurface that replicates the resultant transfer matrix. While this is an intuitive design process, however, it does not necessarily produce an optimal result. Instead, the metasurface should be designed in terms of its analytical operation, which is especially attractive when working in the polarization regime, as I will explore throughout the rest of this thesis. In general, the desired analytical operation of a set of bulk optics may be defined *without* reference to the physical structures, and

this purely mathematical approach allows for the design of a metasurface towards a more optimal solution, a general concept which I will explore in Chapters 2 and 4, especially as pertains to the idea of complex birefringence.

Even so, the versatility of metasurfaces does not end with acting as replacements for bulk optics. Metasurfaces are equally capable of fundamentally new types of operations, with new technologies and capabilities developing out of computer-driven approaches, such as topological optimization and machine-learning driven techniques. These new operations bring concepts such as information optics, quantum metasurfaces and holography into the realms of possibility, where before these were confined to strict theory. Quantum theory is particularly relevant. Not only do metasurfaces enable the direct implementation of quantum theory and optics by allowing for flexible and accessible photonic manipulation, quantum theory also sees many analogues in classical light, and metasurfaces allow for these quantum-classical experiments to be implemented with relative ease. Some of these will be discussed in my thesis, for example, the manipulation of quantum polarized light with metasurfaces, as well as utilizing Positive-Operator Valued Measurements (POVM) with polarimetry in Chapter 5.

1.3 Scope of thesis

This thesis focuses on the manipulation and measurement of polarized light utilizing metasurfaces. The key concepts developed over the course of my thesis revolve primarily around the concept of multi-part dielectric metasurfaces, working exclusively in the transmission regime with a focus on maximizing the respective transmissivities. In this context, I focus my work primarily around deepening our capabilties in controlling and modifying a key aspect of light, polarization, through the concept of complex birefringence.

In Chapter 2, I will be discussing my work on complex birefringence. Based on recent works [42], complex birefringence extends the concept of conventional birefringence by introducing the notion of gain and loss to a birefringent transformation. Here, I demonstrate that unlike original proposals, gain is unnecessary, and completely arbitrary polarization manipulation may be accomplished using only judiciously engineered losses via diffraction. I also cover in this chapter the primary design and fabrication techniques which I employ throughout the course of my thesis. These techniques were used to verify the practicality of complex birefringence both in numerical modelling as well as classical experimental implementation.

Chapter 3 extends the notion of complex birefringence yet further into the quantum regime, utilizing experimental results and theoretical extension to discuss the applicability of such metasurfaces into quantum experiments. This chapter addresses, in general, biphoton states, which are both ubiquitous in many aspects of quantum optics as well as being ideally suited as the primary target of manipulation

with complex birefringence.

Next, in Chapter 4, I develop a concept for the sensitive monitoring of small polarization deviations from an arbitrarily chosen state, revealing that the approach chosen is analytically optimal within the constraint of chirality. This analysis is further extended into the chiral regime, discovering that there exist a class of polarization states which are best addressed using a chiral metasurface, and subsequently designing an appropriate metasurface using numerical modelling before finally demonstrate sensitive monitoring with experimental verification.

In Chapter 5, I explore singleshot polarimetry using a metasurface. My work continues previous developments on the topic, applying a Positive Operator Value Measurement approach from quantum mechanics to accomplish singleshot polarimetry with imperfect measurement bases, revealing that a pathway towards significantly eased precision constraints is both possible and practical. This is demonstrated with both numerical as well as experimental verification, proving to be both robust and efficient.

Finally, in Chapter 6, I summarize the works I have performed over the course, drawing conclusions from the experimental and numerical results as well as providing outlooks on potential future explorations of the concepts I have laid out.

Chapter 2

Complex birefringence

Complex birefringence is a recently suggested concept that extends the concept of conventional, real-valued birefringence [42]. As discussed in Chapter 1, phase control is a critical aspect of optics, and is a part of nearly every optical experiment. Much of this control is afforded by conventional birefringence in various forms, from waveplates, to general phase retarders, to many nonlinear optical components [43]. By introducing non-Hermiticity, whether gain or loss, to a birefringent transformation, it is possible to enable fundamentally new types of polarization control, expanding the degrees of freedom in which polarization might be manipulated.

In this chapter, I show that complex birefringence is a powerful tool with which polarization may be readily transformed in various manners, as well as describing and demonstrating in experiment a practical, analytically optimal design and fabrication process through which this complex birefringence may be accomplished in physical terms, allowing for flexible and compact access to regimes of polarization manipulation that were not previously available.

Conventional birefringence is a Hermitian transformation. Birefringence is the property of a material wherein different refractive indices are present along the ordinary and extraordinary optical axes of the material, in turn imposing different phase retardances to incident light, and inducing phase shifts in the polarization of the light. Barring practical losses such as reflection, material absorption, imperfections and so forth, conventional birefringence is lossless. Naturally, this imposes restrictions on the possible transformations that may be performed, which are typically alleviated by utilizing a combination of bulk optical elements to accomplish. However, *complex* birefringence presents an additional degree of freedom in a singular element, delivering benefits in applications such as polarization measurements and entanglement experiments, especially in scenarios like satellite and long-term experiments where compactness and robustness is critical.

The most important restriction of conventional birefringence arises from its strength, that of a conservative transformation. Here, 'conservative' and 'Hermitian' are used somewhat interchangeably, referring respectively to the physical and the mathematical implications of the same concept. A conservative transformation of light is one that does not alter the amount of energy present within that light, and mathematically, that transformation may be described by

a Hermitian transfer matrix. As such, this limits the types of transformations that can be implemented using simple birefringence. Non-conservative operations on light, such as the general case of polarization transformation, are currently implemented using an optical circuit of bulk optical components. At minimum a waveplate, partial linear polarizer, and another waveplate, implementing tunable polarization-dependent loss, to create such a transformation. This is less than ideal, introducing additional sources of inaccuracy to any experiment in both the imperfection of individual optical elements, as well as that of mechanical error in building the setup. Furthermore, for cases such as optical communications networks and sensing, compactness is often prized, contraindicating the utility of such a setup.

Complex birefringence is termed as such due to the introduction of gain and-or loss to the concept of birefringence [42], resulting in complex refractive indices (and the related permitivitty tensors). However, gain is as yet a highly nontrivial property to engineer, and as such, it is not a realistic concept to utilize. In the hypothetical case that gain may be reasonably introduced within the desired form-factor, however, there remains an additional obstacle in that gain media amplify *all* incident light, including noise, which is especially undesirable in the case of quantum experiments, working as they do with low photon count problems. As such, it becomes clear that working exclusively with losses to implement complex birefringence is a superior option, with the additional caveat that minimizing those losses would of course be ideal.

It is precisely these aspects which I will focus on in this chapter, leveraging judiciously engineered losses to enable true flexibility of manipulation of polarization in a compact, monolithic structure, enabling full compacting of bulky and expensive optical setups into a single unit. I will develop a theoretical analysis, showing that the chosen approach is optimal, and subsequently demonstrate this approach in experiment.

2.1 Complex birefringence from Singular Value Decomposition

Consider a pair of states $|A_i\rangle$ and $|B_i\rangle$. Representing a transformation $\mathbf{T}$ in Jones formalism, it is clear that under a conventional, unitary transformation, defining a desired transformation $\mathbf{T}|A_i\rangle = |A_f\rangle$ naturally fixes the corresponding transformation, since

$$\langle B_f|A_f\rangle = \langle B_i|\mathbf{T}^\dagger\mathbf{T}|A_i\rangle \tag{2.1}$$
$$\langle B_f|A_f\rangle = \langle B_i|A_i\rangle, \tag{2.2}$$

given that $\mathbf{T}$ is unitary by definition. Thus, while it is possible to define an arbitrary polarization state to another, it is not possible to define arbitrary transformations for pairs of states using conventional birefringence [44].

However, it has been demonstrated theoretically [42] that to achieve truly arbitrary control over pairs of polarisation states, it is a sufficient condition to achieve for some transformation $\mathbf{T}_{\text{compl}}$:

$$\begin{aligned} |s_1\rangle &= \mathbf{T}_{\text{compl}}|\theta\rangle \\ |s_2\rangle &= \mathbf{T}_{\text{compl}}|-\theta\rangle, \end{aligned} \tag{2.3}$$

where $|s_1\rangle$ and $|s_2\rangle$ are opposing pairs of polarisation states, such as diagonal and anti-diagonal states, and $|\pm\theta\rangle$ are polarisation states coplanar with and symmetrically separated by an angle θ about a state of equal distance to $|s_1\rangle$ and $|s_2\rangle$. This transformation is necessarily non-conservative and non-hermitian, in contrast to conventional birefringent materials. The action of such a transformation may be seen in Fig. 2.1.

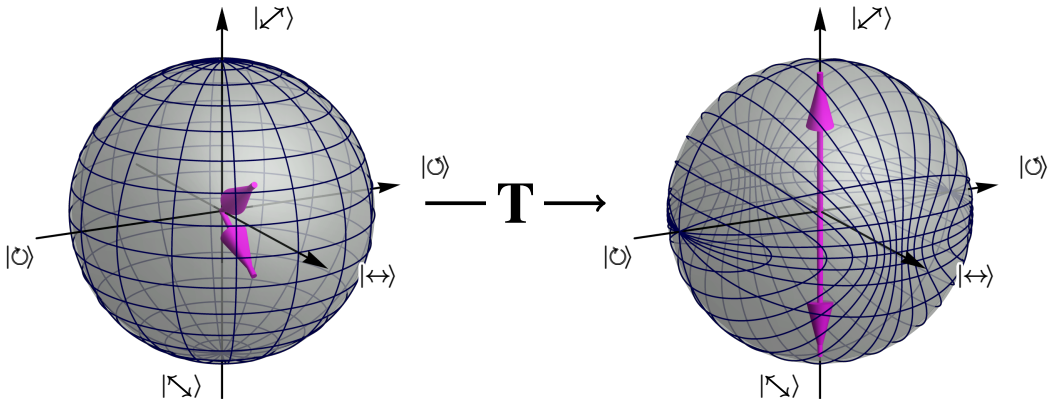

FIGURE 2.1: Transformation of polarization states with a complex-birefringent wave plate, visualized on a Poincaré sphere. Left: two input states with close polarization state vectors indicated by purple arrows. Right: state vectors (purple arrows) after a transmission via a complex-birefringent wave plate, which become orthogonal. The distorted gridlines additionally illustrate nontrivial polarization changes for various input states. They are transformed by a non-conservative transformation into the form as seen on the right.

Here, it is relevant to consider the Jones calculus representation of polarization. Jones calculus is a mathematical treatment for fully polarized light, wherein a single fully polarization state $|\psi\rangle$ may be represented generally with

$$|\psi\rangle = \begin{bmatrix} E_x \\ E_y \end{bmatrix},$$

where E_x and E_y are complex values denoting the components of the electric field aligned along some arbitrarily chosen, orthogonal axes perpendicular to the direction of propagation of light. This is known as the Jones vector of a polarization state.

It is important to emphasize that unlike Mueller calculus, which will be discussed later, the Jones vector can only represent *fully* polarized light. A global phase factor is frequently eliminated from this polarization representation for the sake of convenience. Equivalently, we may express common types of polarization states under the Jones formalism, for example, horizontal and vertical states denoted respectively as:

$$|H\rangle = \begin{bmatrix} 1 \\ 0 \end{bmatrix}, \quad |V\rangle = \begin{bmatrix} 0 \\ 1 \end{bmatrix}.$$

This formalism invites similar forms to denote the transformation implemented by any given optical element. In this case, the transformations are denoted by 2×2 matrices also known as the Jones matrix or transfer matrix of a given optical element. Notably, if losses through practical concerns such as material absorption or stray reflections are ignored, any conventional optical element such as polarizers and waveplates are represented in the Jones formalism as Hermitian matrices. That is to say, it is true of any conventional Jones matrix that

$$J = J^{\dagger},$$

where $J^{\dagger}$ denotes the conjugate transpose of the matrix J.

The task then becomes to formulate a non-Hermitian transfer matrix that is capable of fulfilling the requirements for arbitrary control which does *not* rely on gain. The starting point is the the Singular-Value Decomposition (SVD), which decomposes a 2×2 matrix as follows,

$$\mathbf{T}_{\text{compl}} = \mathbf{U} \begin{bmatrix} \sigma_1 & 0 \\ 0 & \sigma_2 \end{bmatrix} \mathbf{W}^{\dagger} \tag{2.4}$$

$$= \mathbf{U} \cdot \mathbf{M} \cdot \mathbf{W}^{\dagger}, \tag{2.5}$$

where $\mathbf{U}$ and $\mathbf{W}$ are complex, unitary matrices and σ_1 and σ_2 are non-negative and real. The SVD of a matrix is a generalization of an eigenvalue decomposition,and indeed, the column vectors comprising the matrices $\mathbf{U}$ and $\mathbf{W}$ constitute orthonormal vectors which can be used as basis vectors, related by the corresponding mapping of $\sigma_i \mathbf{M}$. While general, complex SVD computation is a non-trivial task, this thesis only requires consideration of the decomposition of a 2×2 matrix $\mathbf{T}$, which possesses known analytic solutions [45].

We contextualize this decomposition physically as $\mathbf{T}_{\text{compl}}$, a Jones transfer matrix, which is a complex, 2×2 matrix that represents the transformation of a polarization element on an incident polarization state. Notably, the ratio σ_2/σ_1 defines the degree of polarization-dependent transmission, and accordingly, the degree of complex birefringence offerred by the transfer matrix in question. As such, we may

further decompose the equation as follows:

$$\mathbf{T}_{\text{compl}} = \frac{\sigma_1}{2}\mathbf{U}\begin{bmatrix}1 & 0\\ 0 & e^{i\kappa}\end{bmatrix}\mathbf{W}^\dagger + \frac{\sigma_1}{2}\mathbf{U}\begin{bmatrix}1 & 0\\ 0 & e^{-i\kappa}\end{bmatrix}\mathbf{W}^\dagger = \frac{\sigma_1}{2}(\mathbf{T}_1 + \mathbf{T}_2), \tag{2.6}$$

where $\kappa = \cos^{-1}(\sigma_2/\sigma_1)$. This solution is non-unique. Since $\mathbf{U}$ and $\mathbf{W}$ are both unitary, it follows that $\mathbf{T}_1$ and $\mathbf{T}_2$ are, by construction, unitary matrices. This thus demonstrates that by any arbitrary complex transformation may be performed by the linear sum of two unitary transformations while considering only losses. Each unitary transformation may be performed by a single metasurface pixel, and as such, it follows that an arbitrary, complex transformation may be physically implemented using the combination of just two types of metasurface pixels.

It may be observed from Eq. 2.5 that this reveals an analytically optimal solution. Asserting for ease of notation that $\sigma_1 > \sigma_2$ and that $\mathbf{W}$, $\mathbf{U}$ respectively comprise the pairs of column vectors W_1, W_2 and U_1, U_2 such that $\mathbf{W} = [W_1, W_2]$, $\mathbf{U} = [U_1, U_2]$, we observe that an input polarization state W_1 is transformed to $\sigma_1 U_1$ at the output. In absence of gain, this state is fully transmitted when $\sigma_1 = 1$. This thus presents the fact that there exists a necessarily maximum transmission for a single polarization state, which may be arbitrarily chosen. Correspondingly, the orthogonal input polarization state W_2 is attenuated and transformed to $\sigma_2 U_2$. As such, the transformation $\mathbf{T}_{cmpl}$ may be interpreted physically as the combination of a waveplate and selective polarization attenuation, or general elliptical dichroism combined with the tailored and specific phase retardance of polarization eigenstates [46, 47, 48].

Absent any other constraints, this thus reveals that for any given transfer matrix $\mathbf{T}_{\text{compl}}$ there exists at least one solution by which we may decompose and express it optimally as the sum of conservative transformations, demonstrating a way to implement the transformation in a practical manner. The non-conservative nature arises from the tailored loss, which, barring inevitable losses from experimental concerns, is the minimum required to accomplish the the task.

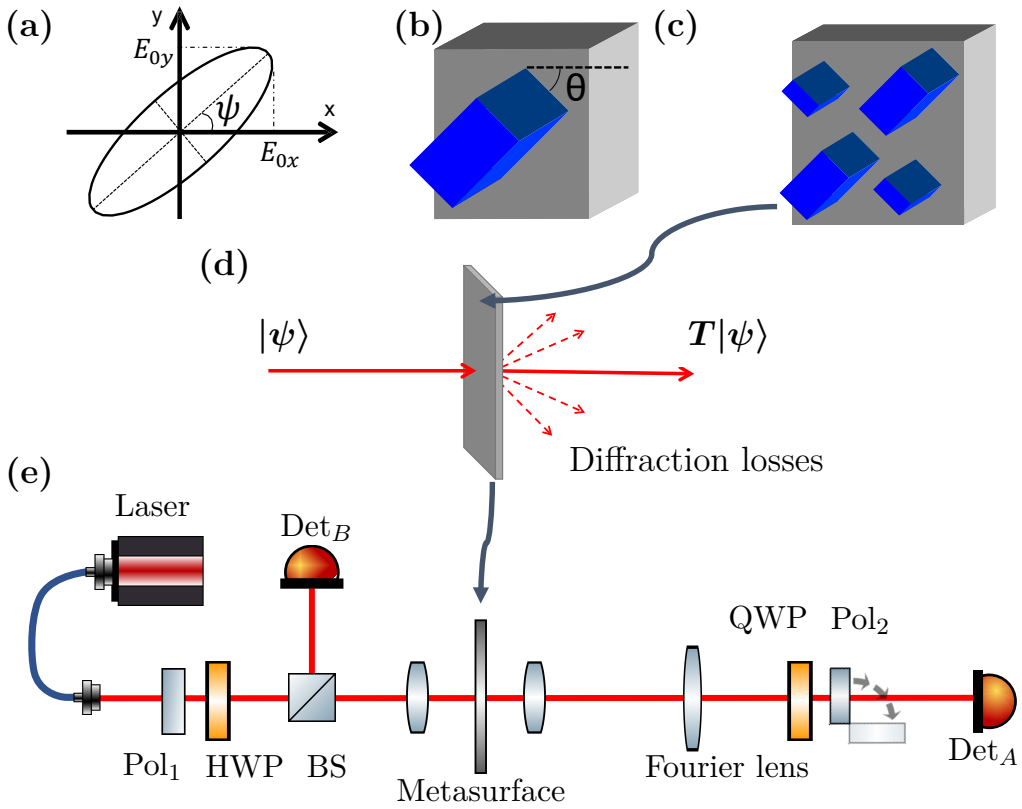

FIGURE 2.2: Concept of realizing complex birefringence with all-dielectric metasurfaces. (a) Conventional polarization control comprising real-valued phases along the ordinary and extraordinary axes, corresponding to a Jones vector $(E_{0x}, E_{0y}e^{i\phi})$[49] as might result from a (b) a homogenous array of nano-pillar dielectric resonators rotated at an angle θ. (b) A unit cell with two pairs of distinctly sized nano-pillars realizing complex birefringence, combining two singular pillars of different sizes and angles. (c) A metasurface utilizing the unit cell in (b), realizing engineered polarization-dependent losses via diffraction. (d) Schematic diagram of the experimental setup utilized to characterize the manufactured samples.

2.2 Tailored loss for polarization pair transformation

Having established that a transfer matrix transforming two arbitrarily chosen input polarization states $\{A_i,\ B_i\}$ into two other two arbitrarily chosen output states $\{A_t,\ B_t\}$ is an inherently non-conservative and therefore lossy transformation, we established that in the form of Eq. 2.6 we present an analytically optimal solution by construction. It then becomes prudent to consider the exact degree of loss that is incurred for any given transformation.

Consider, using the Jones formalism, two arbitrary input states

$$A_i = \begin{bmatrix} \cos\alpha_i \\ \sin\alpha_i e^{i\varphi_i} \end{bmatrix}, \quad B_i = \begin{bmatrix} \cos\beta_i \\ \sin\beta_i e^{i\phi_i} \end{bmatrix},$$

and the desired output states

$$A_t = \begin{bmatrix} \cos\alpha_t \\ \sin\alpha_t e^{i\varphi_t} \end{bmatrix}, \quad B_t = \begin{bmatrix} \cos\beta_t \\ \sin\beta_t e^{i\phi_t} \end{bmatrix},$$

where α and β, φ ad ϕ define the polarization angle and phases of the respective states. The corresponding orthogonal input states are then

$$A_i^{\perp} = i\varsigma_2 A_i^* = \begin{bmatrix} -\sin\alpha e^{-i\varphi_i} \\ \cos\alpha \end{bmatrix}, \quad B_i^{\perp} = i\varsigma_2 B_i^* = \begin{bmatrix} -\sin\beta e^{-i\phi_i} \\ \cos\beta \end{bmatrix},$$

where

$$\varsigma_2 = \begin{bmatrix} 0 & -i \\ i & 0 \end{bmatrix}$$

is the second Pauli matrix. We may then write Eq. 2.6 explicitly as:

$$\mathbf{T}_0 = \langle A_t^* | B_i \rangle \cdot |B_t\rangle\langle A_i^{\perp}| - \langle B_t^* | A_i \rangle \cdot |A_t\rangle\langle B_i^{\perp}| = \begin{bmatrix} \tau_{11} & \tau_{12} \\ \tau_{21} & \tau_{22} \end{bmatrix}, \tag{2.7}$$

where

$$\begin{aligned} \tau_{11} =& \sin\alpha_i \cos\beta_i \cos\alpha_t \cos\beta_t\ e^{i\varphi_i} + \sin\alpha_i \sin\beta_i \sin\alpha_t \cos\beta_t\ e^{i(\varphi_i+\phi_i+\varphi_t)} \\ & - \cos\alpha_i \sin\beta_i \cos\alpha_t \cos\beta_t\ e^{i\phi_i} - \sin\alpha_i \sin\beta_i \cos\alpha_t \sin\beta_t\ e^{i(\varphi_i+\phi_i+\phi_t)}, \end{aligned} \tag{2.8}$$

$$\tau_{12} = \tau_{21} = \sin\alpha_i \cos\beta_i\ \cos\alpha_t \sin\beta_t\ e^{i(\varphi_i+\phi_t)} - \cos\alpha_i \sin\beta_i \sin\alpha_t\ \cos\beta_t\ e^{i(\varphi_t+\phi_i)}, \tag{2.9}$$

$$\begin{aligned} \tau_{22} =& \cos\alpha_i \cos\beta_i \sin\alpha_t \cos\beta_t\ e^{i\varphi_t} + \sin\alpha_i \cos\beta_i \sin\alpha_t \sin\beta_t\ e^{i(\varphi_i+\varphi_t+\phi_t)} \\ & - \cos\alpha_i \cos\beta_i \cos\alpha_t \sin\beta_t\ e^{i\phi_t} - \cos\alpha_i \sin\beta_i \sin\alpha_t \sin\beta_t\ e^{i(\phi_i+\varphi_t+\phi_t)}. \end{aligned} \tag{2.10}$$

The two singular values of $\mathbf{T}_0$ are given by

$$\sigma_{\min/\max} = \frac{1}{\sqrt{2}}\sqrt{|\tau_{11}|^2 + 2|\tau_{12}|^2 + |\tau_{22}|^2 \pm \gamma}\,, \tag{2.11}$$

where

$$\gamma = \sqrt{\left(|\tau_{11}|^2 - |\tau_{22}|^2\right)^2 + 4|\tau_{12}|^2\left(|\tau_{11}|^2 + |\tau_{22}|^2\right) + 8\,\mathrm{Re}\left(\tau_{11}^*\tau_{12}^2\tau_{22}^*\right)}\,. \tag{2.12}$$

And finally, we arrive at

$$\mathbf{T}_{complex} = \frac{e^{i\phi_g}}{\sigma_{\max}}\begin{bmatrix}\tau_{11} & \tau_{12}\\ \tau_{21} & \tau_{22}\end{bmatrix} = \begin{bmatrix}T_{11} & T_{12}\\ T_{21} & T_{22}\end{bmatrix}, \tag{2.13}$$

where ϕ_g is an arbitrary global phase. For an input state A_i, the output is a pure state, $\mathbf{T}\,|A_i\rangle = t_A|A_t\rangle$, with a transmission coefficient

$$\begin{aligned} t_A &= -\frac{e^{i\phi_g}\langle B_t^*|A_i\rangle\langle B_i^\perp|A_i\rangle}{\sigma_{\max}} \\ &= -\frac{e^{i\phi_g}\left(\cos\alpha_i\,\cos\beta_t\; + \sin\alpha_i\,\sin\beta_t\; e^{i(\varphi_i+\delta_t)}\right)\left(\sin\alpha_i\,\cos\beta_i\; e^{i\varphi_i} - \cos\alpha_i\,\sin\beta_i\; e^{i\delta_i}\right)}{\sigma_{\max}}. \end{aligned} \tag{2.14}$$

When the input state is B_i, the output pure state is $\mathbf{T}|B_i\rangle = t_B|B_t\rangle$, where the transmission coefficient is

$$\begin{aligned} t_B &= \frac{e^{i\phi_g}\langle A_t^*|B_i\rangle\langle A_i^\perp|B_i\rangle}{\sigma_{\max}} \\ &= \frac{e^{i\phi_g}\left(\cos\beta_i\,\cos\alpha_t\; + \sin\beta_i\,\sin\alpha_t\; e^{i(\delta_i+\varphi_t)}\right)\left(\sin\alpha_i\,\cos\beta_i\; e^{i\varphi_i} - \cos\alpha_i\,\sin\beta_i\; e^{i\delta_i}\right)}{\sigma_{\max}}. \end{aligned} \tag{2.15}$$

Therefore, the power transmission efficiencies $T_A = |t_A|^2$ and $T_B = |t_B|^2$ depend on the inner products of the states, which relate to the distances between the states on the Poincaré sphere. A few notable singularities become apparent from this analysis. Both T_A and T_B are zero when $A_i = B_i$ and $A_t \neq B_t$ because it is impossible to transform one state into two different states simultaneously. When A_i is orthogonal to the conjugate state of B_t, T_A will be zero. When B_i is orthogonal to the conjugate state of A_t, T_B will be zero. These features are evident in Fig. 2.3 showing the calculated transmission efficiency when four states are all linearly polarized, i.e. $\varphi_i = \delta_i = \varphi_t = \delta_t = 0$. One can see that $T_A = 0$ when $|\beta_t - \alpha_i| = \pi/2$ and $T_B = 0$ when $|\alpha_t - \beta_i| = \pi/2$. However, there are always some cases that T_A and T_B can reach 100% simultaneously.

In general, once the two polarization pairs are chosen, the transmission efficiencies may be analytically determined from these calculations. The solution shown here in Eq. 2.7 is the analytical maximum efficiency given the constraints of symmetricality and exclusion of amplification, since it has by construction a maximum singular value of one. However, this formulation also explicitly asserts that the off-diagonals τ_{12} and τ_{21} are equal, resulting in a symmetric transfer matrix $\mathbf{T}_{cmplx}$. This is *not* a fundamental restriction of the concept as expressed in Eq. 2.6, and this constraint is only necessary to guarantee that the decomposed transfer matrices $\mathbf{T}_1$ and $\mathbf{T}_2$ are symmetrical, the utility of which will be explained in the following

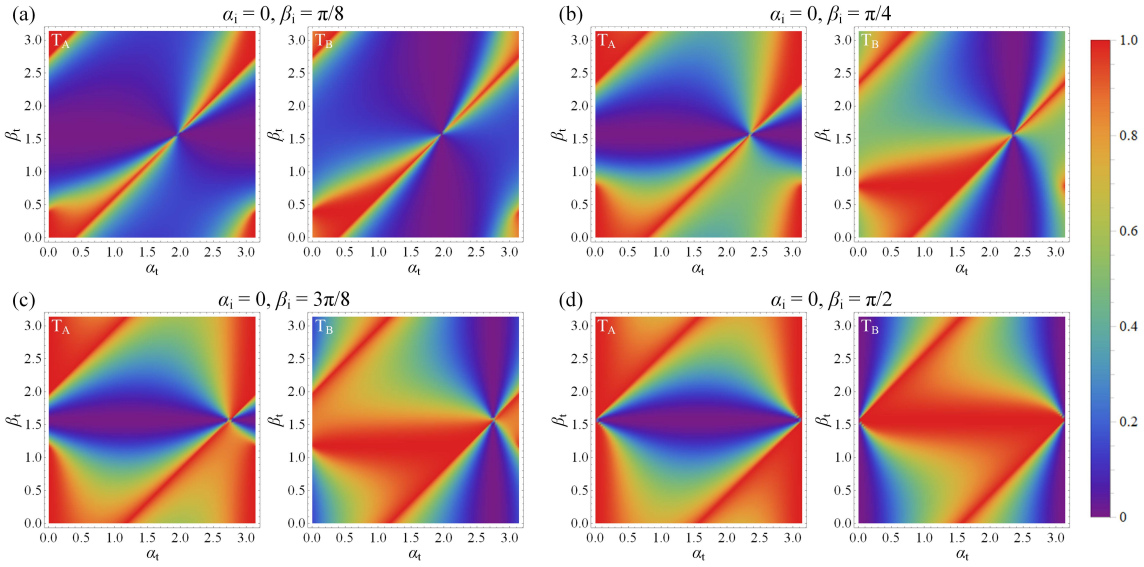

FIGURE 2.3: Transmission efficiency of the designed transfer matrix for transforming two linear polarization states into other two polarization states as functions of α_t and β_t when (a) $\alpha_i = 0$, $\beta_i = \pi/8$; (b) $\alpha_i = 0$, $\beta_i = \pi/4$; (c) $\alpha_i = 0$, $\beta_i = 3\pi/8$; and (d) $\alpha_i = 0$, $\beta_i = \pi/2$.

section. The notion of chirality in complex birefringence will be explored briefly in Section 4.

2.3 Dielectric metasurface design and fabrication

Dielectric metasurfaces are highly transparent and can easily attain transmission efficiencies greater than 85%[9]. As such, they are the ideal platform to complement the minimal loss associated with the theoretical design. Here, the additional constraint of symmetrical transfer matrices becomes clear: a symmetrical transfer matrix corresponds to a metasurface pixel of D_2 symmetry, such as a rectanglular cuboid or elliptical cylinder. This is beneficial in multiple ways; not only do dielectric metasurfaces exhibit weaker chirality as compared to the alternative of plasmonic metasurfaces [50], practical concerns arising from numerical design and fabrication meant that the simplification to a more constrained design space was desirable.

For a desired pair of polarization state transformations $\{A_{in}, B_{in}\} \rightarrow \{A_{out}, B_{out}\}$, we may use the derived solution for the transformation $\mathbf{T}_{cmpl}$ as shown in Eq. 2.13, expressing it with minor variations as:

$$\mathbf{T} = \frac{e^{i\phi_g}}{\sigma_1}\mathbf{T}_{cmpl} = \frac{e^{i\phi_g}}{\sigma_m}\left[\langle A^*_{out}|B_{in}\rangle \cdot |B_{out}\rangle\langle A^{\perp}_{in}| - \langle B^*_{out}|A_{in}\rangle \cdot |A_{out}\rangle\langle B^{\perp}_{in}|\right], \quad (2.16)$$

where σ_1 is the larger SVD value of $\mathbf{T}_{cmpl}$ and ϕ_g is a global phase. This global phase may be chosen arbitrarily, reflecting the invariance of this solution to the construction, and σ_1 is explicitly included as a scaling factor. The resultant transfer matrices are, again, symmetric by construction, and it may be demonstrated that $\langle H|\mathbf{T}|V\rangle \equiv \langle V|\mathbf{T}|H\rangle$ for all values of $\mathbf{T}$.

Following the choice of state transformations, Equation 2.6 can be used to decompose the transfer matrix into symmetrical, unitary components, which can be easily expressed as simple metasurface pixels. It is known that a pixel with simple, two-fold reflectional symmetry such as a cuboidal or ellipsoidal pixel produces a symmetrical transfer matrix of the form

$$\mathbf{T}_{single} = \mathbb{R}(-\theta) \cdot \begin{bmatrix} e^{i\phi_o} & 0 \\ 0 & e^{i\phi_e} \end{bmatrix} \cdot \mathbb{R}(\theta), \tag{2.17}$$

where $\mathbb{R}(\theta)$ is a rotation matrix of angle θ, and ϕ_o and ϕ_e are the ordinary and extraordinary phase retardances of the pixel [9, 51]. Interleaving these metasurface pixels as seen in Fig. 2.2(b,c) is equivalent to the linear sum of their transfer matrices, effectively implementing the right-hand side of Eq. 2.6, thus offering a straightforward path to implementing the initial complex transfer matrix. We refer to this pairwise arrangement of metasurface pixels as binary structures. The concept is not new, having seen usecases such as circular microwave polarizers [47], terahertz polarization gratings [52], optical holograms [53, 14], generators of vector vortex beams [54], however, the implementation of complex birefringence with such structures was, as of the commencement of my work on the concept, entirely unexplored.

Physically, this pairwise sum arises from the interference of coherent, incident polarization states transmitted through the nanopillars comprising the metasurface in the forward direction. The resultant diffraction corresponds to the polarization-dependent loss, thus constituting the non-Hermitian nature of the complex birefringence without any gain necessary.

Accordingly, numerical simulations to design the metasurfaces were then performed. Using Rigorous Coupled Wave Analysis [55, 56], sweeps across the physical sizes of individual, cuboidal resonators without rotation were generated, see Fig. 2.4. These sweeps were generated using idealized refractive indices of amorphous silicon on glass. In general, the superpixel periodicities used in this thesis are either of $1600nm$ or $1800nm$, with individual cuboidal pixels centered within a quadrant of the period. A global search was then performed over the space of this sweep, accounting for a degree of freedom in design of the nanoresonator rotation. The selected physical parameters were then simulated as a full binary metasurface and simulated numerically using a commercial electrodynamic solver, CST Studio. A notable limitation of Eq. 2.6 is that it does not consider potential second- and higher- order effects such as near-field interactions between nanoresonators. The full simulations revealed that these relatively weak higher order interactions do

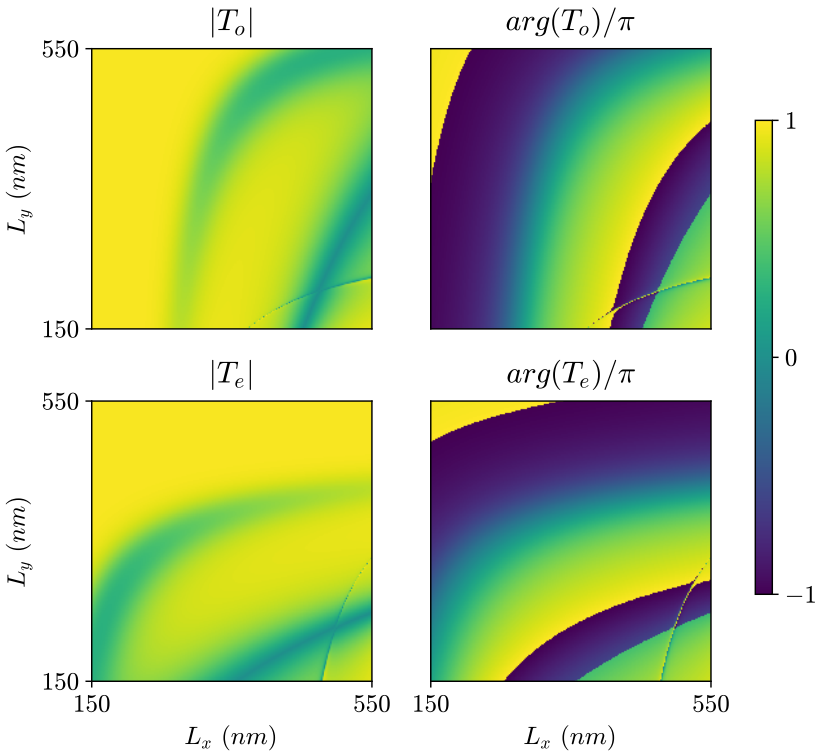

FIGURE 2.4: Numerical simulation of transfer matrix of silicon cuboidal resonators on glass substrate, with a silicon height of $700nm$ and refractive index $n = 3.486$ and a periodicity of $800nm$. Shown here are the magnitudes of transmitted light in the ordinary and extraordinary axes against the physical sizes of the pixels (L_x, L_y) varying from $150nm$ to $550nm$.

exist for some configurations, particularly ones with subpixels that have relatively small pairwise separations. Knowing that both the solutions to Eq. 2.6 and the single resonators implementing a given degree of birefringence are non-unique, we are thus able to design metasurfaces while giving minimal consideration to higher order interactions, simplifying the process greatly.

While the analytical design based on Eq. 2.16 and the linear sum of pixels, it was found to be necessary to perform secondary optimization passes using CST Studio to fine-tune the parameters for real physical conditions. These optimization passes targeted the phase-invariant fidelity measure, which we will now define. We define first the Jones transfer matrix elements $\mathbf{T}_{ij}^{(n)}$ and $\mathbf{T}_{ij}^{(t)}$, where the superscript (t) and (n) denote the design target and numerically simulated transfer matrix respectively, and the subscripts i, j denote the index of the element. We then assert that some unknown value τ scales the target transfer matrix such that for all indices i, j, the difference δ may be minimized:

$$\delta = \sum_{i,j} \left| T_{ij}^{(n)} - \tau T_{ij}^{(t)} \right|^2 .$$

Minimizing the value of δ with respect to τ, we find that this minimum value of τ to be

$$\tau = \frac{\sum_{i,j} T_{ij}^{(n)} T_{ij}^{(t)*}}{\left| T_{ij}^{(t)} \right|^2}$$

By solving these two equations, we arrive at the expression

$$\delta = \frac{1}{\sum_{i,j} \left| T_{ij}^{(t)} \right|} \left[\sum_{i,j} \left| T_{ij}^{(n)} \right| \sum_{i,j} \left| T_{ij}^{(t)} \right| - \sum_{i,j} \left| T_{ij}^{(n)*} T_{ij}^{(t)} \right|^2 \right]$$

Finally, we normalize the right side elements, and arrive at a phase-invariant measure of fidelity

$$\delta = 1 - \frac{\left| \sum_{i,j} T_{ij}^{(n)*} T_{ij}^{(t)} \right|^2}{\sum_{i,j} \left| T_{ij}^{(t)} \right|^2 \sum_{i,j} \left| T_{ij}^{(n)} \right|^2}. \tag{2.18}$$

This fidelity measure was used for the final optimization step, aiming to minimize the difference between the numerically simulated transfer matrix and the target with a simple gradient descent algorithm. While this optimization step is insensitive to overall efficiency, only fine variations of the nanoresonator parameters were allowed, preserving the high efficiency of the initial design obtained from the linear combination of resonators design step and subsequently to CST Studio while suitably eliminating near-field interactions.

The metasurfaces were fabricated at the ANU node of Australian Nanofabrication Facility (ANFF). First, an amorphous-silicon thin film of approximately

710nm thickness was prepared using Plasma-Enhanced Chemical Vapor Deposition (PECVD) on a 170μm thick glass substrate. This sample was then characterized for its specific refractive index and thickness, both of which are known to vary slightly between different runs of deposition. These newly obtained values were then used to iteratively refine and re-simulate the design numerically to ensure that the final design conformed to the deposited film as closely as possible.

Using these finalized parameters, etching was carried out via Electron Beam Lithography (EBL) and Inductively Coupled Plasma (ICP) etching. Varying exposures (from approximately 150μCcm^{-2} to 200μCcm^{-2}) were utilized to produce a small range of metasurfaces with slight variations in sizes to account for fabrication variances.

During the fabrication, the dimensions of the fabricated structures may be different from the designed values due to variations of the fabrication conditions in the electron beam lithography and etching. In order to compensate for the possible fabrication errors, for any given single design, we patterned the same dimension multiple times using different doses during the electron beam lithography, effectively tiling the metasurface multiple times across a single substrate. This is, in essence, a form of stochastic error compensation; by both increasing and decreasing the 'ideal' dose for a given patterning process, we are able to trial-and-error a small range of physical dimensions of the metasurface, and in subsequent characterization, we may choose the best-fit metasurface to suit the original design specifications. Once characterized, the transfer matrix may be considered known with precision limited only by the experimental setup (as opposed to the limitations of fabrication) and thus, well defined and usable for experiment, the fabrication errors having been accounted for in experiment and data analysis.

This general design and fabrication technique was used throughout the duration of my thesis.

2.4 Experimental realization of complex birefringence

After the fabrication of the metasurface[1], characterization was carried out in the classical regime.

The fabricated metasurfaces were characterized using the experimental setup illustrated in Fig. 2.2(e). A variable-wavelength laser operating in the $1500-1575$nm telecommunication range was used as the light source, and input polarization states were prepared from this laser using a fixed linear polarizer (Pol_1) and a motorized half-wave plate (HWP). A 50:50 beam splitter (BS) and detector were introduced immediately after the state preparation to provide a normalization baseline for the

[1]Fabrication was performed by Khosro Zangeneh Kamali using facilities at ANU's ANFF

measurements. A lens focused the beam to an approximate 80μm spot normally incident on the metasurface, followed by an objective lens used to image the transmitted light. To exclusively collect zero-th order transmitted light, a Fourier lens was used to exclude higher orders of diffracted light. At times, an additional diaphragm to further limit the capture of the diffracted light was incorporated before the Fourier lens Finally, the polarization was characterized via a motorized quarter-wave plate (QWP) and a linear polarizer (Pol_2) to project the transmitted state onto a varying basis, with the resultant power captured with an infrared photodiode power detector. These measurements were performed multiple times for any given state and wavelength, typically 10 measurements per datapoint, and the average taken to ensure that any physical environmental factors were excluded, as well as to obtain an accurate estimation of random, systemic variation. This process was automated using a script written in Python, capable of controlling the laser, waveplates, and power meters.

The Jones matrix of the metasurface was then reconstructed by performing a normalized least mean squares (nLMS) fitting the measured power ratio to the form:

$$P_{ratio} = ||\langle\theta_{\text{Pol}_2}|\mathbf{QWP}(\theta_{Q1})|\mathbf{T}|\theta_{in}\rangle||^2 \tag{2.19}$$

where θ_{Pol_2} is the orientation angle of the linear polarizer (Pol_2), $|\theta_{in}\rangle$ is the input linear polarization state at an angle of θ_{in} selected by a corresponding rotation of HWP, $\mathbf{Q}(\theta_Q)$ is the transmission matrix of the quarter-waveplate rotated at an angle θ_Q, and P_{ratio} is the ratio of the measured powers at the detectors A and B. This allows for accurate and unique reconstruction of the transfer matrix, up to a global phase [57]. Exclusively in this chapter, we also assume that the transfer matrix is symmetrical, allowing only one quarter waveplate to be used to fully condition and calculate a unique transfer matrix. Details are provided in Appendix A. This numerical reconstruction was performed using Python, utilizing the differential evolution optimizer as implemented by SciPy [58] to locate global minima. This allowed for relatively simple avoidance of local minima in a strongly multivariate problem.

Here, I demonstrate the first experimental realization of a metasurface that can transform a pair of very close polarizations into orthogonally polarized states. Specifically, we aim to demonstrate the transformation sketched in Fig. 2.1, transforming from the input linear polarization states $|A_i\rangle = |41°\rangle$ and $|B_i\rangle = |49°\rangle$ to the output states $|A_t\rangle = |0°\rangle$ and $|B_t\rangle = |90°\rangle$ [Fig. 2.1(right)]. The theoretical framework as outlined was employed to determine the transfer matrices required, and converted to a practical physical design that was then fabricated. Fig. 2.5(a) shows the scanning electron microscopy (SEM) image of the fabricated metasurface which was subsequently characterized under the classical regime.

I measured the optical transmission through the metasurface using the setup outlined in Fig. 2.2(d), and reconstructed the experimental parameters of the metasurface transfer matrix, as shown in Figs. 2.5(b,c) for the wavelength of

1563nm. As discussed, a fitting was performed, minimizing the normalized least mean squares difference between Eq. 2.19 and the measured power ratio to a value of 4.1×10^{-7}, with a maximum standard deviation in data of $7.2 \times 10^{-7} W$. This metasurface, as measured, realizes a transformation of the nearby input states to the near-orthogonal output states $|A_t\rangle = |0.3 \pm 0.7^\circ\rangle$ and $|B_t\rangle = |89.8 \pm 0.7^\circ\rangle$, in accordance with the theoretical design.

The singular value decomposition of the transfer matrix quantifies the efficiency of the metasurface, and as such, I determined these to be $\sigma_1 = 0.751$ and $\sigma_2 = 0.138$, corresponding to the maximally and minimally transmitted linear polarization states $|\mathbf{W}_1\rangle = |135^\circ\rangle$ and $|\mathbf{W}_2\rangle = |45^\circ\rangle$. Of note is that the maximum singular value σ_1 is substantially below 1, indicating that the metasurface has a transmission of approximately 56%, unlike the fully transmissive analytical design. It is likely that this arises from experimental concerns with losses arising from reflection and deviations from the numerical design, as well as potential angular dispersion due to the focusing of the laser on the metasurface. These can be improved in future works with higher quality sample fabrication, as well as the incorporation of an anti-reflection coating to the substrate. Despite this, however, the ratio of σ_2/σ_1 is substantially less than 1, demonstrating strong polarization dependent transmission, in accordance with the theoretical design for complex birefringence.

Regardless of the less than ideal transmission efficiency, however, this metasurface performs as expected. Under a classical regime, we demonstrate that the metasurface can map nearby polarization states into well resolved orthogonal states, in accordance with the original design concept as shown in Fig. 2.1. In Fig. 2.5(d), the solid blue line represents a dependence of the output vs. input linear polarization angle. For the input states around $|\mathbf{W}_2\rangle = |45^\circ\rangle$, there is an enhanced responsivity of the output polarization with respect to small changes of the input state, shown as the steepness of the gradient, since $\mathrm{d}\theta_{out}/\mathrm{d}\theta_{in} \simeq 3.7 > 1$. In particular, the dashed lines mark the two close input polarizations which are mapped to orthogonal states at the output, in accordance with Fig. (2.1). Conversely, at input polarization angles around $|\mathbf{W}_1\rangle = |135^\circ\rangle$, the metasurface provides the opposite effect, bringing well-separated polarization states closer together. We note that the increased responsivity is associated with a minimum of power transmission [dashed-dotted line in Fig. 2.5(d)], which is the necessary and inevitable tradeoff for the implementation of such functionality in all-dielectric structures without amplification.

Also characterized was the responsivity of mapping linear polarization states across a range of wavelengths, of which the results are shown in Fig. 2.5(e). The visible oscillations vs. wavelength with a period of about $3nm$ (with peak-to-peak amplitude up to 15% of the transmission amplitude) are consistent with the Fabry-Perot interference due to the 170μm thick glass substrate used in the experimental sample. We conclude, therefore, that these oscillations arise from the internal reflection of laser light of the glass substrate, and in future works, these may be reduced by applying an anti-reflection coating if not desired.

In the specific case of this thesis, the interference fringes may be considered acceptable. While they do in fact alter the the transformation of the state, affecting as they do the transmission of the metasurface, we may consider individual wavelengths independently of each other, and evaluate the performance accordingly. As such, regardless of these interference fringes, the increased responsivity is consistently notable around the input angle $|\mathbf{W}_2\rangle = |45°\rangle$, for a wavelength range $1550-1570$nm, as seen in Fig. 2.5(e). This demonstrates that a relatively wide bandwidth of operation is attainable, and can be further enhanced by specially optimizing the nano-resonator design and introducing anti-reflection coating on the substrate.

Under our scheme, it is possible to transform between arbitrary input to output pairs of polarization states, including any elliptical ones. As an illustration of these principles, we show in Fig. 2.6 the application of the general approach to the following pairs of input states,

$$|A_i\rangle = \begin{bmatrix} \cos(29.1°) \\ \sin(29.1°)e^{-i\,0.5\pi} \end{bmatrix}, \quad |B_i\rangle = \begin{bmatrix} \cos(27.5°) \\ \sin(27.5°)e^{-i\,0.7\pi} \end{bmatrix}$$

and the target output states

$$|A_t\rangle = \begin{bmatrix} \cos(41.6°) \\ \sin(41.6°)e^{i\,0.25\pi} \end{bmatrix}, \quad |B_t\rangle = \begin{bmatrix} \cos(49.0°) \\ \sin(49.0°)e^{i\,0.82\pi} \end{bmatrix}$$

We designed and numerically optimized a metasurface which achieves theoretical transmission values of $\sigma^2_{max} = 0.828$ and $\sigma^2_{min} = 0.0324$. Notably, this design targets elliptical states instead of the linear ones shown in Fig. 2.5, demonstrating the additional degree of freedom in the rotation of the metasurface pixels. However, while this design has a maximum singular value *near* to 1, it does not attain a maximumally transmitted value even in analytical design. As discussed in Section. 2.2, this analytical shortfall arises from the lack of chirality in the formulation of the equations, and may be remedied in future works by the implementation of chiral meta-pixels. This design was then fabricated and experimentally characterized using the same experimental technique as outlined above.

The characterized results were shown in Fig. 2.6, with the transfer matrix and relevant state transformation plotted in the Poincaré sphere. As can be seen in the figure, the transformation of states is highly elliptical, demonstrating the capability of our metasurface of performing the transformations as expected. However, the transmission efficiencies measured were lower than expected, with a maximum transmission efficiency for $|A_i\rangle$ of 34.9% at 1557nm. As before, this is likely attributable to the experimental and fabrication concerns, in particular, it is likely that angular dispersion of the beam may be responsible in large part for the divergence. The metasurfaces fabricated were limited to $100 \times 100\mu m$ in size, and as mentioned, the beam was focused to an approximately $80\mu m$ diameter spot. The metasurface is designed strictly for normal incidence, and the deviation from normal incidence of the beam due to the tight focusing is likely to cause substantial

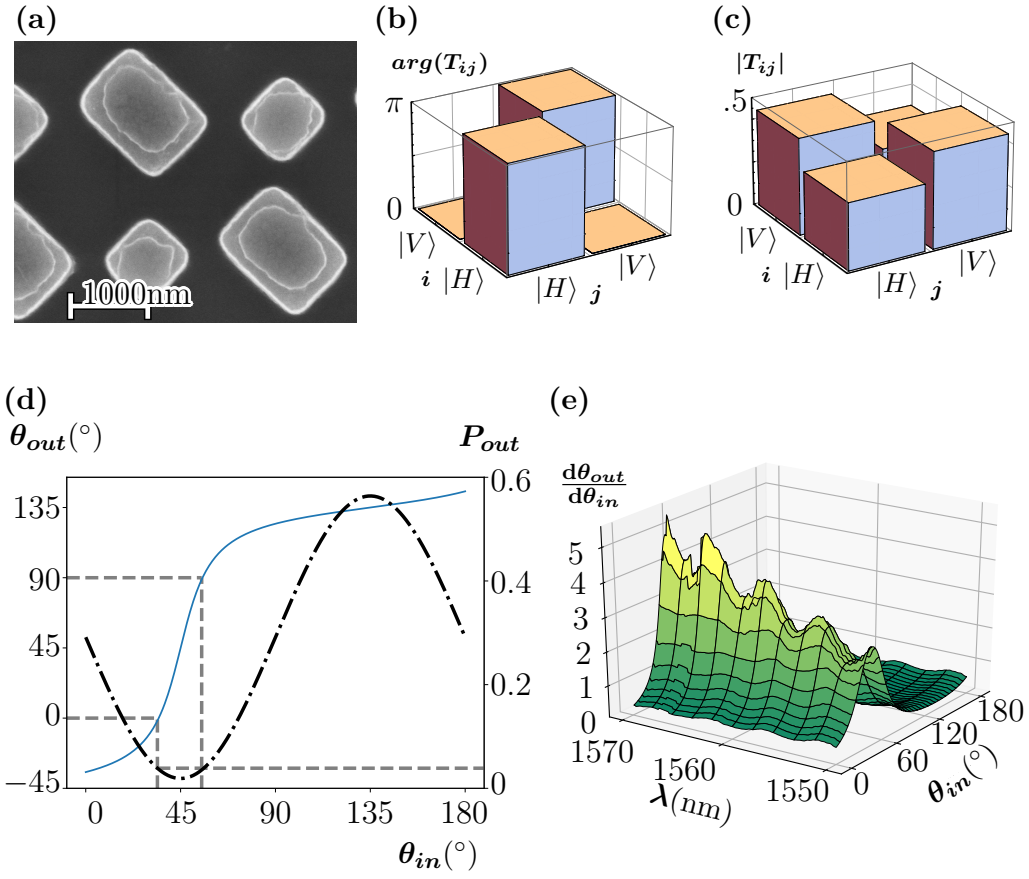

FIGURE 2.5: Experimental results for a metasurface designed to bring nearby states into orthogonal ones. (a) Scanning Electron Microscope (SEM) image of the manufactured metasurface. (b,c) Experimentally characterized arguments (b) and absolute values (c) of the polarization transfer matrix $\mathbf{T}$ of the metasurface at a wavelength of 1563nm. (d) Experimentally derived angular resolution of input linear polarization states denoted by $|\theta_{in}\rangle$ to the output states $|\theta_{out}\rangle$ and net transmitted power P_{out}, calculated at 1563nm (scaled against input power of 0.995mW). Marked by dashed lines are the corresponding two states denoted by the arrows in Fig. 2.1. (e) Responsivity $d\theta_{out}/d\theta_{in}$ vs. the input wavelength and polarization angle.

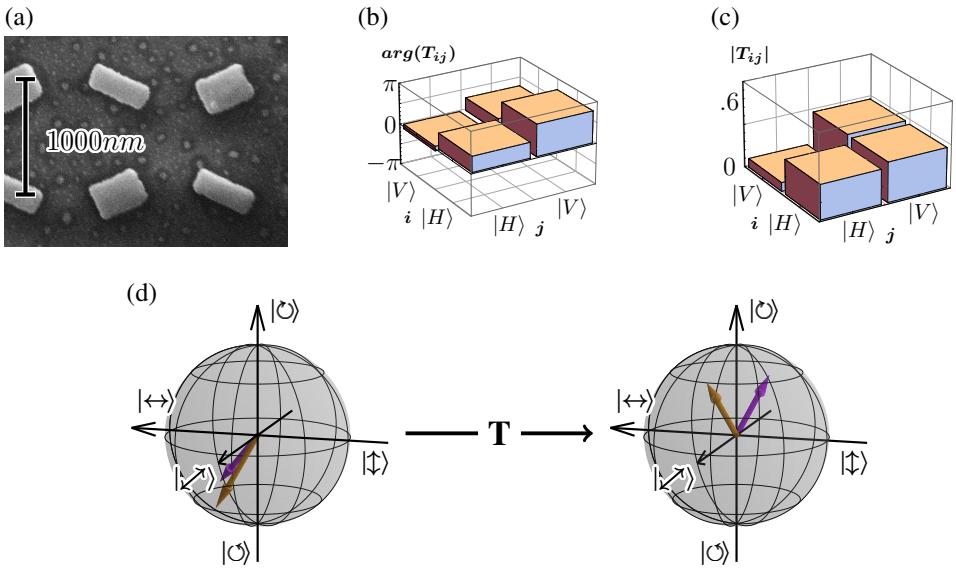

FIGURE 2.6: Experimental results for a metasurface designed to transfer two elliptical polarization states to other chosen states. (a) Scanning Electron Microscope (SEM) image of the manufactured metasurface. (b,c) Experimentally characterized arguments (b) and absolute values (c) of the polarization transfer matrix **T** of the metasurface at a wavelength of 1557nm. (d) The transformation of states calculated from the numerical model.

effects with regards to the quality of the transformation. Unfortunately, due to experimental constaints, this was not characterized in detail.

These results demonstrate conclusively that the concept of complex birefringence is attainable in practical terms. Not only does the fabricated metasurface demonstrate the desired polarization transformation in shifting a pair of nearby polarization states to a pair of fully orthogonal ones, it also demonstrates a relatively high efficiency. While this efficiency is lower than is ideal, it is hoped that future works can explore this particular aspect, and potentially address it via improved fabrication techniques.

2.5 Summary

In this chapter, I have developed and expanded on the concept of a novel form of polarization control relying on judiciously engineered loss to effect nonconservative control over polarization states, termed complex birefringence. This is achieved in a monolithic, dielectric metasurface, complementing the analytically optimal theory. This technique was implemented in experiment using a binary metasurface, with appropriate characterization and experimental procedure verifying that the control may be attained under realistic conditions and over a broad range of wavelengths, promising great suitability for replacement of conventional bulk optical methods of

attaining similar effects in both classical and quantum experiments. We anticipate that this platform may be extended to a great many uses, especially in cases where compactness and lightweight control over polarization is required.

A notable area of expansion and development would be the consideration of chirality in the transfer matrix. This work as presented restricts itself solely to a symmetrical transfer matrix and thus achiral metasurface, limiting the degrees of freedom utilized in the transformation. With reference to Section 2.2, we note that a higher efficiency could be potentially achieved for some states by expanding a range of transformations to include asymmetric matrices, which would require tackling the nontrivial design task of metasurfaces with a chiral response [50]. Some consideration of this is made in Section 5, however, it is not extensively considered in my thesis.

Chapter 3

Transformation of biphoton states

Complex birefringence also paves the way towards arbitrary transformation of biphoton polarization states in a highly compact package. In quantum optics, biphoton polarization states are an extremely common fixture; for example, arguably the most common source of entangled photons, Spontaneous Parametric Down Conversion (SPDC) production, produces photons that are entangled in polarization (among other properties). It follows that the manipulation of such states is an utterly fundamental aspect of experimental and practical implementation of quantum optics, seeing uses in fields of increasing interest such as quantum computing and quantum cryptography [59, 60]. Accordingly, new ways to manipulate such states will greatly facilitate such developments. Complex birefringence, especially as implemented here with single metasurfaces, presents just such an avenue for control and transformation.

Complex birefringence, a concept I presented in Chapter 2, provides a ready answer to accomplishing this task. Conventional birefringence may *only* rotate these states in parallel to each other across the surface of the sphere, maintaining the relative angle under all transformations. Complex birefringence, by contrast, enabling as an additional degree of freedom the divergence (or convergence) of these states. As such, among other things, the non-Hermitian transformations expressed in the form of complex birefringence allows for the tuning of the degree of entanglement of entangled pairs of photons. Such non-Hermitian transformation of polarization states further opens new regimes for the non-conservative manipulation of quantum states and photon interference [61, 62, 63]. Non-conservative transformations can also underpin the construction of optical neural networks [64].

In this chapter, I describe and analyze the application of complex birefringence to quantum light, demonstrating through theoretical analysis as well as characterized results that this novel form of polarization control is both useful and practical for such usecases. Not only do I extend the transformation and manipulation as outlined in Chapter 2 to quantum light, I also demonstrate that this offers fundamentally novel and powerful control over entanglement, which is a critical aspect to many prospective applications.

Two-photon states, also known as biphoton states, are a strict subset of the more general Fock state, involving only two photons, as suggested by the name.

Despite this restriction, or perhaps because of it, biphoton states nevertheless remain a common and useful part of quantum experiments, arguably comprising a majority of currently extant experiments and research efforts, for example, quantum two-level systems [65], quantum communication [66] and the aforementioned entangled photon states such as might be used for quantum teleporation [67], quantum cryptography, and many other areas of quantum optics, both fundamental and practical [68, 69, 70].

SPDC is an especially ubiquitous source of temporally correlated photons, having arguably changed the entire field of quantum optics, fundamentally enabling many of the aforementioned fields to exist in the current day [71]. Biphoton sources have been demonstrated in numerous different media, ranging from bulk crystals to waveguides, or even two-photon emission in semiconductors [72, 73]. Regardless of the physical implementation, SPDC setups are regarded as one of the most reliable and readily available sources of biphotons, and are yet more attractive for their relatively simple technical designs. They allow for flexible generation of temporally correlated pairs of photons, which may be entangled in polarization, frequency, angular momentum, or not at all, depending on the exact specifics of this setup.

Of interest for the purposes of this thesis are the photons distinguishable in the polarization states. SPDC, as implied by the name, is a phenomenon where a pump photon of higher energy decays into two lower energy photons, obeying the so-called phase matching conditions, which are themselves consequences of the conservation of energy and momentum of the photons [72]. The specific manner in which these conditions are fulfilled are dependent on the SPDC medium, and are categorized into Type I and II SPDCs, which can emit photons in the states

$$|\Psi_I\rangle = \frac{|HH\rangle + e^{i\phi}|VV\rangle}{\sqrt{2}}, \quad |\Psi_{II}\rangle = \frac{|HV\rangle + e^{i\phi}|VH\rangle}{\sqrt{2}}.$$

Notably, the polarization states produced are relatively inflexible, and based on the physical parameters of the SPDC source. Varying the polarization and degree of entanglement are done in post-generation, and typically using bulk optical setups, or some integrated optical circuit such as in the case of waveguide-based SPDC. However, complex birefringence offers the possibility of manipulating these output states in their polarization degree of freedom in a single structure, potentially paving the way towards far more efficient and compact SPDC implementations.

Weak measurements are of further interest as a relatively new tool used in quantum experiments. They are performed by integrating the signal over time, in effect weakly perturbing the system, as opposed to an instantaneous, projective (strong) measurement [74]. These are applied in cases where there is a limitation in how strong a signal may be obtained from a system; for practical reasons such as limiting the coupling between the detector and the system to be measured so as to avoid disturbing the system to be measured. This lends further benefits such as effectively acting as a frequency filter for noise, assuming of course that the source

of the noise is periodic in nature.

As implied by the name, weak measurements are performed by coupling the measurement weakly to the system to be observed. This weak coupling allows the measurement to avoid strongly perturbing the system, and consequently, avoids collapsing the system. In general, this allows for measurements of ongoing time evolution of systems, such as in Hardy's paradox [75], and by resolving the paradoxical impossibility of inferring a system's temporal evolution from its final outcome, is an important tool for quantum measurements. These are applicable in both general quantum experiments, as with particle-antiparticle pairs, but also in optical experiments. However, these weakly-coupled measurements are not easy to achieve experimentally, and in the case of polarization measurements, necessarily require very specific polarization transformations [76, 77]. Developing complex birefringence for such polarization control will only help to advance the capabilties of weak measurements, paving the way towards more flexible implementations.

This unconventional polarization transformation is of further interest in particular to quantum computing. With the potential for arbitrarily controlling the polarizations of a biphoton state into arbitrary output states, such metasurfaces may be used to implement states with photons confined exclusively to some combination of one polarization state or the other, known NOON states for their wavefunction representation as $|N,0\rangle + |0,N\rangle$. These states are of particular interest to quantum information applications, and can form the basis for quantum optical logic gates [78, 79].

The manipulation of biphoton states is not a trivial task, whether it be in the discussed NOON state, or some other ensemble. Typical methods for manipulating these states revolve around the splitting of the biphotons along separate paths, individual control, followed by their recombination [80]. This inevitably requires the selection of the photons, in some manner, such as a Fock state filter, as well as temporally-adjusted paths similar to the construction of a Mach-Zehnder interferometer, none of which are trivial tasks to achieve in experiment. Mechanical precision is a particular concern, especially outside of laboratory situations where stray vibrations and physical robustness are a major concern. Even in the case of a purely waveguide-integrated manipulation structure [81], these designs are non-trivial.

The extension of complex birefringence into the manipulation of quantum light thus forms the basis for solutions to many of these problems. Not only is complex birefringence highly versatile, providing arbitrarily-designed solutions to these manipulations, they are also monolithic and physically robust, providing a highly attractive alternative to existing approaches.

3.1 Biphoton states

Two-photon correlated states are notably common, in particular, as a result of SPDC emission [72], with quantum dots being another source of two-photon states in literature. Polarization entanglement is an especially common degree of freedom utilized in experimental uses, for example, in quantum information transmission, cryptography, and computation [82]. Manipulation of these polarization states and associated entanglements is as always a non-trivial task, requiring the implementation of multiple bulk optical elements and, in most cases, mechanical adjustments.

As with any other quantum state, pure states may be represented by their wavefunctions, which can be written in the form:

$$|\Psi\rangle_{AB} = \sum_{i,j} c_{ij} |i\rangle_A \otimes |j\rangle_B, \tag{3.1}$$

where $c_{i,j}$ are real, positive coefficients defining the probability amplitudes, and $|k\rangle_\chi$ represents the photon χ in k basis state, of which the full set of $|k\rangle$ states forms a complete, orthonormal basis. It is always possible to express this in a form such that

$$|\Psi\rangle_{AB} = \sum_{n} \sqrt{\lambda_n} |\tilde{i}\rangle_A \otimes |\tilde{j}\rangle_B, \tag{3.2}$$

where the set $|\tilde{k}\rangle$ again form a complete, orthonormal basis, and $\sqrt{\lambda_n}$ are known as the Schmidt coefficients. n is known as the Schmidt rank, and is given by the minimum of the dimensionalities of the original basis states, and in turn, this is known as the Schmidt decomposition k[83]. In the case of a biphoton state, these coefficients and basis states may be obtained exactly from the singular value decomposition of the 2×2 matrix given by c_{ij}, taking i and j to index positions in the matrix, and thus giving $n = 2$.

These Schmidt coefficients may be used to quantify the entanglement of the system, namely, the system is unentangled if and only if there is only one non-zero Schmidt coefficient. In a multi-part system such as a two-photon state, any combination of two non-zero Schmidt coefficients defines an entangled system, with the degree of entanglement increasing towards a maximum for equal, non-zero values. It is reasonable, therefore, to define some combination of the Schmidt coefficients that gives a singular, scalar value that quantifies the entanglement of the system. Several such formulations exist, however, for the purposes of this thesis, I will be using the cooperativity parameter, sometimes known as the Schmidt number. This is given [84] by:

$$Q = \frac{\left(\sum_n \lambda_n\right)^2}{\sum_n \lambda_n^2}. \tag{3.3}$$

This value ranges with minimal to maximal entanglement from 1 to 2, providing a way to readily evaluate the entanglement of a given system.

In this chapter, I will be visualizing biphoton polarization states on a Poincaré sphere, and as such, I will first establish an understanding of the equivalence to its conventional wavefunction representation, based primarily on the work of Chekhova et al. [59]. We first consider the standard form of an entangled biphoton wavefunction, such as one produced by an SPDC source, assuming without loss of generality that only a single spatial and frequency mode exists, and write the wavefunction explicitly as:

$$|\Psi\rangle = c_1|2,0\rangle + c_2|1,1\rangle + c_3|0,2\rangle + |0,0\rangle, \tag{3.4}$$

where the kets $|m,n\rangle$ represent a state with m number of photons in a chosen polarization state x (for example, $|H\rangle$) and n photons in its orthogonal polarization state y (as a matching example, $|V\rangle$), and $|0,0\rangle$ represents the vacuum state. Since the photons are assumed to be indistinguishable in spatial and frequency modes, the $|1,1\rangle$ state comprises two photons that may be distinguished exclusively on their polarization states. c_1, c_2, and c_3 are complex coefficients determined by the nature of the source, and by the normalization condition, we know that:

$$\langle\Psi|\Psi\rangle = 1 = |c_1|^2 + |c_2|^2 + |c_3|^2.$$

Discarding the vacuum state as irrelevant and expressing each coefficient in Euler notation and discarding global phase as an arbitrary value we may choose, we further express these coefficients as:

$$c_1 = d_1, \quad c_2 = d_2 e^{i\varphi_2}, \quad c_3 = d_3 e^{i\varphi_3},$$

where d_1, d_2, and d_3 are again related via the normalization condition such that $d_1^2+d_2^2+d_3^2 = 1$, resulting in four real variables defining all three complex coefficients. We now define the photon creation operators $a_x^\dagger$ and $a_y^\dagger$, in the same basis states as used in Eq. 3.4, and define further that an arbitrary photon creation operator exists as:

$$a^\dagger(\vartheta,\varphi) = \cos\frac{\vartheta}{2}a_x^\dagger + e^{i\varphi}\sin\frac{\vartheta}{2}a_y^\dagger.$$

These parameters are bounded by $\vartheta \in [0,\pi]$ and $\varphi \in [0,2\pi]$. This allows us to write an equivalent representation of Eq. 3.4 as:

$$|\Psi\rangle = \frac{a^\dagger(\vartheta_a,\varphi_a)a^\dagger(\vartheta_b,\varphi_b)|vac\rangle}{||a^\dagger(\vartheta_a,\varphi_a)a^\dagger(\vartheta_b,\varphi_b)|vac\rangle||} \tag{3.5}$$

They are related by construction, giving us the coefficients (choosing d_2 to be represented in terms of d_1 and d_3):

$$\begin{aligned}
\varphi_3 &= \varphi_a + \varphi_b, \\
d_1 &= \frac{\sqrt{2}\cos\frac{\vartheta_a}{2}\cos\frac{\vartheta_b}{2}}{\xi}, \\
d_3 &= \frac{\sqrt{2}\cos\frac{\vartheta_a}{2}\cos\frac{\vartheta_b}{2}}{\xi}, \\
\cos\varphi_2 &= \frac{\cos\varphi_a \sin\frac{\vartheta_a}{2}\cos\frac{\vartheta_b}{2} + \cos\varphi_b \sin\frac{\vartheta_b}{2}\cos\frac{\vartheta_a}{2}}{d_2\xi}, \\
\sin\varphi_2 &= \frac{\sin\varphi_a \sin\frac{\vartheta_a}{2}\cos\frac{\vartheta_b}{2} + \sin\varphi_b \sin\frac{\vartheta_b}{2}\cos\frac{\vartheta_a}{2}}{d_2\xi}, \\
\xi &= \sqrt{1 + \cos^2\frac{\vartheta_a - \vartheta_b}{2} - \sin\vartheta_a \sin\vartheta_b \sin^2\frac{\varphi_a - \varphi_b}{2}}.
\end{aligned} \tag{3.6}$$

An inversion of these relations give us a mapping from the coefficients of an arbitrary biphoton state to a basis in $\{\vartheta_a, \varphi_a, \vartheta_b, \varphi_b\}$, which we may see can be used as the polar and azimuthal angles to plot a pair of points on the surface of a sphere. As such, this is a convenient visualization of a biphoton states as a pair of points on a Poincaré sphere, and will be used throughout this section to provide a visual reference for the transformation of these biphoton states.

Visualizing these biphoton polarization states on a Poincaré sphere also allows us a ready, visual intuition of the degree of entanglement of any given biphoton state. In Fig. 3.1, we see three examples of polarization states, which are represented both in terms of their respective Poincaré spheres, as well as their wavefunctions as in 3.1. These are all pure states with photons indistinguishable in spatial and frequency modes, and as such, the diagonal terms are equal. It is important to note that due to the quantum nature of the biphoton state we are visualizing, these are not the representations of two *individual* photons that are in the polarization states represented by each vector arrow, rather, *both* vectors combined represent a *single* biphoton wavefunction. Notably, we see that as expected, fully orthogonal polarization states are maximally entangled, and a pair of identical polarization states are minimally entangled seen in Fig. 3.1(a) and (b) respectively, with Schmidt numbers of 1 and 2. And finally, in Fig. 3.1(c), we see a partially entangled state, with a Schmidt number of $Q = 1.275$. Notably, we see that at the minimum $Q = 1$, the vectors representing the biphoton state overlap exactly, representing their indistinguishability, and as the Schmidt number increases towards a maximum of 2, the vectors representing the component states on the Poincaré sphere diverge, to a maximally diverged state of two vectors facing fully away from each other, corresponding to fully distinguishable, orthogonal states. Finally, with the partially entangled states, the vectors are in between these two extremes. This is in line with theoretical expectations, and provides a visual comparison of the degree of entanglement in any given biphoton state.

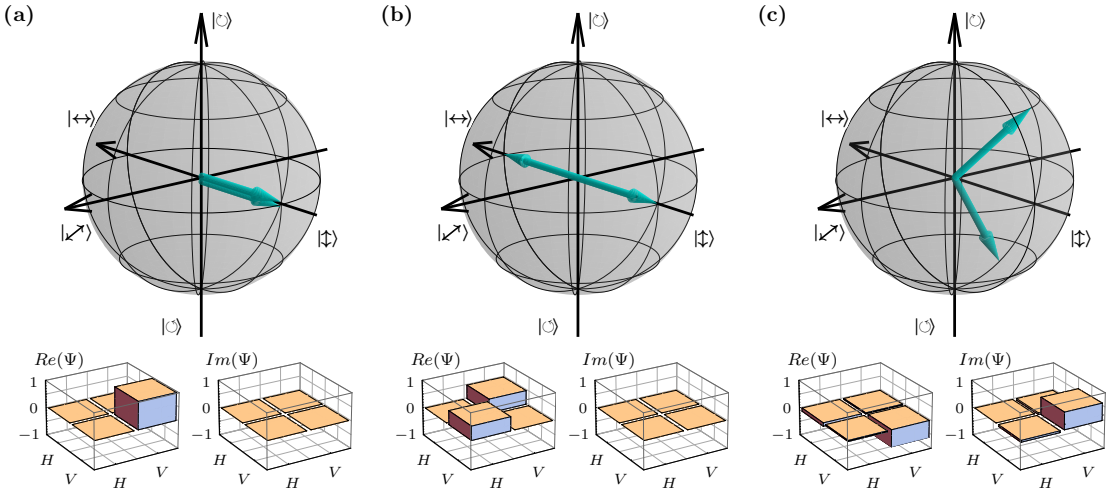

FIGURE 3.1: Examples of polarization-correlated biphoton states shown in Poincaré sphere representation, with the states represented as pairs of arrows as well as in the wavefunction basis, shown as the real and imaginary parts of Ψ in the bar graphs. (a) $|0,2\rangle$ state, with both photons in the vertical polarization state and a Schmidt number of $Q = 1$ (no entanglement). Note that the arrows representing the states have been offset slightly purely for visual clarity. Under a true representation, they would overlap fully. (b) $|1,1\rangle$ state, with photons in orthogonal horizontal and vertical states, with a Schmidt number of $Q = 2$ (maximum entanglement). (c) Photon state with arbitrary polarization correlation, with a Schmidt number of $Q = 1.275$ (partial entanglement).

3.2 Complex birefringence for transformation of biphoton states

We now consider a mathematical treatment of the concept. The action of the metasurface on a two-photon state will, in general, produce a superposition of pure two-photon and mixed single-photon states, the latter of which occurring when one of the paired photons is lost. These states can be distinguished through conditional detection schemes. We express this transformation as:

$$|\Psi(A_i, B_i)\rangle \xrightarrow{\mathbf{T}} |\Psi(\mathbf{T}A_i, \mathbf{T}B_i)\rangle = |\Psi(A_t, B_t)\rangle, \tag{3.7}$$

where the subscripts i and t correspond to the input and transformed states after the metasurface, respectively. This is analogous to the classical case described above in Chapter 2, and it therefore follows that the same approaches we have already formulated may be applied to achieving simultaneous, independent transformation of a pair of polarization states using a single metasurface, described mathematically and schematically in Eq. (2.16) and Fig. 3.4(a).

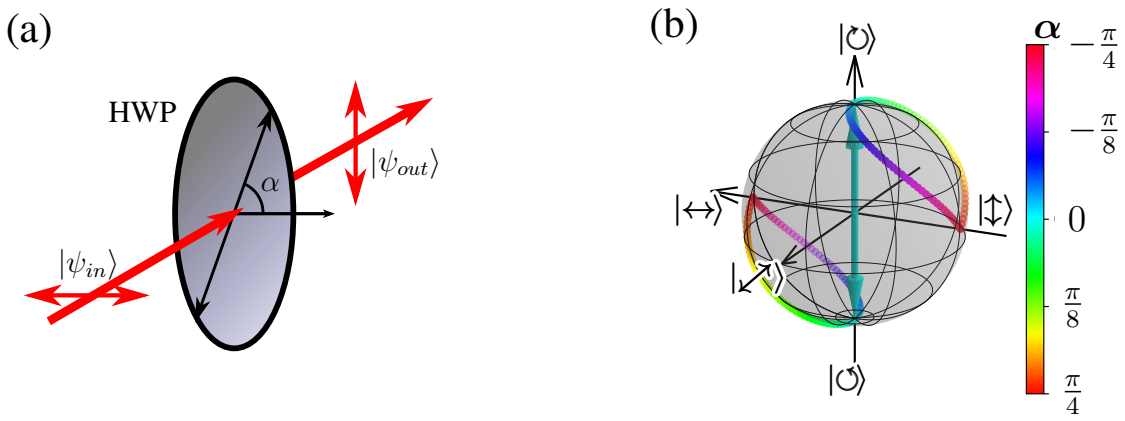

FIGURE 3.2: Conventional polarization transformation of $|\Psi(H, V)\rangle$ entangled input state by an ideal $(\pi/2)$ phase retarder rotated at angle $\alpha°$, shown in schematic in (a) with a half-wave plate and (b) as a Poincaré sphere representation of biphoton states.

As previously discussed with Eq. 2.1, conventional birefringence does not offer the degree of freedom required to attain independent transformation of pairs of states; specifying the transformation of one state necessarily specifies the transformation of the other. This may be seen visually in Fig. 3.2, where the action of conventional birefringence is numerically demonstrated, using an ordinary half-waveplate as the birefringent transformation. Starting with a pair of horizontal and vertical polarization states, which are naturally orthogonal to each other, the states were transformed by the waveplate rotated to an angle of α, given by $\mathbb{R}(-\alpha) \cdot \mathbf{H} \cdot \mathbb{R}(\alpha)$, where $\mathbb{R}(\alpha)$ represents the two-dimensional rotation matrix at the angle α. The output polarization states were plotted across the surface

of the Poincaré sphere in Fig. 3.2(b), with the colours of the points representing the waveplate angle α. As can be seen from the plot, at no point are the output polarization states anything but orthogonal to each other, demonstrating that the states are rotated in parallel to each other, and thus degree of entanglement is unchanged under conventional birefringence.

Complex birefringence alleviates this constraint, and may be easily visualized in Fig. 2.1. Instead of locking the biphoton states to rotate in parallel to each other across the surface of a Poincaré sphere, a complex birefringent transformation allows them to diverge from each other, with the distortion of the gridlines in Fig. 2.1 demonstrating the overall distortion of the states. We can readily see that in the case of a biphoton state, such a transformation would, in fact, allow for the modification of the degree of entanglement between the photons, allowing for unprecendented control over biphoton states in a monolithic structure. Conventional approaches to this concept would typically operate by splitting the beam path by their polarizations along a Mach-Zender interferometer path, with optical elements placed along one or the other path to perform the required transformations to the biphoton states.

We then consider the experimental potential of tailored two-photon manipulation and quantum state transformation[1]. Recent studies demonstrated that photon interference at lossy couplers can demonstrate unconventional features, including a transition between bunching and anti-bunching statistics [85, 62]. These studies were based on plasmonic structures, comprising metallic metasurfaces, and as such, inherent losses associated with the metallic absorption of light. The logical extension is thus a pivot to an all-dielectric metasurface in which we may minimize the loss, and correspondingly, maximize the transmitted, useful light. As with Vest et al.'s experiment, we design a polarization state coupler, coupling horizontal and vertical polarization states together, as opposed to the usual beam splitter coupling spatial modes as in the original Hong-Ou-Mandel experiment [86, 85]. Correspondingly, we present here a design and experimental characterization for an all-dielectric metasurface which realizes a non-conservative coupler as required for such an experiment. In keeping with the experiment on bunching and anti-bunching of photons, we consider the coupling transformation between the $|H\rangle$ and $|V\rangle$ polarizations with a non-conservative transfer matrix [62] in the form:

$$\mathbf{T}_{\varphi} = \rho \begin{bmatrix} 1 & \mathrm{e}^{i\varphi} \\ \mathrm{e}^{i\varphi} & 1 \end{bmatrix}, \tag{3.8}$$

where ρ is a scaling coefficient. The phase value of $\varphi = \pi/2$ corresponds to a conventional conservative coupler, while other phases generally correspond to non-conservative transformations, notably, $\varphi = 0$ yielding the inverted bunching behaviour demonstrated by Vest et. al. The optimal practical realization with the minimal necessary amount of losses (in structures without gain) corresponds to the maximum possible value of ρ, which is achieved when the maximum singular value

[1]Fabrication was performed by Khosro Zangeneh Kamali using facilities at ANU's ANFF

of the transfer matrix $\sigma_1 \to 1$.

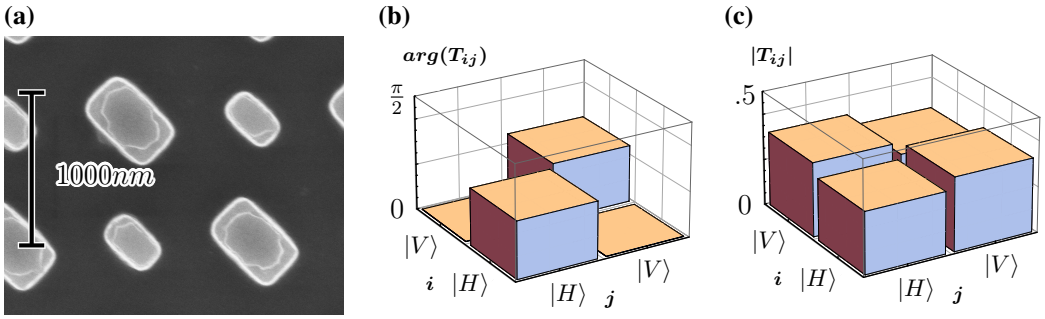

FIGURE 3.3: Fabricated complex-birefringent metasurface for arbitrary transformation of polarization-entangled two photon states. (a) SEM image of a metasurface made of amorphous-silicon on a glass substrate. (b, c) Experimentally characterized transfer matrix at a wavelength of 1560nm, including (c) arguments and (d) modulus of the elements, which is close to Eq. (3.8) with $\varphi = \pi/4$.

Using the same analytic and numerical approaches to complex birefringence as outlined in Section 2, binary metasurfaces implementing unconventional polarization coupling as per Eq. (3.8) for some arbitrary phases φ were designed. These designs were then fabricated and characterized classically, with an example of results presented in Fig. 3.3(a), which transfer matrix [Figs. 3.3(b, c)] realizes the case of $\varphi \simeq \pi/4$. The results hown have a normalized least mean squares parameter value of $3.5 \times 10{-}7$, with a maximum standard deviation in datapoints of $6.9 \times 10{-}7W$. While the absolute values of the experimental transfer matrix are not individually unitary as in Eq. (3.8), with a slight variation between the diagonal and antidiagonal values, the fabricated metasurface nevertheless enables unconventional interference and control of the biphoton states.

This demonstration of a transfer matrix in line with the inverted Hong-Ou-Mandel experiment potentially paves the way towards efficient quantum computing. Photonics are a prime candidate for the implementation of quantum computing, owing to their innately quantum behaviour and extreme propagation speed. This is a topic that has seen considerable interest over the past decade, and the metasurface demonstrated here, with its thoeretically optimal transmissivity, can only complement further exploration of the concept. While the HOM effect of bunching of photons may be utilized as the fundamental basis of bosonic qubit logic gates [87], so too can anti-bunching result in the potential for *fermionic* qubit logic gates [88], which may subsequently be used as the building blocks of a full optical computation circuit. Nor should a metasurface implementing the exact $\varphi = 0$ transfer matrix of Vest et al.'s experiments be impossible, only requiring a more carefully designed and fabricated metasurface. Unfortunately, a more detailed exploration

of this concept is well beyond the scope of this thesis, and may be left to a later work.

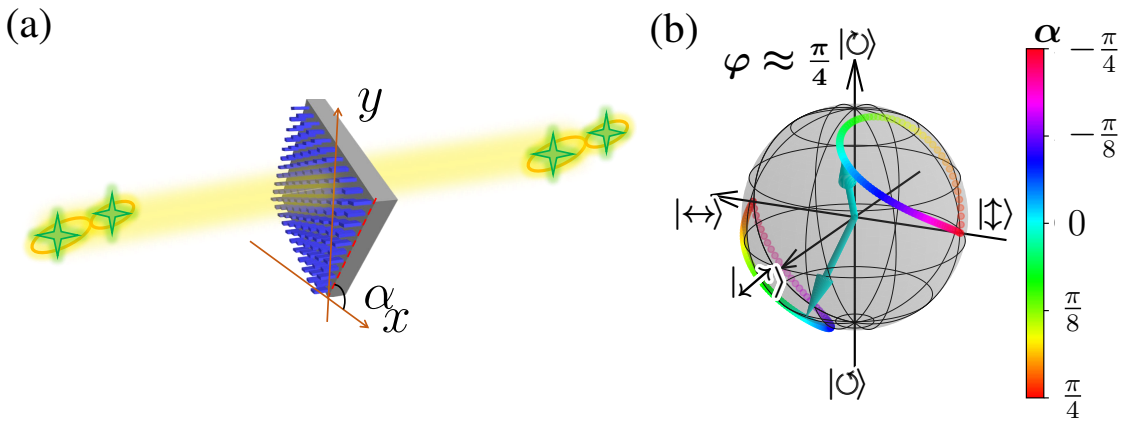

FIGURE 3.4: Application of complex-birefringent metasurfaces for arbitrary transformation of polarization-entangled two photon states. (a) Schematic of a metasurface oriented at an angle α° to perform the desired transformation for entangled photon pairs. (b) Transformation of $|\Psi(H,V)\rangle$ entangled input state calculated with the experimental transfer matrix of the metasurface oriented at angle α° as shown in (a).

This metasurface serves a dual purpose as a demonstration platform for demonstrating the capability of complex birefringence for control of entanglement of biphoton states. Utilizing the experimentally measured transfer matrix [Fig. 3.3(b, c)] of this metasurface, numerical calculations were performed to determine the transformation of a biphoton state. Similar to the equivalent calculations performed with a conventionally birefringent waveplate and shown in Fig. 3.2(a), an input biphoton state comprising orthogonally polarized horizontal and vertical states was projected through the metasurface, with the metasurface rotated at an angle α, given by $\mathbb{R}(-\alpha)\cdot\mathbf{T}\cdot\mathbb{R}(\alpha)$ where $\mathbf{T}$ is the transfer matrix. The output polarizations were again plotted on a Poincaré sphere, shown in Fig. 3.4(b), with the colours of the points representing the pairs of states at a given angle α. As we can see in the figure, the polarization states *converge* towards each other as the metasurface is rotated, despite starting with a pair of fully orthogonal states. This demonstrates that the metasurface is, indeed, capable of altering the degree of polarization of light, unlike a conventionally birefringent transformation.

Unfortunately, resources were not available to perform the verification of these experiments in the quantum regime, in particular, no quantum light source was available for use. However, these classical results remain largely sound as a demonstration of the key concepts involved.

One particular issue of note in the context of quantum experiments is that the fundamental mode of operation of complex birefringence depends on loss through

judiciously engineered diffraction. Unlike the case of classical light wherein the lost light may be entirely disregarded beyond efficiency concerns, loss of half of a pair of correlated photons must be accounted for in experiment. However, this is a relatively well-understood problem which has been discussed [89] and in some cases, exploited as a part of the experiment, such as in parity-time symmetry breaking experiments [90].

Even in the case of losses of quantum light, information need not be lost, and can be recovered in a systematic manner, via a technique called quantum state distillation. The general intention of this technique, as the name implies, is to distill some smaller set of states from a larger ensemble of states while preserving the maximal amount of quantum information possible [91]. In other words, this is a form of filtering of quantum states while not destroying information, with uses such as remote state preparation [92] and the purification of qubits for quantum computation [93]. More importantly, any filtering process may be considered a lossy process in which some quantity of the initial pool of prepared states is removed. As such, this both provides a formalism by which we may consider the loss of photons and accordingly quantify the information lost, and by considering the lost photons to be a form of random noise, a means by which they might be filtered out directly [94].

Procrustean filtering is a technique through which local filtering may be applied to a single photon out of a biphoton state to recover information about the total state [91]. Photon loss, as would be incurred using the non-conservative metasurfaces I have outlined in this thesis, may in fact be addressed by this filtering technique with the appropriate adjustments for what is functionally equivalent to bit-flip noise [94]. Even so, a key advantage of my approach, implemented as it is on dielectric metasurfaces, is that the loss is *controllable*. This is not the case in plasmonic metasurfaces, where the loss is a fundamental quality of the material used. Furthermore, the formalism suggested here presents an exact means to quantify the probability that any given input pair survives the filtering, or lossy transition process. A more detailed analysis may be done in a future work, however, it remains that despite the lossy nature of the complex birefringence proposed in this thesis, manipulation of quantum light in a concise and efficient way remains very much within the realms of possibility.

3.3 Summary

In this chapter, I have further developed the concept of complex birefringence, demonstrating that it can be used to implement novel types of polarization control. This includes the control over the degree of polarization entanglement in a monolithic structure, allowing, in theory, full control of the entanglement using a complex birefringent metasurface by employing judiciously engineered loss. The principles used to engineer this metasurface are identical to those of Chapter 2, demonstrating that the concept is both flexible and powerful while still managing to achieve an optimal structure and analytically minimal amount of loss, however,

while a metasurface capable of performing this transformation was fabricated and verified with classical characterization, a full experimental verification of this in a quantum experiment was not possible due to the limitations of time and access to resources.

The concept of complex birefringence was also utilized to demonstrate a metasurface that was capable of performing an unconventional Hong-Ou-Mandel experiment, with this metasurface implementing a highly unconventional polarization coupler with a phase difference of $\varphi = \pi/4$ capable of achieving full coalesence of photons on a dielectric structure which utilizes minimal amounts of loss, unlike previous works with inherently lossy plasmonic metasurfaces. Again, it was not possible to verify this in quantum experiment, however, verification of the metasurface via classical characterization was performed.

Chapter 4

Polarization monitoring

Polarization is a multiply parametric property of light, defined by independently measurable parameters that collectively comprise a property that is frequently considered a singular attribute. Correspondingly, to measure the polarization of light, it is usually necessary to take several sequential measurements which are then processed for reconstruction, a process that typically requires multiple optical components and independent measurements separated over time [95]. However, the distribution of the independent measurements across some span of time results in fundamental limits on the time resolution of any such measurement, and similarly, the introduction of multiple optical components naturally increases the physical bulk of any such system, as well as raising concerns of precision and accuracy for every component added.

In select cases, however, a full characterization of the polarization of light is not necessary to accomplish the desired experimental or practical goals. In such cases, a full reconstruction of the polarization necessarily introduces experimental and computational overhead to accomplish such reconstruction [96, 97, 98, 99], which may be undesirable. Additionally, such techniques often rely on the projection of the polarization state being measured to some known state, such as the horizontal or vertical, before being measured and reconstructed, which once again introduces more potential losses and errors. As such, a technique in which we directly monitor ultrasmall deviations from an initial polarization state in some manner can be desirable in experimental and practical usecases, allowing for rapid and immediate response.

In the last decade, metasurfaces comprised by a thin layer of nanostructures have shown exceptional capabilities in the manipulation of both classical [44] and quantum [100, 99] light associated with the polarization degree of freedom. Particularly, metasurfaces have been used for compact and fast polarization measurement in a static form by dividing the beam into multiple spatial paths [96, 97, 98, 99], and in fact, I will delve into this aspect of polarization in Chapter 5. However, these metasurface polarimeters still require computational data processing to reconstruct the polarization state, and the achievable resolution in differentiating adjacent polarization states is limited in turn by the precision of the detectors and computational algorithm. This presents difficulties when the desired perturbations are extremely small, and moreover, forces additional computational overhead

and processing time. Here, I propose instead a means of *directly* monitoring the perturbation of polarization states from a chosen anchor point, allowing for sensitive, minimal detection.

Direct polarization monitoring has many potential uses, even limiting ourselves to monitoring only the magnitude of the deviation as opposed to the exact deviation. Materials analysis and quality control in manufacturing, for example, frequently utilizes polarization to monitor for residual stresses and flaws in manufacture [101, 102]. Similarly, polarization microscopy of various forms has seen rising interest in biomedical sciences, in particular for various forms of cancer detection [103], sometimes with the aid of some fluroescent dye introduced to the tissues in question [104]. The principles in all of these usecases are similar: similar materials produce similar polarization changes in incident light, whether the materials are glass, plastic, or biological tissues, and as such, deviations from a known baseline is sufficient to establish a deviation in the material. While a full analysis of the polarization state in question can in some cases yield more information, it is *sufficient* to simply know that some degree of deviation exists, perhaps as a first-response sorting system, with unusual cases subsequently measured in greater detail.

Furthermore, following my development of the concept of complex birefringence in Chapters 2 and 3, one notable weakness still remains. The scheme as discussed, while principally speaking general, does not currently support the control of arbitrary elliptical (or circular) polarizations. This is due to the fact that the metasurfaces utilized lack chirality, however, this lack of chirality is *not* a fundamental limitation of complex bifringence. Rather, it is a limitation arising from the physical implementations as discussed, coupled with the fact that dielectric metasurfaces tend to offer weaker chiral responses than plasmonic metasurfaces, due to the lack of surface plasmon enhancement of the resonances [105, 106]. This deficiency will be addressed in this chapter, wherein I discuss the notion of introducing chirality to extend the concept of complex birefringence, developing both a use-case as well as a practical means of introducing chirality even in simple binary metasurface pixels as used here.

Such chiral, dielectric metasurfaces for polarization monitoring naturally carry the high transmissivity characteristic of dielectric metasurfaces. This remains a strong positive despite the relative weakness of chiral responses inherent to dielectric metasurfaces due to the high transmissivity, with the high transmissivity enabling sensitive detection for low-light measurements [44, 100, 99]. Furthermore, this demonstrates more general cases of polarization transformation utilizing the same basic principles of complex birefringence, greatly extending the flexibility of the concept.

4.1 Concept for polarization monitoring

To monitor deviations from a polarization state, we must first choose the state to be monitored, now designated the anchor state $|\psi_{anch}\rangle$. This is represented in Fig. 4.1 as a red cross on the surface of the Poincaré sphere. Any perturbations from this state are then represented as the orthogonal state $|\psi_{\perp}\rangle$, thus yielding the overall, perturbed input polarization state $|\psi_{in}\rangle = |\psi_{anch}\rangle + \delta|\psi_{\perp}\rangle$, where δ is small, and gives the magnitude of the perturbation. δ may also be complex, representing the phase of the perturbation, ϕ_{δ}. Represented in the shaded region in Fig. 4.1(a) are perturbations over the full 2π range of phases, for values of $|\delta|^2 < 0.01$. We note for completeness that by definition of orthogonality, $\langle\psi_{anch}|\psi_{\perp}\rangle = 0$. We construct the desired transformation mathematically as

$$\mathbf{T} = \xi \left(|V\rangle \langle \psi_{anch}| + \alpha |H\rangle \langle \psi_{\perp}| \right), \tag{4.1}$$

yielding an output state of

$$|\psi_{out}\rangle = \mathbf{T}|\psi_{in}\rangle = \xi(|V\rangle + \alpha\delta|H\rangle), \tag{4.2}$$

where $|\xi|^2$ gives the maximum transmission of power of the anchor state $|\psi_{anch}\rangle$, and $|\xi\alpha|^2$ gives the transmission of the perturbation state $|\psi_{\perp}\rangle$. In this ideal case, the anchor state is transformed purely to the vertical polarization state, albeit with some loss, and any perturbations from said anchor state are transformed into the horizontal polarization state. This yields an easily measurable value quantifying the magnitude of the perturbation $|\delta|$: the ratio of powers in the horizontal and vertical output states, or mathematically, $P_H/P_V = |\alpha|^2|\delta|^2$. This measurement can be trivially performed using, for example, only a polarizing beam splitter and two power meters, as shown in Fig. 4.1(b). Accordingly, the metasurface design goal would be to maximize $|\alpha|^2$, effectively amplifying the sensitivity of the metasurface to any small perturbations. We term this the *responsivity* of the design, represented by $\eta = |\alpha|^2$, and is seen in Fig. 4.1(c) as the greatly increased coverage of the shaded area around the vertical polarization. With this concept, we only require an initial characterization of the η of the metasurface, following which, the amplitude of any deviation of the input may be determined through a single measurement of the ratio P_H/P_V, and trivial calculation of $|\delta| = \sqrt{(P_H/P_V)/\eta}$.

Note that the ideal transformation in Eq. 4.1 is in general *non-unitary* (and thus nonconservative) and *chiral*, particularly for highly elliptical and circular anchor polarization states. In practice, chiral transformations with dielectric metasurfaces at normal incidence are non-trivial to attain [107], and working within this limitation, an additional term is added to Eq. 4.1 as follows:

$$\mathbf{T} = \xi \left(|V\rangle\langle\psi| + \alpha|H\rangle\langle\psi_{\perp}| + \gamma|V\rangle\langle\psi_{\perp}| \right). \tag{4.3}$$

This additional term in γ represents the degree of the perturbation that is mapped to the $|V\rangle$ polarization state instead of the horizontal, altering the ratio to $(P_H/P_V)/\eta = |\delta|^2/|1+\gamma\delta|^2$. This functionally introduces a degree of non-uniqueness

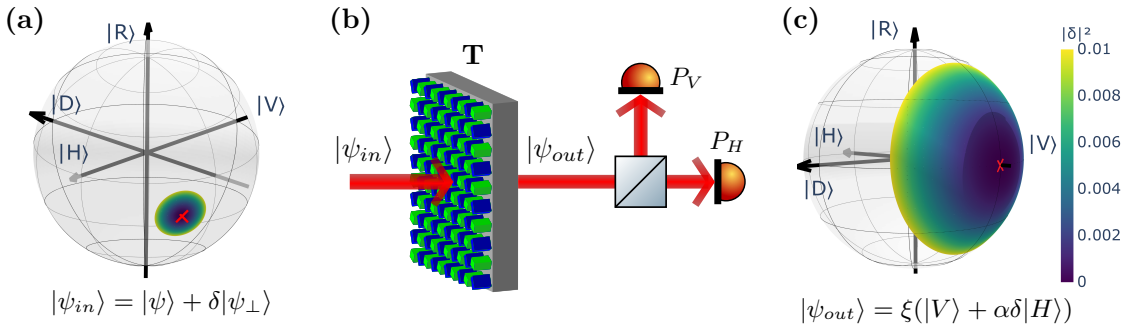

FIGURE 4.1: Concept of sensitive polarization monitoring with metasurface. (a) An arbitrarily chosen elliptical anchor polarization (red cross) on a Poincaré sphere and deviations $|\delta|^2$ up to 0.01 are indicated by a crown. (b) An experimental scheme utilizing metasurface performing a special non-unitary transformation $\mathbf{T}$ that transforms a perturbed input polarization $|\psi_{in}\rangle$ to an output polarization state $|\psi_{out}\rangle$, allowing for monitoring of polarization deviations using only a polarizing beam splitter and the power measurements P_V and P_H. (c) At the output, the anchor state is converted to the vertical polarization and the horizontal component represents the deviation which is amplified by a factor $\eta = |\alpha|^2$.

to the calculation of delta for a given power ratio as follows. Beginning with the ratio of powers, given simply as:

$$\frac{P_H}{P_V} = \frac{|\langle H|\mathbf{T}|\psi_{in}\rangle|^2}{|\langle V|\mathbf{T}|\psi_{in}\rangle|^2} = \frac{|\alpha\delta|^2}{|1+\gamma\delta|^2},$$

we assert that for some range of δ_{max} to δ_{min}

$$\frac{P_H}{P_V} = \frac{|\alpha\delta_{max}|^2}{(1+|\gamma|\,|\delta_{max}|)^2} = \frac{|\alpha\delta_{min}|^2}{(1-|\gamma|\,|\delta_{min}|)^2}, \tag{4.4}$$

and solve to reveal that

$$\begin{aligned} |\delta_{max}| &= \frac{\sqrt{P_H/P_V}}{|\alpha|+|\gamma|\sqrt{P_H/P_V}} \approx \sqrt{\frac{P_H/P_V}{\eta}}\left(1+|\gamma|\sqrt{\frac{P_H/P_V}{\eta}}\right) \\ |\delta_{min}| &= \frac{\sqrt{P_H/P_V}}{|\alpha|-|\gamma|\sqrt{P_H/P_V}} \approx \sqrt{\frac{P_H/P_V}{\eta}}\left(1+|\gamma|\sqrt{\frac{P_H/P_V}{\eta}}\right). \end{aligned} \tag{4.5}$$

Thus, for any measured power ratio P_H/P_V, the magnitude of perturbation is determined to be within the range $[\delta_{min}, \delta_{max}]$, which is in turn proporation to γ and the input perturbation. Accordingly, we introduce an additional design goal: to minimize the fraction of the perturbation power mapped to the vertical component at the output, parametrized by $|\gamma|^2$.

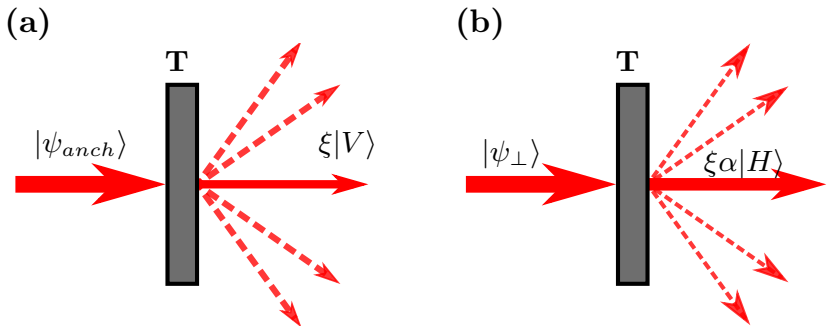

FIGURE 4.2: Schematic representation of optimal metasurface for monitoring of polarization deviations. (a, b) Response of metasurface to incident anchor polarization state $|\psi_{anch}\rangle$ and the perturbed state $|\psi_{\perp}\rangle$, respectively, with diffraction losses shown as dashed lines.

Utilizing Jones formalism, we may define the anchor state and its orthogonal as follows:

$$|\psi_{anch}\rangle = \begin{bmatrix} \cos\beta \\ \sin\beta e^{i\varphi} \end{bmatrix}, \quad |\psi_{\perp}\rangle = \begin{bmatrix} -\sin\beta e^{-i\varphi} \\ \cos\beta \end{bmatrix}, \tag{4.6}$$

we may rewrite Eq. 4.3 in explict parameters of the input polarization as:

$$\mathbf{T} = \xi \begin{bmatrix} -\alpha\sin\beta e^{i\varphi} & \alpha\cos\beta \\ \cos\beta - \gamma\sin\beta e^{i\varphi} & \sin\beta e^{-i\varphi} + \gamma\cos\beta \end{bmatrix}. \tag{4.7}$$

This yields an analytic expression for a transfer matrix that maps a chosen anchor state (β, φ) to the vertical output polarization with any perturbations mapped to the orthogonal horizontal output polarization with a sensitivity α. This is an asymmetrical transfer matrix with non-equal off-diagonal components, which will be an important consideration in the subsequent design process.

4.2 Designining metasurfaces for polarization monitoring

As discussed in Section. 2, the required non-unitary transfer matrix $\mathbf{T}$ may be achieved in a monolithic, dielectric metasurface. In Figure 4.2, we can see the desired transformation as physically implemented using tailored diffractive losses: the metasurface transforms the anchor state $|\psi_{anch}\rangle$ into $|V\rangle$ in the zeroth order with a tailored reduction of power, where the attenuation is lost to high-order diffraction, as shown in Fig. 4.2(b). Input perturbations $|\psi_{\perp}\rangle$, orthogonal to the anchor state, are correspondingly the metasurface transformed into $|H\rangle$ in the zero order with (ideally) full transmission, since we aim to minimize the high-order diffraction for such states as shown in Fig. 4.2(c).

However, as already noted, the ideal form of the transformation, where $\gamma = 0$, requires in generality a chiral transformation, in contrast to the already-performed work on complex birefringence, which focuses purely on the symmetric case. We

therefore impose an additional constraint to equation 4.7, which yields by construction of equal off-diagonal terms the analytical condition:

$$\gamma = -cot\beta e^{-i\varphi}(\alpha - 1) \tag{4.8}$$

to arrive at a modified transfer matrix of

$$\mathbf{T}_{symm} = \begin{bmatrix} -\sin\beta e^{i\varphi} & \cos\beta \\ \cos\beta & \frac{1-\alpha\cos^2\beta}{\sin\beta} e^{-i\varphi} \end{bmatrix}. \tag{4.9}$$

Neglected for clarity is a scaling factor of $1/\sigma_1$, scaling the transfer matrix by its maximum SVD value so as to ensure unity. This is an analytical optimal solution, minimizing the necessary uncertainty of reconstruction γ for a given responsivity α and chosen anchor state. It was observed that this constraint of chirality to the transformation resulted in substantial loss of potential performance, the specifics of which will be discusssed quantitatively in the experimental results. The chosen platform of binary metasurfaces presented a potential solution in the form of near-field coupling between nano-pillars and the inherent asymmetry of the substrate, presenting a means by which chirality can be implemented.

Unlike the linear addition of uncoupled pixels, near-field coupled chiral structures are not readily analyzed with analytical methods, and as such, it was necessary to design the metasurfaces using inverse design. Inverse design is a process in which metasurface parameters are designated, and the numerical modelling is utilized to generate and trial potential metasurfaces until the desired performance is achieved [39, 40]. As discussed in Chapter 1, metasurface optimization is a highly multivariate problem, in this case, utilizing 6 parameters: lengths, widths, and angles of rotation for each cuboidal metasurface pixel, with heights and supercell dimensions fixed. Furthermore, this is a multiobjective optimization problem with the γ and overall transmission as minimization and minimization targets respectively, and with the responsivity α a direct constraint on the optimization problem. As such, this optimization problem cannot be easily approached with a simple gradient descent: not only are gradient descent algorithms prone to optimizing towards local minima in multivariate problems, such algorithms also handle multi-objective problems poorly. An approach of writing a function with which to combine the objectives tends to lead to biasing towards one target over another, and while multi-objective variants of the gradient descent algorithm exist, they tend to have poor overall performances [108].

As such, this optimization task was performed using the NSGA-II genetic algorithm as implemented in a Python package [108, 109], interfacing with the RCWA code as the numerical solver. This genetic algorithm was chosen due to its robust handling of multiple objectives, as well as its high performance in constrained optimization problems, exactly as was required for this design process. This attained a highly efficient metasurface that was capable of implementing the desired polarization monitoring for fixed anchor polarization state and responsivities.

Following this inverse design process, an optimization pass was performed using CST Studio, similar to the process described in section 2.3, and fabricated using the same techniques.

4.3 Experimental demonstration for polarization monitoring

After fabrication, the metasurfaces were characterized, in the zeroth order transmission using a free space setup. Unlike in Chapter 2, a quarter waveplate and halfwaveplate were used to project the states into the bases, allowing for fully condition reconstruction of asymmetrical transfer matrices. Owing to the higher specificity of design of this particular application, scans were performed over a range of wavelengths as well as physical rotation angles θ of the metasurface (indicated in Fig. 4.3(a)), searching for the best-fit design.

Figure 4.3(b-f) shows experimental results of fabricated metasurfaces[1]. Figure 4.3(b) shows the characterized Jones matrix of the metasurface at $1573.8nm$ when the rotation angle is $\theta = 64°$. As before, the characterization was performed using the tomography method laid out in Section 2.4, launching prepared polarization states through the metasurface which are subsequently projected into basis states for measurement with a power meter, and fitted using nLMS as the target fitting parameter. This fitting parameter was found to be 4.3×10^{-6}. As per the inversely-designed structure, the characterized transfer matrix turned out to be highly chiral. The corresponding anchor state was determined from this characterization to be $[\cos(0.353\pi), \sin(0.353\pi)\exp(-0.388\pi i)]^T$, using an extension of Eq. 4.3 as:

$$|\psi_{anch}\rangle = \frac{\mathbf{T}^{-1}|V\rangle}{||\mathbf{T}^{-1}|V\rangle||}.$$

Similarly, $|\gamma|$ and α were determined from the transfer matrix using:

$$|\gamma| = \frac{|\langle V|\mathbf{T}|\psi_{\perp}\rangle|}{|\langle V|\mathbf{T}|\psi_{anch}\rangle|} \tag{4.10}$$

$$\eta = |\alpha|^2 = \frac{|\langle H|\mathbf{T}|\psi_{\perp}\rangle|^2}{|\langle V|\mathbf{T}|\psi_{anch}\rangle|^2}. \tag{4.11}$$

This state is a highly elliptical state, indicated for visualization by the red cross on the Poincaré sphere in Fig. 4.3(b), which shows the anchor states as a function of the metasurface rotation angle in the range from $-90°$ to $90°$.

Notably, this concept lends itself well to rotational tuning —one can use a single metasurface to monitor a large range of different anchor states. As we see in

[1]Fabrication was performed by Jihua Zhang using facilities at ANU's ANFF

Fig. 4.3(c), a simple physical rotation of the metasurface results in a strong variation of the anchor state transformed to the vertical output, correspondingly, the responsivity varies over a large range as we can see in Fig. 4.3(e), up to a maximum of approximately 25. Despite this not being an explicit design goal, it is clear that for a large range of anchor states, we are nevertheless able to maintain a strong responsivity, with values > 5 being considered usable to perform measurements. Furthermore, it is worth noting that this range may be effectively doubled simply by considering the mapping of the anchor state to the horizontal, with the perturbation correspondingly mapped to the vertical polarization state. Unsurprisingly, this results in a mirroring of the results, with an optimal symmetrical transfer matrix of:

$$\mathbf{T}_{symm} = \begin{bmatrix} \frac{1-\alpha \sin^2 \beta}{\cos \beta} e^{-i\varphi} & \sin \beta \\ \sin \beta & -\cos \beta e^{i\varphi} \end{bmatrix}, \tag{4.12}$$

with a corresponding $\gamma = \tan \beta e^{-i\varphi}(\alpha - 1)$. Accordingly, we see that it is possible to map the anchor state to the horizontal and vertical output states when the $0 > \beta > \pi/4$ and $\pi/4 > \beta > \pi/2$ respectively, to minimize γ, which has a minimum theoretical value of

$$|\gamma| = min(tan\beta, cot\beta) \cdot (\alpha - 1)$$

for all symmetrical transfer matrices. While this is not shown in Fig. 4.3, it is clear that this approximately doubles the range of anchor states with effective responsivities, while requiring essentially only an implementation modification of swapping the positions of the vertical and the horizontal outputs in the results.

In Fig. 4.3(d), we see both the demonstration of sensitive monitoring of polarization deviations, as well as the effect of γ on the measurement. This is an analytical calculation derived from the experimental characterization of the transfer matrix, plotting the power ratio P_H/P_V against the perturbation size $|\delta|^2$. It is, as noted, all but trivial to find the size of the perturbation simply from the gradient of the line, shown in red, simply by dividing the power ratio by η, however, we see that as the phase ϕ_δ of the perturbation varies, a small range of $|\delta|^2$ appears for any given measured power ratio, shown in the shaded colour of the figure. As discussed, this uncertainty of determination of $|\delta|^2$ is dependent on γ, and is on the order of $2|\gamma\delta|$, proportional to the magnitude of the deviation. It remains reasonable, therefore, to conclude that for small deviations, we can still obtain accurate and useful reconstruction. The responsivity as a function of the rotation angle is shown in Fig. 4.3(e). One can see that the responsivity is maximized near the rotation angle we have chosen, as indicated by the vertical dashed line. The $|\gamma|$ value also reaches the smallest value of 0.646 near this angle, as shown by the solid line in Fig. 4.3(f). This corresponds to a relative uncertainty of $1.292|\delta|$, or about 12.9% when the deviation magnitude is 10% of the input anchor state.

The experimental characterization of the metasurface indicates a superior (smaller) γ than the ideal, symmetrical case, as predicted by the differences between Eq. 4.9 and 4.1. In Fig. 4.3(f), we see that the supported $|\gamma|$ by a symmetrical

(i.e. non-chiral) transfer matrix for the same anchor state and responsivity is larger than our experimental values. This is not entirely a surprise, given that the characterized transfer matrix as seen in Fig. 4.3(b) is *asymmetrical*, and thus, the metasurface deviates from the design in a particularly serendipitous manner. This chirality arises from the near-field coupling between adjacent pixels as well as asymmetry in the propagation direction arising from the substrate, which is not well-accounted for by the theoretical binary metasurface structure as shown in Eq. 2.6.

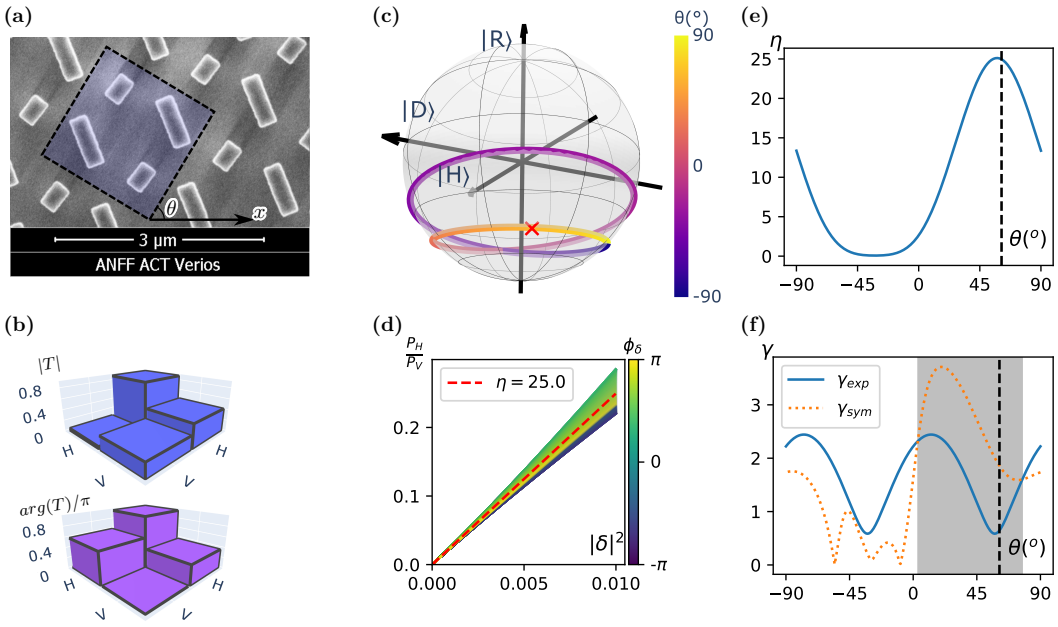

FIGURE 4.3: (a) SEM of metasurface fabricated to implement polarization sensing. The unit cell is indicated using the black, dashed box, with rotation from the horizontal indicated by θ. (b) Experimentally characterized transfer matrix values of the metasurface when $\theta = 51°$. (c) Precession of the anchor state as a function of the metasurface rotation angle θ. The anchor state relating to the transfer matrix of (b) is indicated by the red cross. (d) Predicted power ratios P_H/P_V against deviation from anchor state $|\delta|^2$. The phase of the deviation ϕ_δ, indicated by the colour gradient, results in a relative uncertainty range $2|\gamma\delta|$ in determining $|\delta|$. (e) Variation of responsivity as the metasurface is rotated by angle θ. The result corresponding to (b, d) is indicated by the dashed line. (f) Variation of uncertainty γ_{exp} with rotation of the metasurface, compared to a theoretically constructed metasurface with identical anchor state and responsivity, but of purely symmetrical transfer matrix (γ_{sym}).

This enhanced sensitivity was then directly measured. Using the experimental setup as shown schematically in 4.1, polarization states were prepared and projected through the metasurface, and then divided using a polarizing beam splitter into its horizontal and vertical components. The input states were prepared as before using

linearly polarized laser light in the infrared range ($1500 - 1575nm$) and focused onto a spotsize of approximately $40\mu m$ on the metasurface. Subsequently, lenses were used to collect the light and project it through the polarizing beam splitter, with the outputs measured using two power meters and recorded via a Python program.

At the optimized rotation angle $\theta = 64°$, a large number of perturbed states around the anchor state of $[\cos(0.353\pi), \sin(0.353\pi)\exp(-i0.388\pi)]^T$ were prepared. These states were prepared with the intention of covering a full phase sweep of $\phi_\delta \in (0, \pi)$, as well as deviations with magnitudes of up to $|\delta| = 0.1$. These perturbed states may be seen in polarization ellipse form in Fig. 4.5(a), with the black line showing the anchor state and the shaded blue region representing all perturbed states. For each input state, the output power ratio was measured multiple times and averaged before plotting at their corresponding position on the Poincaré sphere in Fig. 4.5(b). In line with the analytical design, we see that the H-V power ratio is minimized at the anchor state and increases proportionally with the deviation magnitude. From this measurement data, we obtain by fitting a responsivity $\eta = 21.8$, as shown in Fig. 4.5(c) by the red line. As before, the colour of the data points represents the phase of the input deviation ϕ_δ. Based on the maximum and minimum values of $|\delta|$ (i.e. the uncertainty of measuring $|\delta|$) for a certain H-V power ratio, we derive out the experimental $|\gamma|$ to be 1.33. Although it is larger than the predicted value from the characterized transfer matrix ($|\gamma| = 0.646$), it is still smaller than the theoretical limit ($|\gamma|_{sym} = 1.826$) predicted for a *symmetrical* transfer matrix as given in Fig. 4.3(f), confirming the advantage of chiral response applied in this work.

The demonstrated responsivity of $\eta = 21.8$ is slightly smaller than the predicted value from the characterized transfer matrix in Fig. 4.3. This is, most likely, due to experimental error inherent to the direct measurement of the power ratio. Due to the extreme sensitivity of this measurement, with its intention of measuring very small perturbations, the movement of the waveplates is on the order of 0.05°, on the same order as the 0.03° backlash error of the motors [110]. Furthermore, the physical rotation of the waveplates causes the beam to shift across the metasurface and power meter surface due to imperfect alignment; while pains were taken to account for this, limitations exist in the degree of precision that may be achieved without specialized equipment. This shift across the metasurface is likely to present problems; due to the uncorrected proximity effect during the electron beam lithography, it is likely that the dimensions of the nanopillars is not exactly the same across the entire patterned area. Given that the polarization transformation is based on these physical sizes, the transfer matrix varies to a slight degree across the metasurface. Thus, to ensure that a uniform transfer matrix is measured, a small beam size is necessary, however, as a beam is focused, it gains an increasing spatial frequency range and a degree of inherent polarization variation due to the beam divergence [111]. Cumulatively, these errors account for the difference in responsivity.

Lastly, we further demonstrated the proposed concept for an anchor state close to the right circular polarization by rotating the same metasurface at a different angle $\theta = -64°$ and operating it at a different wavelength of $1550.5nm$.

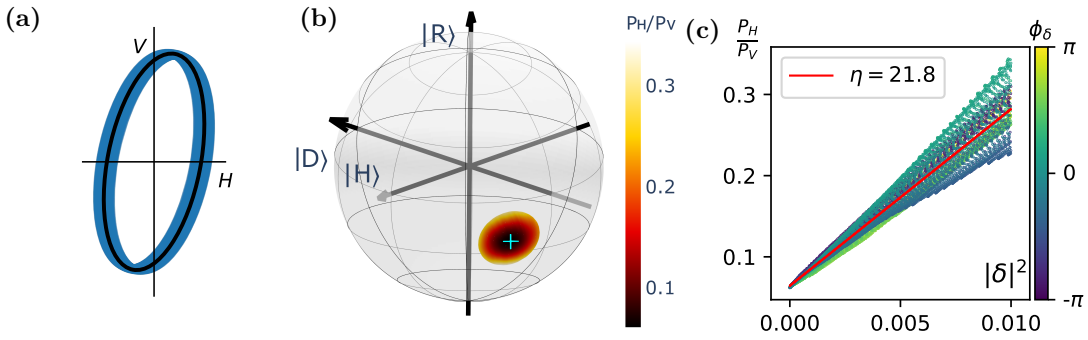

FIGURE 4.4: Experimental measurement of power ratios for an elliptical anchor state of $[\cos(0.353\pi), \sin(0.353\pi)\exp(-i0.388\pi)]^T$. (a) The polarization ellipse of the input polarization states used for the measurement. The precise anchor state is indicated by the black line, with variations from this state indicated by the blue, shaded region. (b) Experimentally measured power ratio outputs (P_H/P_V), plotted on a Poincaré sphere with positions corresponding to the corresponding input polarization states. The colour shading indicates the variation of power as the state deviates from the anchor state, indicated by the cyan marker, with the strong increase demonstrating that relative ease of measurement of small deviations. (c) The experimental power ratios as plotted against the deviations from the anchor states. The experimentally measured $|\gamma|$ is 1.33, as compared to the prediction from the experimentally characterized transfer matrix of 0.65.

The related result is shown in Fig. 4.5. The anchor state has a Jones vector $[\cos(0.21\pi), \sin(0.21\pi)\exp(-0.448\pi i)]^T$, whose polarization ellipse is indicated by the black line in Fig. 4.5(a) and position on Poincaré sphere is marked by the cyan cross in Fig. 4.5(b). For this anchor state, we experimentally demonstrated a responsivity of $\eta = 3.8$. Note that it is more difficult to achieve a high responsivity for a circular anchor state as compared to an elliptical anchor state as a result of the more stringent requirement on the chirality of the transformation in Eq. (4.1). For this near-circular anchor state, the experimentally measured $|\gamma|$ is 0.815. For a symmetrical transfer matrix, the theoretical $|\gamma|$ is 1.224 for the same anchor state and responsivity.

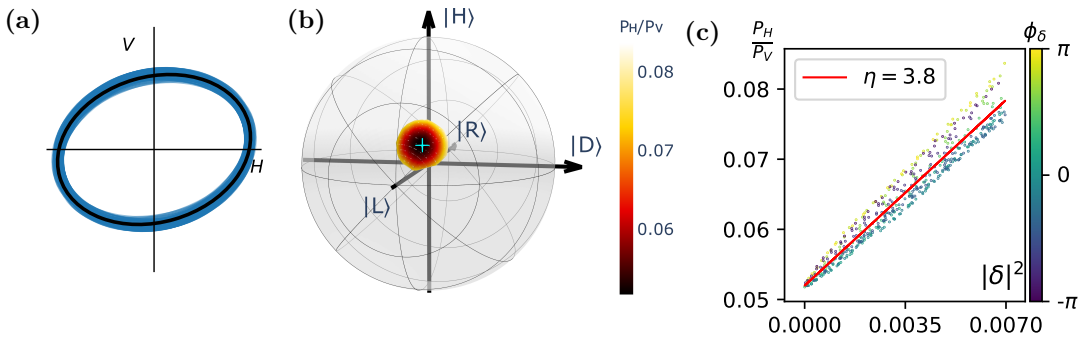

FIGURE 4.5: Experimental measurement of power ratios for a near-circular anchor state of $[\cos(0.21\pi), \sin(0.21\pi)\exp(-i0.448\pi)]^T$. (a) The input polarization states used for the measurement. The precise anchor state is indicated by the black line, with variations from this state indicated by the blue, shaded region. (b) Experimentally measured output power ratios (P_H/P_V), plotted on a Poincaré sphere with positions corresponding to the corresponding input polarization states. The colour shading indicates the variation of power as the state deviates from the anchor state, indicated by the cyan marker, with the strong increase demonstrating that relative ease of measurement of small deviations. (c) The experimental power ratios as plotted against the deviations from the anchor states. The experimentally measured $|\gamma|$ is 0.815, as compared to the prediction from the experimentally characterized transfer matrix of 0.500.

4.4 Chirality in dielectric metasurfaces

It is known that dielectric metasurfaces do not generally exhibit particularly strong chirality [50], however, the metasurface in this chapter, fabricated as silicon on glass, demonstrates a non-trivial degree of chirality. While in principle, any metasurface that exhibits some form of structural symmetry breaking is capable of causing a chiral transformation in projected light, these are typically weaker in dielectric metasurfaces as opposed to plasmonic metasurfaces, due to dielectric metastructures achieving on average lower local field enhancement than their plasmonic counterparts, outside of sharp resonances. This discrepancy can in cases

be as much to 20:1, leading to corresponding discrepancies in degrees of chiral response [112, 113].

Chirality is a relatively broad concept, even in the context of optical experiments alone. The fundamental physical concept of chirality revolves around physical asymmetry; an object is said to be chiral if in some way its mirror image cannot be superimposed on itself. In optical effects, chirality in general refers to the physical reversal of the direction of propagation of light through some part of the optical circuit, and that the behaviour in these inverted directions of propagation are not the same. Even within this relatively narrow definition, however, there are variations in types of chirality.

In an optical context, chirality revolves primarily around polarized light. There is no difference between flipping the polarization of incident light as opposed to inverting the optical component in question, therefore, by simple physical symmetry, the correlation between the handedness of polarization and physical inversion leads to what are termed chiral phenomena. As mentioned, chirality is a relatively broad term, and includes asymmetric circular polarization conversion, polarization rotation, and dichroism in various forms, whether linear or circular [114]. Furthermore, chirality can be observed in both reflected and transmitted modes. The latter will be the focus of this section.

The various forms of chirality each have their own uses, for example, dichroism of any kind can be used to implement polarization-sensitive filtering or wave mixing at an interface. In the specific case of this thesis, however, the chirality requirement arises from the numerical optimization problem, as a consequence of the transformation as described in Equation 4.1.

Chiral metasurface design is a highly non-trivial challenge, and yet one that has been sought after for a considerable amount of time. Even before the advent of metasurfaces in their current form, Fresnel had already speculated, two centuries ago, that helical structures can interact with similarly helical light (the latter of which we now term circular polarization) [115], attempts have been made to fabricate these structures, and inevitably fallen short of simpler structures more specifically designed with breaking of mirror symmetries in mind [107]. However, as yet no analytical description of chiral metasurfaces exist, and experiments in this matter depend largely on numerical optimization and physical testing. Such implementations of chiral metasurfaces may generally be classified into two categories, determined by the physical implementation of symmetry breaking: extrinsic and intrinsic chirality.

Extrinsic chirality, here, refers to some form of asymmetry induced via means external to the metasurface structure, typically by utilizing oblique incident angles. A schematic example is shown in Fig. 4.6(a). By angling the beam away from normal incidence, the profile presented towards the beam becomes asymmetric, thus yielding the required broken symmetry for a chiral response [116, 117]. Works on

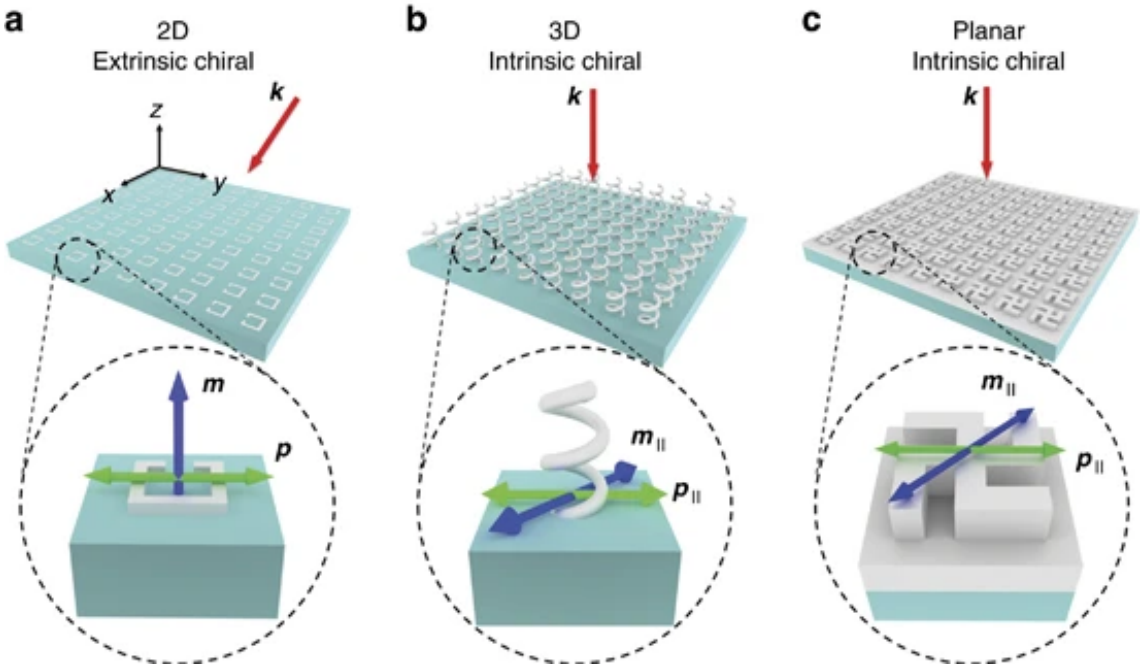

FIGURE 4.6: Schematic illustrations of types chiral metasurfaces, adapted from [107]. The red arrows $\boldsymbol{k}$ show the incident light, while the insets show single unit cells with their associated electric and magnetic fields ($\boldsymbol{p}$, green arrow and $\boldsymbol{m}$, blue arrow respectively). (a) shows an extrinsically chiral metasurface with split ring resonators. Note the oblique angle of incidence use to induce extrinsic chirality. (b) Optically thick metasurface with tall helical structures inducing intrinsic chirality. (c) Planar metasurface with gammadion structures inducing intrinsic chirality.

this matter have typically involved structures such as split-ring resonators utilizing plasmonic metasurfaces, with the associated losses [107, 118].

Intrinsic chirality, by contrast, refers to some form of structural asymmetry or chirality inherent to the metasurface even at normal incidence. One example of such structural asymmetry that has seen recent research efforts is the gammadion in both dielectric and plasmonic metasurfaces [107, 119, 120]. Similarly, three-dimensional spirals with their axis oriented normal to the direction of propagation of light offer structural asymmetry that leads to optical chirality [121, 122, 123]. These structures are optically thick, extending some significant fraction of a wavelength above the substrate, and consequently are challenging to fabricate, typically requiring multiple layers of deposition and etching. Schematic examples are shown in Fig. 4.6(b, c).

In general, the chirality of the metasurface pixel may be approximately predicted by its physical symmetry, with the according forms of classification, in turn leading to a ready form of prediction of the chirality supported by any given structure.

Considering, in general, that the standard 2×2 Jones transfer matrix is defined by:

$$\begin{bmatrix} t_x \\ t_y \end{bmatrix} = \begin{bmatrix} A & B \\ C & D \end{bmatrix} \cdot \begin{bmatrix} i_x \\ i_y \end{bmatrix}, \tag{4.13}$$

where t_x, t_y and i_x, i_y are the complex transmitted and incident electric fields in the x and y direction respectively, which in the backward propagation direction would yield a transfer matrix of:

$$\begin{bmatrix} t_x \\ t_y \end{bmatrix} = \begin{bmatrix} A & -C \\ -B & D \end{bmatrix} \cdot \begin{bmatrix} i_x \\ i_y \end{bmatrix}, \tag{4.14}$$

using the same notation for the incident and transmitted fields, and accordingly, we see that the symmetry of the transfer matrix infers the chirality of the relevant metasurface. In turn, the form of the transfer matrix may be predicted from the physical symmetry of the metasurface unit cell, with the physical symmetry giving the expected symmetry of the transfer matrix [51].

The chirality exhibited by the metasurface demonstrated in this chapter may be classified with its $C_{2,z}$ symmetry, categorized similarly to an L-shaped structure. As we can see in Fig. 4.3, the achieved transfer matrix is, indeed, highly chiral, with one linear, and one elliptical eigen state. However, this coupling-mediated asymmetry was not analytically studied in this thesis, and was arrived at through the optimization process. Nor is the concept of coupling-mediated transfer matrix a topic well studied as yet, with some few works largely utilizing plasmonic structures [124, 125], however, the singular demonstration of chirality in this work is a promising avenue of research, both for the general implementation of chiral transformations with dielectric metasurfaces, as well as to improve the performance of this specific concept of monitoring small polarization deviations.

4.5 Tunable metasurfaces for polarization monitoring

A notable weakness of the technique as outlined in this chapter is that the anchor state is fixed by the physical parameters of the metasurface, up to the rotation degree of freedom. Rotational tuning of the metasurface, while allowing for the variation of the anchor state, has limitations, as can see in Fig. 4.3; both sensitivity and the uncertainty scaling parameter γ worsen as the angle diverges from the optimal position (respectively decreasing and increasing). While the metasurface remains usable within a range of angles near this optimal angle, with the degree of usability defined by the tolerance of the external systems attached it is a fundamental and unavoidable tradeoff that must be paid to attain this tunability.

There exists, however, an alternative that was not explored in the course of this thesis. Tunable metasurfaces have seen recent interest, utilizing optically,

electrically, mechanically, or thermally actuated layers or media to alter the properties of the metasurface. In general, the concepts for tunable metasurfaces revolve around altering the physical parameters of the metasurface in some way, with a large number of ways in which this is approached. Mechanical tuning, for example, involves fabricating the metasurface on some form of stretchable substrate, allowing for mechanical stretching or squashing to alter the distance between metasurface pixels. Graphene layers have also been proposed as one of the most versatile approaches; via electrical tuning, it is possible to directly alter the resonance properties of the metasurface pixels and thus tune the properties over a broad spectral range. Similarly, the infiltration of birefringent liquid crystals allows for the tuning of the inter-pixel dielectric properties, allowing for the direct alteration of both the refractive index of the surrounding media as well as the electromagnetic resonances of the pixels themselves via electrical or thermal tuning [126, 127, 128, 129].

Combining the principles of these tunable metasurfaces with the polarization sensing metasurfaces demonstrated here would allow for the tuning of the metasurface properties. Even a relatively simple addition of liquid crystals, would allow for substantial freedom in enhancing the flexibility that this platform can enable. By introducing liquid crystals as a dynamically birefringent layer, electrical or thermal actuation would allow for the dynamic switching of said crystals from an unordered, isotropic state to a nematic, birefringent state, with the corresponding alteration of the optical properties will in turn alter the transformation of the binary metasurface, potentially paving the way towards a polarization sensing metasurface that is able to substantially vary its anchor state without losing sensitivity or increasing the uncertainty. This is, however, not analytically predictable, and is best treated using numerical simulations as well as practical experimentation in a future work.

4.6 Summary

In conclusion, we reveal that dielectric metasurfaces can provide amplified responsivity for monitoring small deviations around an arbitrarily chosen anchor polarization state through a simple readout of output horizontal and vertical components. We formulated a metasurface design principle and fabricate metasurfaces with a specially optimized binary combination of nano-resonators that is capable of transforming an arbitrarily chosen anchor state to a similarly arbitrary linear polarization state, where any perturbations are transformed into the orthogonal state with near-unity transmission. As such, any small deviations from the anchor states are covnerted into an effectively amplified deviation, in a convenient form that may be trivially measured as the ratio of the powers between linear polarization pairs. This may be accomplished, for example, using a single polarizing beam splitter and two power meters, providing a robust and simple system with which to monitor polarization perturbations without the use of a polarimeter or more involved computational processing.

This metasurface was demonstrated with both characterized results as well as direct, experimental measurements of perturbed polarization states. The measured results demonstrate high responsivity and precision in monitoring deviations around arbitrarily elliptical and near-circular input states, and proves that the concept may be extended freely to any chosen input state with the appropriate metasurface design. We anticipate that our work will enable a new class of ultra-compact and ultra-sensitive flat meta-optical devices for a broad range of applications, including advanced sensing, imaging (biomedical and otherwise), and metrology in both classical and quantum photonics.

This work has also demonstrated moderately strong chirality in a dielectric metasurfaces without utilizing extrinsic asymmetry. Numerical simulations as well as the experimental characterization and results verify that the fabricated metasurfaces display chiral effects that arise through exclusively through near-field coupling of symmetric metasurface pixels. This form of chirality presents a promising avenue for future exploration, potentially yielding a more general implementation of chiral, dielectric metasurfaces with simple design processes.

Chapter 5

Robust polarization measurements

As discussed in Section 4, polarization is a multiply parametric property of light, requiring several independent measurements to properly characterize [95]. Typically, this is performed using an instrument called a polarimeter, which applies through mechanical reconfiguring some known degree of phase shift to the input polarization, projects the unknown polarization state to be measured into multiple different basis states, typically the four Stokes parameters, which are in turn used to reconstruct the original polarization state. The phase shift is accomplished using some form of tunable phase retarder, such as a waveplate that may be rotated relative to the beam, and by utilizing sequential reconfigurations of this system, a full basis of reconstruction may be generated for the measurement.

Here, I develop a novel form of polarimetry by applying concepts from quantum physics, demonstrating a method of performing polarimetry in a single step that not only avoids the problems of traditional polarization measurements but also circumvents the problems faced by contemporary attempts at accomplishing such polarimetry, and further incorporates design measures to ensure that the resultant metasurfaces are highly robust against fabrication error while being able to offer accurate and precise measurements.

Polarimetry in experimental scenarios presents numerous experimental challenges, namely, the common refrain of the bulk of traditional optical components and the mechanical imprecision of adjusting such components. Any system is only as precise as the tolerances allowed by the system, which in the case of mechanical, reconfigured parts, presents challenges in particular for the precision required in quantum measurements. In the case of polarimetry, an additional challenge of requiring that the polarization state be projected to *multiple* basis states presents a unique problem of limiting the temporal resolution of any such measurement; a measurement simply cannot be taken any faster than the phase retarder can be mechanically reconfigured. These limitations constitute systematic, mechanical errors that are especially problematic for quantum experiments.

These problems are well understood and recognised, especially in the particular case of quantum light. Consequently, efforts towards eliminating the systematic errors arising from these mechanical reconfiguration have seen much interest, revolving as they do around the obvious path of eliminating the mechanical

components entirely, and perform the experiment entirely via a static device of some kind [130]. The key concept to this approach involves the use of a series of beam-splitting optical components in some manner, each implementing quantum interference [131, 132]. This thus results in multiple, spatial output ports, each one with its own detector, with a number of outputs greater than the number of inputs to the system. These extra inputs correspond, naturally to vacuum input states, incorporating nonclassical multiphoton interference as an unwanted but inevitable factor to the measurement. Metasurfaces, however, present a route to circumvent these problems entirely.

Recent works reveal that metasurfaces are capable of resolving incident, polarized light into multiple basis states over spatial degrees of freedom as opposed to temporal [96, 97, 98, 99]. The metasurfaces are tailored to diffract chosen polarization components of incident light to each diffraction order, thus dividing the input state into multiple spatial ones, forming a complete set of bases for accurately and uniquely reconstructing the polarization state using simultaneous measurements. This technique facilitates measurement of both classical [44] and quantum states [100, 99].

However, current approaches [133] still exhibit undesirable limitations. While these limitations were previously believed to be intrinsic to this approach, I have demonstrated over the course of my thesis that this is not the case. The first, and primary restriction to prior approaches lies in the design of the metasurface; until now, it has been believed that it is fundamentally necessary to interleave multiple metagratings on a metasurface in order to split several distinct pairs of polarization components. This interleaving imposes restrictions on the utility of such a metasurface: not only must the incident beam be large enough to fully illuminate *all* the interleaved gratings, said interleaving also results in distortion of the beam transverse to the direction of propagation [134, 99]. Neither of these are practical, especially in the context of the strict requirements of quantum experiments.

A recent study has demonstrated polarimetry with a single metagrating [133], however, an additional linear polarizer is still required under this scheme. This naturally adds setup complexity and size in addition to attenuating the transmitted power, and thus, remains less than ideal for applications of the concept. However, these limitations are not inherent to single-shot polarimetry, and in my thesis, I explored a new path towards practical, usable implementations.

Existing works on single-shot polarimetry attempt to recreate traditional polarimetry, resolving the incident polarization into some combination of the traditional orthogonal Stokes basis states (horizontal, vertical, diagonal, anti-diagonal, left circular and right-circular), which are then used to reconstruct the unknown polarization state; the novelty being that the the resolution is performed over spatial degrees of freedom, typically diffraction orders of the metasurface. However, this requires that *every* relevant diffraction order needs to act as a (close to)

perfect polarizer, which is a largely impractical goal to accomplish in practical implementations, leading to the afore-mentioned interleaving of metagratings and the associated problems. However, drawing from the concept of Positive Operator-Valued Measurements (POVM) formalism from quantum mechanics, I established that a regime exists in which using *partially* polarizing basis states we may accomplish a full reconstruction of the Stokes parameters defining the state. This eliminates both the need to attain an extremely precise design and fabrication, and to interleave multiple metagratings. As such, this is a far more practical and easier to attain single-shot polarimetry.

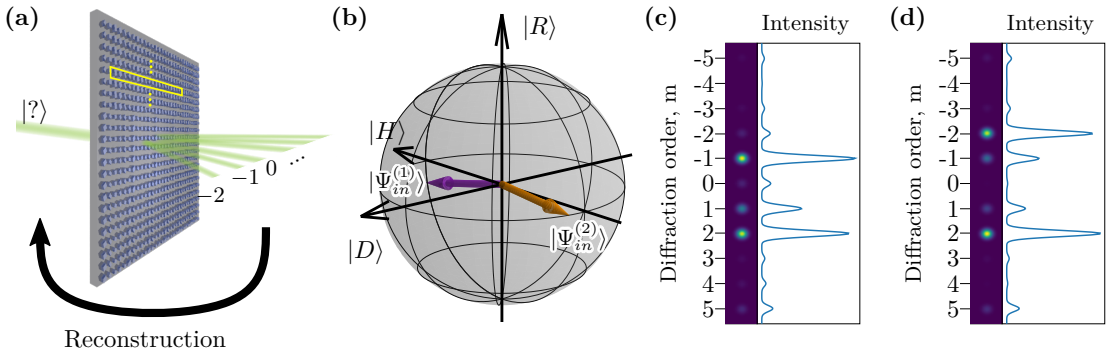

FIGURE 5.1: (a) Conceptual sketch of single-metagrating polarimetry. Highlighted in yellow is a single 16 resonator unit cell. From the output diffraction orders, any unknown input state may be reconstructed by knowing the metasurface instrument matrix. (b) Poincaré sphere representation of two arbitrarily chosen input states $|\Psi_{in}^{(1)}\rangle$, $|\Psi_{in}^{(2)}\rangle$ characterized in Jones formalism by the polarization angles and phases $(1.5, 0.1)$, $(0.1, 1.5)$ respectively. (c,d) Intensities of output diffraction orders corresponding to the respective input states $|\Psi_{in}^{(1)}\rangle$, $|\Psi_{in}^{(2)}\rangle$.

5.1 Theory for single-shot polarimetry

We first establish that each diffraction order, denoted by an index m, may be considered independently of each other, each transforming the input polarization state (quantum or otherwise). Furthermore, working under a linear regime, we may express the transformation of quantum states as follows:

$$\psi_{out}^{(m)} = \mathbf{T}^{(m)}\psi_{in}, \tag{5.1}$$

or equivalently under Stokes formalism as:

$$P_{out}^{(m)} = \mathbf{M}^{(m)} \cdot S_{in}, \tag{5.2}$$

where ψ_{in} and $\psi_{out}^{(m)}$ are the input and output polarization states for the respective diffraction order m, and $\mathbf{T}^{(m)}$ and $\mathbf{M}^{(m)}$ denote the classical 2×2 Jones transfer matrix and 1×4 instrument matrix respectively. They are related via the expression

$$\mathbf{M}^{(m)} = \frac{1}{2} \begin{pmatrix} \rho_{00} + \rho_{10} \\ \rho_{00} - \rho_{10} \\ \rho_{01} + \rho_{10} \\ (\rho_{10} - \rho_{01})i \end{pmatrix}, \tag{5.3}$$

where ρ_{ij} are the the elements of the 2×2 density matrix $\mathbf{T}^{(m)} * . \mathbf{T}^{(m)}$, indexed by $0, 1$. This is equivalent to the first row of the Stokes matrix under Mueller notation.

Considering each individual diffraction order as a polarizer acting on incident light, we perform a SVD of the transfer matrices, as in 2.5. Knowing that this decomposition establishes the degree of transmission of the polarization states (equivalent to the eigenstates of $\mathbf{W}^{\dagger}$), we note that if $\sigma_2^{(m)} = 0$, the transformation is that of a perfect polarizer, fully filtering out any orthogonal polarization. Conversely, if $\sigma_2^{(m)} > 0$, then some degree of the orthogonal polarization state is transmitted, establishing the transformation as a partial polarizer, with a power extinction ratio of $(\sigma_2^{(m)}/\sigma_1^{(m)})^2$.

We now define the creation and annihilation operators from the input as $\hat{a}_p^{\dagger}$ and $\hat{a}_p$, where $p = \{H, V\}$ is the polarization state, and the respective output operators at each of the diffraction orders as $\hat{b}_p^{(m)\dagger}$ and $\hat{b}_p^{(m)}$. The transformation imposed by the metasurface is then expressed with the linear transfer matrix elements as:

$$\hat{b}_p^{(m)} = \sum_{p'=H,V} \left(\mathbf{T}_{p,p'}^{(m)}\right)^* \hat{a}_p \,, \quad \hat{b}_p^{(m)\dagger} = \sum_{p'=H,V} \mathbf{T}_{p,p'}^{(m)} \hat{a}_p^{\dagger} \,. \tag{5.4}$$

The scope of the work is limited to tomography of polarization-entangled states with a fixed number of input photons (N), which is a measurement that can prove challenging for practical reasons [135, 136, 137, 138, 139]. Despite this being a seemingly simple task, it is nevertheless one that is ubiquitous and utterly necessary to much of quantum optics; so long as an experiment produces output in polarization, it is necessary to measure, in some way, said output. Limiting the task to that of fixed input photons is similarly reasonable, with fixed input photon count experiments ranging from that of entangled biphoton states to those of quantum computing. The simplest type of click detectors are unable to resolve the number of incident photons, and nor are they capable of distinguishing the polarization state of said photons, and as such, a measurement technique such as demonstrated here can only prove beneficial. It is also known that the state characterization can be generalized to the regime when the maximum photon number is known using the approach of Ref. [131]. In the case of no more than one photon arriving at such a detector, positioned at the diffraction order m, then its response is governed by the

following POVM operator [140],

$$\hat{A}^{(m)} = \sum_{p=H,V} \hat{b}_p^{(m)\dagger} \hat{b}_p^{(m)} = \sum_{p,p'=H,V} \mathbf{A}_{p,p'}^{(m)} \hat{a}_p^\dagger \hat{a}_{p'} \ , \tag{5.5}$$

where using Eqs. (2.5) and (5.4) we can calculate the matrix expression

$$\begin{aligned} \mathbf{A}^{(m)} &= \left(\mathbf{T}^{(m)}\right)^\dagger \mathbf{T}^{(m)} \\ &= \sum_{j=1,2} \sigma_j^{(m)} \left|\mathbf{W}_j^{(m)}\right\rangle \left\langle \mathbf{W}_j^{(m)}\right| \\ &= (\sigma_1^{(m)} - \sigma_2^{(m)}) \left|\mathbf{W}_1^{(m)}\right\rangle \left\langle \mathbf{W}_1^{(m)}\right| + \sigma_2^{(m)} \mathbf{I}. \end{aligned} \tag{5.6}$$

We see that this is a sum of a polarization projection operator and a polarization-insensitive detection. The presence of the latter term is a consequence of the partial-polarizer transformation at each of the diffraction orders. Although conventional polarimetry requires near-perfect polarizers (i.e. $\sigma_2^{(m)} = 0$), we find that POVM formalism enables unique and accurate quantum state reconstruction in the regime of $\sigma_2^{(m)} > 0$.

After determining the detection operators, we find the probabilities of the simultaneous detection of N photons by a combination of N detectors at the diffraction orders $m_1, m_2, \ldots m_N$, when there is exactly one photon at each detector. These are proportional to the corresponding photon correlations:

$$\Gamma(m_1, m_2, \ldots, m_N) = \mathrm{Tr}(\rho_N \hat{A}_{m_1} \hat{A}_{m_2} \cdots \hat{A}_{m_N}), \tag{5.7}$$

where ρ_N is an input density matrix. Then, we follow an established procedure [99, 141] to enumerate with index q all the possible N combinations of M detectors, $(m_1, m_2, \ldots, m_N)$ and rewrite Eq. (5.7) in an equivalent form,

$$\Gamma_q = \sum_{s=1}^{S} \mathbf{B}_{p,s} r_s \ . \tag{5.8}$$

Here r_s are the independent real and imaginary parts of the input density matrix defined according to the procedure in Ref. [138], $S = (N+3)!/(3!N!)$, $q = 1, \ldots, Q$, $Q = M!/(N!(M-N)!)$, and M is the total number of detected diffraction orders. The matrix elements $\mathbf{B}_{p,s}$ depend on the transfer matrix elements, and more specifically on the vectors $\mathbf{W}_j^{(m)}$ and singular values $\sigma_p^{(m)}$ according to the form of Eq. (5.6). We can then reconstruct an input state from the correlation measurements by performing a pseudo-inversion of Eq. (5.8), provided the number of different correlations matches or exceeds the number of unknowns, $Q \geq S$,

$$M \geq N + 3 \ . \tag{5.9}$$

In addition to the necessary condition as laid out in Eq. (5.9), we impose the additional design restriction that the reconstruction results are robust in the presence of experimental errors in the correlation measurements, whether these arise from fabrication errors in the metasurface, equipment imprecision, or other similar sources. We may conveniently express this requirement via the condition number κ of matrix $\mathbf{B}$, defined as the ratio of its largest and smallest singular values [142, 143, 99]. The condition number of an equation characterizes the worst-case error in output for a given error in the set of input parameters [144, 145]. In particular, we may contextualize this condition number in terms of the reconstruction of the input polarization state from the power via the inverse of Eq. 5.2:

$$S_{in} = \mathbf{M}^{-1} \cdot P_{measured}, \tag{5.10}$$

where $P_{measured}$ and S_{in} are the complete measurement vectors and reconstructed polarization state, under the Stokes basis. We may also formulate the propagation of errors based on this as:

$$\Delta S_{in} = \mathbf{M}^{-1} \cdot \Delta P_{measured}. \tag{5.11}$$

From here we may calculate the norm of all quantities, and utilize Cauchy's Inequality to find that an upper bound exists as:

$$||\Delta S_{in}|| = ||\mathbf{M}^{-1}|| \cdot ||\Delta P_{measured}||. \tag{5.12}$$

It then becomes natural to consider the *relative* error of reconstruction, in the form of $\Delta S_{in}/S_{in}$, and as such, we obtain:

$$\frac{||\Delta S_{in}||}{||S_{in}||} \leq ||(\mathbf{M}^{-1})^{-1}||||\mathbf{M}^{-1}|| \cdot \frac{||\Delta P_{measured}||}{||P_{measured}||} = ||\mathbf{M}||||\mathbf{M}^{-1}|| \cdot \frac{||\Delta P_{measured}||}{||P_{measured}}||. \tag{5.13}$$

We see here that $||\mathbf{M}||||\mathbf{M}^{-1}||$ essentially defines the worst-case scaling of the relative error of the measurement as compared to that of the output, and as such, it characterizes the robustness of the system. This value is the inverse condition number of the system [146, 147, 139],

$$\kappa^{-1} = ||\mathbf{M}||||\mathbf{M}^{-1}||. \tag{5.14}$$

As we can see from Eq. 5.13, in the limit of $\kappa^{-1} \to \infty$, reconstruction of S_{in} becomes impossible. Conversely, minimization of the inverse condition number results in a perfect reconstruction, and as such, becomes a straightforward path towards the practical design of such a the metasurface.

5.2 Numerical design procedure

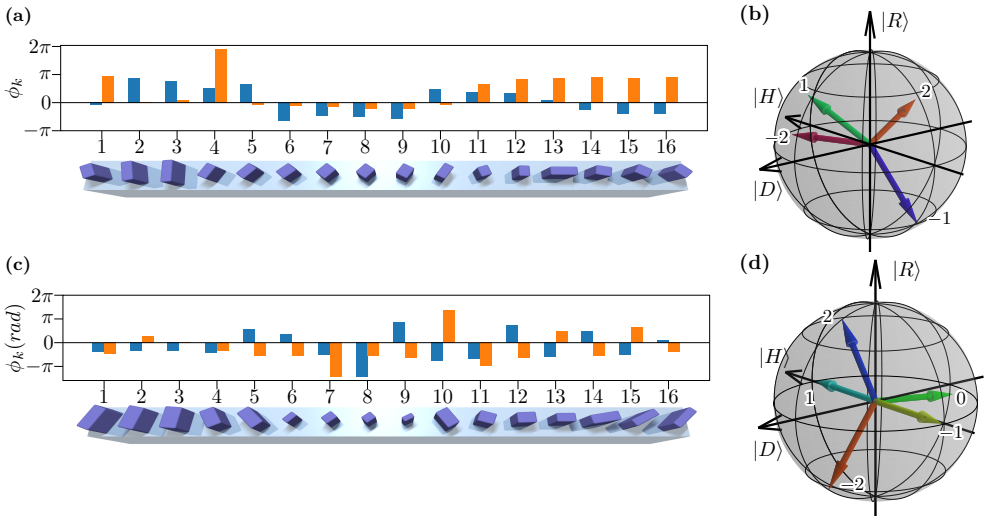

FIGURE 5.2: (a) Ordinary and extra ordinary phase retardances (ϕ_o, ϕ_e) for a metasurface numerically optimized for polarimetry of a single incoming photon state. The render shows the metasurface calculated via analytical calculations and Rigorous Coupled Wave Analysis (RCWA), including the angles to which each element is rotated. The metasurface was designed as $832nm$ thick amorphous silicon on glass, and has an inverse condition number $1/\kappa = 0.573$, close to the theoretical limit of $1/\sqrt{2}$. (b) Poincaré sphere representation of partially polarized diffraction orders $(\pm 2, \pm 1)$ used as the basis states to affect the single-shot polarimetry using the metasurface shown in (a). (c) Phase retardances and three-dimensional render of a metasurface designed for polarimetry of an incoming bi-photon state, simulated for $790nm$ thick amorphous silicon on glass. This has an inverse condition number of 0.170. (d) Basis states for $(\pm 2, \pm 1, 0)$ single-shot polarimetry of bi-photon states.

The metasurface was designed and optimized in multiple steps. First, multi-stage optimization of the metagrating's phase parameters was performed via a semi-analytical approach, targeting the most robust polarization reconstruction using the inverse condition number κ^{-1}. Knowing that each cuboidal resonator defines a transfer matrix $\mathbf{T}_{single}$ as in Eq. 2.17, we may readily define a metagrating as the action of some number of pixels arranged into a periodic supercell, as shown in Fig. 5.2(a,c). It is therefore possible to analytically calculate the transformation matrix of the metasurface using the fourier transform.

$$\mathbf{T}^{(m)} = \sum_{j=1}^{N} \mathbf{T}^{(j)}_{single} e^{-\frac{2\pi i}{N} mn}, \tag{5.15}$$

where N is the total number of elements in a single unit cell, each of which has a transfer matrix $\mathbf{T}^{(j)}_{single}$. This was implemented numerically using a fast fourier transform, thus allowing for the calculation of the condition number as the ratios of the maximum and minimum singular value decomposition values. By minimizing the condition number, it is thus possible to optimize towards a highly robust design. This optimization produced a set of phase parameters corresponding to each pixel of the unit cell, consisting of phase-shifts along the ordinary and extraordinary axes of each pixel ($\phi_o^{(j)}$, $\phi_e^{(j)}$) as well as the angle of each pixel ($\theta^{(j)}$), which may be seen in 5.2(a,c) for one- and two-photon designs respectively. This also allowed us to calculate the basis states of the diffraction orders to be used for the reconstruction, demonstrating that they are clearly non-orthogonal.

As implied by Eq. 5.6, the vectors $\mathbf{W}_j^{(m)}$ are the basis states of the projection measurement. By converting these to a Stokes basis, these may be plotted on a Poincaré sphere for convenient visualization of the basis states implemented by a given metasurface design, as shown in Fig. 5.2(b, d), with the lengths normalized as

$$R = 1 - \frac{P_{min}}{P_{max}}, \tag{5.16}$$

where P_{min} and P_{max} are the minimum and maximum powers transmitted to the relevant diffraction order, representing the relative best-case powers at each diffraction order. Furthermore, this provides a convenient conversion between the Jones transfer matrix formalism (Eq. 5.1) and the instrument matrix formalism (Eq. 5.2): The vector components of the instrument matrix ($In_1^{(m)}$, $In_2^{(m)}$, $In_3^{(m)}$) are exactly equivalent to the basis state vector as derived from $\mathbf{W}_j^{(m)}$.

Similar to the methodology discussed in section 2.3, a physical parameter sweep of cuboidal pixels was then computed using RCWA, thus producing a phase map from which suitable designs could be selected analytically. The physical parameters of the metasurface were then designed by selecting pixels from the sweep that fit desired phase parameters ($\phi_o^{(j)}$, $\phi_e^{(j)}$), up to an arbitrary global phase, while accounting for the rotations of the pixels ($\theta^{(j)}$). This thus greatly simplifies the design process, reducing the parameters considered to just the length and widths of the cuboidal pixels. The combined metasurface structure thus designed was then simulated using a commercial electrodynamics solver, CST Studio, as a final optimization pass and safeguard against second and higher order interactions between adjacent pixels that are not accounted for in the analytical design.

5.3 Robustness of reconstruction

Based on the POVM formulation of the design, strong robustness against fabrication errors is both a target and an expected design outcome of the metasurface. Accordingly, additional analysis was performed to demonstrate this stability, using the numerical designs from the previous section, for single- and double-

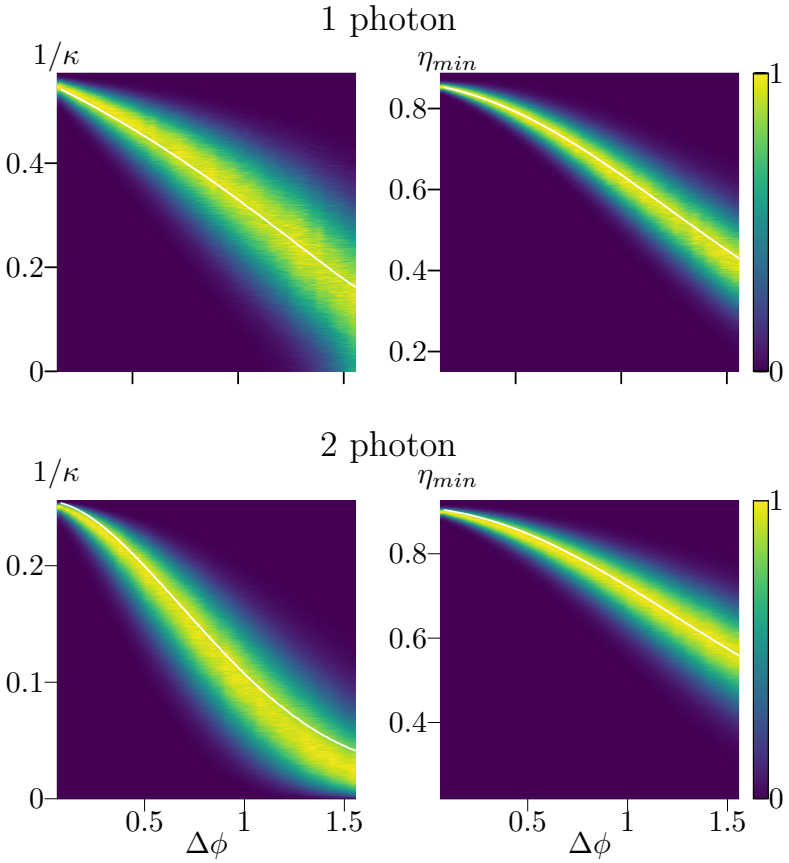

FIGURE 5.3: Plots demonstrating the resistance to random fabrication error $\Delta\phi$ of the single and double photon metasurface designs. The numerically calculated designs were perturbed by adding random errors up to a maximum of $\Delta\phi$ to each of the nanoresonator elements, and the inverse condition numbers κ^{-1} and diffraction efficiencies η_{min}, defined as the minimum power that is captured within the diffraction orders used. The errors were randomized 100000 times for each value of $\Delta\phi$, and the results normalized at each value to a total probability of 1.

photons, random errors were introduced, and the resultant metasurface evaluated for performance. The metrics chosen for this evaluation were the inverse condition number (κ^{-1}), representative of the precision of a tomography reconstruction with the metasurface, and the diffraction efficiency η_{min}, defined as the minimum power diffracted for each of the chosen diffraction orders and representative of the power, or number of photons collected at each diffraction order.

Under realistic fabrication scenarios, the most common deviations from the analytical design pertain to the overall sizes of the nanoresonators. This were modelled as variance in the phase shifts along the ordinary and extraordinary axes of the individual nanopixels, corresponding to the decomposition shown in Eq. 2.17, and thus, random, independent errors up to $\delta\phi$ were added to each nanopixel, and the overall transmission of the altered metasurface structure calculated via superposition of the electric fields and subsequent fourier transformation. From this result, we computed the overall inverse condition number for the altered metasurface. By trialing large numbers of errors, we estimated the falloff of performance with the degree of random error, as shown in 5.3. The errors trialed range up to an extreme case of $\Delta\phi = \pi/2$, which may be considered to be laughably and unrealistically large by the standards of current fabrication technology.

We find that for realistic levels of error, on the order of 10^{-1}, both the inverse condition number and the diffraction efficiencies do not drop significantly, as shown in Fig. 5.3. However, as one might expect, the double-photon design is more sensitive to error than the single-photon design, owing to the necessary consideration of additional diffraction orders to fully resolve multiple photons.

For much larger error values $\Delta\phi$, the average polarization extinction ratio drops from over 5dB (when metasurface acts as a set of reasonably good polarizers) to around 2dB (metasurface implements quite poor polarizers) [Fig. 5.3(b)]. Nevertheless, the minimum diffraction efficiency to the four selected spots remains quite high (over 55%) [Fig. 5.3(c)] and the inverse condition number of a calibrated metasurface remains within 30% of the fundamental limit indicated with the dashed line [Fig. 5.3(d)]. This corresponds to a moderate increase of reconstruction error by a factor of 3, even under extreme structural deviations that are much worse then the standard fabrication accuracy.

5.4 Fabrication

The fabrication of this metasurface was performed as a collaborative effort with the University of Jena in Germany, and as such, varies from previous work. The metasurfaces were fabricated from a $832nm$-thick amorphous silicon layer prepared at the ANU node of Australian Nanofabrication Facility (ANFF) using Plasma-Enhanced Chemical Vapor Deposition (PECVD) on a glass substrate[1]. It was subsequently

[1]Deposition was performed by Khosro Zangeneh Kamali using facilities at ANU's ANFF

etched at the University of Jena using Electron Beam Lithography (EBL) and Inductively Coupled Plasma (ICP) etching. As before, slight variants in the prepared metasurfaces were prepared by in turn varying the EBL exposure times, accounting for minor errors due to fabrication error.

5.5 Experimental characterization

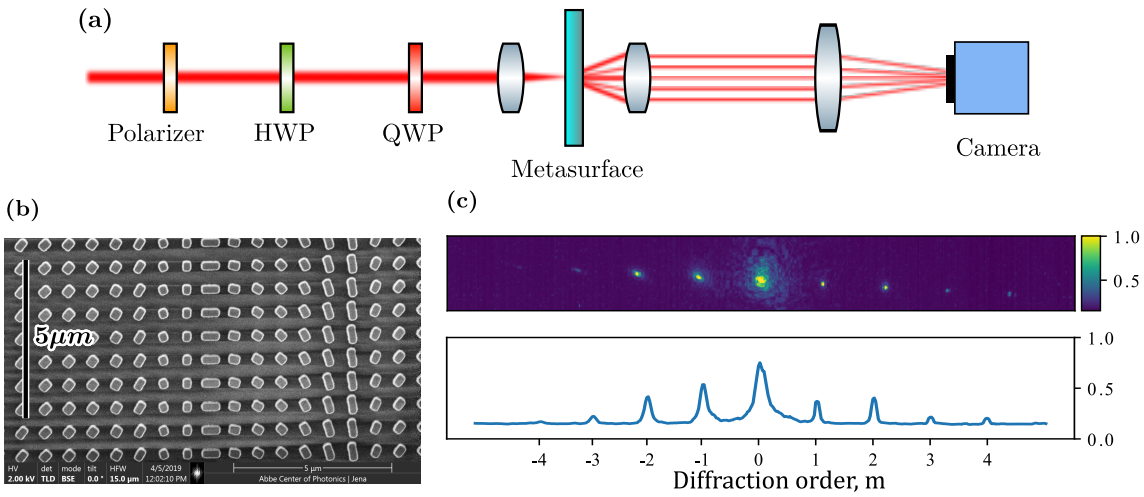

FIGURE 5.4: (a) Schematic of the experimental setup used to classically characterize the metasurface. Input states were prepared from a variable-wavelength infrared laser using a fixed polarizer and motorized half- and quarter- waveplates, before being collimated on the metasurface by lenses. Output diffraction order intensities were collected using a CCD camera. (b) Scanning Electron Microscope (SEM) image of the metasurface, fabricated as $832nm$ amorphous silicon on glass via electron beam lithography. (c) Representative reading as taken using the camera, and the processed intensity plot obtained by slicing across the diffraction orders. Intensities were normalized to 1.

After fabrication, the metasurfaces were characterized using the experimental setup shown in Fig. 5.4(a). The experiment was performed fully in free-space. Using a half-waveplate, quarter waveplate and fixed polarizer, polarization states were prepared from a variable-wavelength laser operating in the $1500 - 1575nm$ telecommunications bandwidth. The prepared polarization state was then focused to a spotsize of approximately $1\mu m$ normally incident on the metasurface. The diffraction orders were then collected using an objective lens with a high numerical aperture, and further focused onto an infrared CCD camera using a convex lens. No polarization-dependent modification was performed to the output of the metasurface. As a separate measurement, the camera was replaced with a calibrated power meter in order to determine the total power that was transmitted

through the metasurface.

The intensities of the diffraction orders over varying input polarization orders were thus captured as images in the camera, as shown in Fig. 5.4(c). The diffraction order spot locations were determined by hand, and the individual intensities were extracted by integrating the total intensities around each location. Working in the Stokes formalism for convenience, each diffraction order was then fitted individually by minimizing the nLMS parameter according to Eq. 5.2.

The individually fitted instrument matrix vectors were then combined to recover the full instrument matrix of the metasurface as a $4 \times m$ matrix. By normalizing this according to the degenerate elements of the density matrix, we may calculate the N-photon inverse condition number of the reconstruction [148].

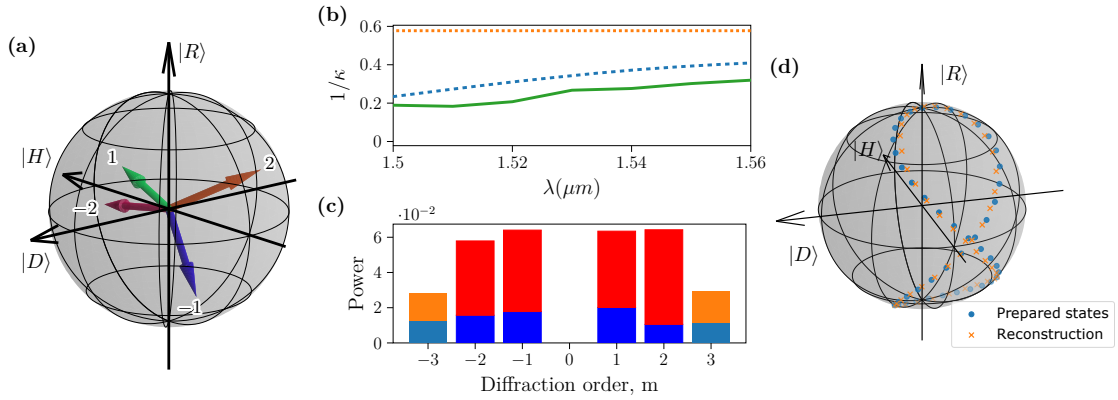

FIGURE 5.5: (a) Poincaré sphere representation of the basis states as calculated from the $(\pm 2, \pm 1)$ diffraction orders of the fabricated metasurface. These are, as predicted, partially polarized states. (b) The experimentally characterized inverse condition numbers of the metasurface across a wavelength range are plotted using the solid green line. The blue, dashed line represents the original RCWA design target, and the orange, dotted line represents the theoretical maximum. (c) The minimum and maximum power directed to each diffraction order, as determined by experiment. (d) Poincaré sphere showing a comparison of input states versus the reconstructed states using the experimentally characterized metasurface.

In the case of the representative results shown in Fig. 5.5, m was 4, comprising the chosen diffraction orders $(-2, -1, 1, 2)$, with the maximum nLMS fitting parameter of these determined to be no larger than 8.7×10^{-6}. From this characterization, we compute first the polarization bases of the instrument matrix, as in Eq. 5.16, and plot these polarization bases in Fig. 5.5(a), calculated at a wavelength of at $1560nm$. Here, we see that the polarization bases have deviated from the original designed

values as shown in Fig. 5.2(a), which may be ascribed to deviations from the numerical design due to fabrication error. This is both expected and accounted for by the robustness computations in Section 5.3. Notably, the degree of polarization of each basis is lower than the original values, up to 12% less in the -2 diffraction order.

Despite these deviations from the original design, the analytical concepts underlying this metasurface concept allow us to determine its usability. Accordingly, we further computed and plotted the inverse condition number across a wavelength sweep from $1500 - 1560\mu m$, along with the inverse condition number from the original numerical design for comparison. These are shown in Fig. 5.5(b), and from this characterization, we see that the experimentally calibrated inverse condition number is lower than the design target by up to 15%, with a maximum value of 0.24 at $1560nm$. It is possible that the condition number improves further at higher wavelengths, however, this was not accessible due to equipment limitations.

From the experimental data as well as the instrument matrix of the metasurface, a reconstruction was performed. From experimental data, an arbitrary range of angles for the half- and quarter- waveplates were chosen. From these angles, and knowing that the first polarizer was positioned vertically, we thus know the polarization states ψ_{in} before incidence on the metasurface, accounting for experimental angular misalignment of the optical elements. From these input states and the measured powers as determined from the camera, we also compute the states reconstructed from the measured intensities P_{out} and the experimentally characterized instrument matrix $\mathbf{M}$, as with Eq. 5.10. We then plotted these on the same Poincaré sphere for comparison, as shown in Fig. 5.5, and thus demonstrate that the reconstruction is successful up to known error. Notably, as the degree of imperfection of the polarization measurements is fully described in our POVM formalism, the metagrating can be calibrated after the fabrication and hence promises extremely high accuracy.

This reconstruction has a maximum deviation from the original polarization state of a maximum of 6%, using a phase-sensitive fidelity measure

$$\delta = 1 - \frac{Re\left(\sum_i \psi_i^* \widetilde{\psi}_i\right)^2}{\sum_i \psi_i^* T_i \sum_i \widetilde{\psi}_i^* \widetilde{\psi}_i}, \tag{5.17}$$

where ψ and $\tilde{\psi}$ are the original and reconstructed polarization states in the Jones notation. This is derived in the same way as the phase-*invariant* fidelity in Eq. 2.18. Note that this 6% does not constitute an exhaustive characterization of the full polarization space, and serves merely to demonstrate the reconstruction capabilities of the metasurface.

5.6 Summary

An important advantage of our approach based on POVM formalism is that it can facilitate accurate polarization reconstruction even in presence of significant fabrication errors, by only performing a single post-fabrication device calibration. We anticipate that our new concept will facilitate diverse applications and lead to the development of optimal polarization state imaging tailored for computer vision and quantum state characterization.

Chapter 6

Conclusion

In my thesis, I have explored many key aspects of polarization in its applications towards endeavours both fundamental and practical, augmenting already-extant capabilties with concepts that are both novel and firmly grounded in what may be achieved in experiment. This approach was demonstrated in numerical works and in experiment, and yet, there remains much room for improvement and exploration.

Firstly, in Chapter 2, I established the concept of complex birefringence using metasurfaces. While this is not an entirely novel concept, it has, prior to this point, been confined exclusively to theoretical considerations due to the lack of feasible fabrication. This original theoretical proposal involved a layered structure comprising engineered gain and loss media, the former of which is highly impractical to create in such a manner. Instead, in this thesis a path towards a practical implementation was developed, beginning with an analytical framework developed by recognising that a non-Hermitian transfer matrix does not necessarily involve gain. While gain would in this case be necessary to maintain a unitary transmission, it was demonstrated in theory that a similar mathematical transformation could be attained using only loss. This new form of birefringence is capable of rotating polarization states independently of each other in a polarization-dependent manner, thus yielding an entirely novel degree of freedom in experimental design.

Also developed in Chapter 2 were general numerical design, fabrication and experimental techniques that were applied throughout my thesis, namely, that of binary metasurfaces. Binary metasurfaces are a combination of two types of simple, cuboidal pixels in a 2×2 grid to form a supercell that is tiled periodically to create the overall metasurface structure. These proved to be a simple yet powerful method for implementing the necessary metasurfaces utilized throughout most of this thesis. The numerical techniques were accomplished in multiple stages, beginning with a relatively coarse, gridded numerical approach to determine finer optimization ranges, allowing for the rapid determination of the desired performance and transformation.

Through fabrication and classical characterization in experiment, I demonstrate that the concept of complex birefringence via engineered loss is both achievable and flexible. There is potential for extending to robustness, related to the concepts later discussed in Chapter 5, but even so, the method proved reliable and usable even without this utility. With the newly revealed design degree of freedom that it

offers, complex birefringence as a platform is capable of highly compact polarization manipulations utilizing only a single metasurface. Not only can this directly replace analogous operations in bulk optics, thus substantially cutting down on the size and complexity of optical setups, it also serves as a practical implementation of general non-Hermiticity in the direct transmission mode of metasurfaces, with applicability in a vast array of experiments.

Complex birefringence is a flexible principle, and one that was further developed in Chapter 3 to extend to quantum applications. I demonstrate that complex birefringence can be utilized for a key aspect of control in quantum optics, namely, that of the degree of entanglement in polarization-correlated states, which are an especially ubiquitous form of entanglement, arising as they do from SPDC sources. This form of control accomplishes a common task that is critical to many applications of entangled biphotons, and furthermore is an additional tool to be used in the fields of quantum weak measurements, quantum cryptography and computing. In particular, it can be used as a foundational building block with which to design quantum logic gates, as well as serving as a means for preparing and modifying qubits. However, due to the tight tolerances required to operate in quantum regimes, this aspect of complex birefringence remains one that requires further research, especially in the quality of the metasurfaces used.

In Chapter 4, I develop the concept of sensitive polarization monitoring, based on similar principles to complex birefringence. By transforming the anchor polarization state to be monitored to a well-defined state, any perturbations from this state may be shunted into an orthogonal state to that defined one, providing an easy means of monitoring these perturbations. With careful design, diffraction-based attenuation of the anchor state may be implemented while the perturbations are maximally transmitted, effectively providing an amplified ratio that can be trivially monitored and measured without the need for a full reconstruction of the polarization state. This technique is applicable to many practical aspects such as polarization microscopy, medical imaging, as well as materials manufacture. In many of these cases, it is sufficient and perhaps desirable to simply monitor the perturbations while utilizing as little operational overhead as possible to improve reaction speeds, as opposed to a full polarimetric reconstruction of the polarization state. This minimal overhead, highly sensitive response is exactly what I outline in this chapter, and could prove extremely useful in industrial and medical settings.

I also explored in this chapter the concept of chirality with binary metasurfaces. While dielectric metasurfaces are acknowledged to have notably lower chiral responses than their plasmonic metasurfaces, their chiral responses are non-negligible. As such, in keeping with the optimal analytical design goals for the polarization monitoring, a method of attaining chirality in a binary metasurface through inverse design was established, utilizing genetic algorithms to perform an inverse design process via numerical simulation. This established the potential for planar, binary metasurfaces to attain intrinsic chirality, arising from near-field coupling of adjacent metapixels. This particular aspect of dielectric metasurfaces bears future

exploration, potentially covering one of the noted weaknesses in dielectric media for metasurfaces.

Furthermore, the concept of complex birefringence may be enhanced by the addition of tunablity. A key aspect of complex birefringence is its relatively simple design approach while offering flexibility in implementation, however, as a passive metasurface, its properties are fundamentally locked in at the point of manufacture. While this can be desirable in some applications, providing stability for long-running experiments and installations, adding tunability can allow for even greater flexibility in cases such as polarization sensing, allowing for dynamic adjustment of the sensing parameters.

Finally, in Chapter 5, I explored the concept of single-shot polarimetry with metasurfaces. While the concept is not new, previous implementations possess notable weakness, largely revolving around the strict requirement of implementing near-perfect polarization filtering of incident light into different spatial paths, which are then captured as power readings on a camera for processing and reconstruction of the original, incident polarization state. This is not, however, a fundamental limitation of the principles involved in single-shot polarimetry, and by applying a concept known as Postive Operator Valued Measurements from quantum mechanics, we revealed that it is possible to utilize partially polarized spatial separation of incident polarization to uniquely and accurately perform polarimetry. Accompanying this approach is the concept of the condition number, which allows for the quantitative characterization of the degree of precision attainable with any given metasurface instrument matrix. This allows for highly robust implementations both in the design process as well as in the fabrication step, as any flaws in fabrication may be numerically estimated and accounted for with a one-time characterization step. Furthermore, we demonstrate here a metasurface that does not suffer from issues with beam quality or size, utilizing a minimally-sized periodic grating that does not require the illumination of a large surface area or cause substantial beam divergence in the far field.

To conclude, I have, through this thesis, demonstrated the flexibility and some of the capabilities of complex birefringence in manipulating polarized light, both in classical and quantum usecases. The application of judiciously engineered loss along with the high transmissivity of dielectric metasurfaces combine to form a powerful platform with myriad applications, and through experimental and analytical means, I have demonstrated that complex birefringence can be the answer to many practical and theoretical shortfalls in optics. There are still many aspects to explore, and this concept of complex birefringence, and carefully tailored losses, may prove to be the answer to myriad experimental problems.

Appendix A

Experimental characterization of the metasurface polarization transfer matrix

We use the experimental scheme presented in Fig. 2.2 of the main manuscript to characterize the metasurface transfer matrix. The power-meter readings are recorded over varying input states (θ_{in}) and the angle of the QWP (θ_Q), which are related to the metasurface transfer matrix $\mathbf{T}$ as follows:

$$P_{\mathrm{Det_A}} = |\langle \theta_{\mathrm{Pol_2}} | \mathbf{Q}(\theta_Q)\mathbf{T}|\theta_{in}\rangle|^2 P_{\mathrm{Det_B}}, \tag{A.1}$$

where $\theta_{\mathrm{Pol_2}}$ is the orientation angle of the linear polarizer ($\mathrm{Pol_2}$), $|\theta_{in}\rangle$ is the input linear polarization state at an angle of θ_{in} selected by a corresponding rotation of HWP, $\mathbf{Q}(\theta_Q)$ is the transmission matrix of the quarter-waveplate rotated at an angle θ_Q, and $P_{\mathrm{Det_{A,B}}}$ are the measured powers at the detectors A and B. Readings were recorded over varying input states (θ_{in}) and the angle of the QWP (θ_Q). We perform numerical fitting to reconstruct from the power measurements the transfer matrix $\mathbf{T}$, up to a global phase.

Here, we prove that this procedure enables accurate and unique reconstruction of the transfer matrix. Let us first consider an idealized situation in the absence of noise. Then, according to Eq. (A.1), the detected power dependence on the input polarization and QWP angles can be represented through the Fourier decomposition as

$$\begin{aligned} P_{\mathrm{r}}(\theta_{in}, \theta_Q; \mathbf{T}) = P_{\mathrm{Det_A}}/P_{\mathrm{Det_B}} = \sum_{p=0,\pm 2} \sum_{q=0,\pm 2,\pm 4} \Big[& \widetilde{P}_{c,c}(p,q)\cos(p\theta_{in})\cos(q\theta_Q) \\ & + \widetilde{P}_{c,s}(p,q)\cos(p\theta_{in})\sin(q\theta_Q) + \widetilde{P}_{s,c}(p,q)\sin(p\theta_{in})\cos(q\theta_Q) \\ & + \widetilde{P}_{s,s}(p,q)\sin(p\theta_{in})\sin(q\theta_Q)\Big] . \end{aligned} \tag{A.2}$$

To be specific, we consider the last polarizer angle to be fixed at $\theta_{\mathrm{Pol_2}} = 0$. We find that the measured angular Fourier components can be used to reconstruct the

absolute values of the transfer matrix elements as follows:

$$|T_{1,1}|^2 = [\widetilde{P}_{c,c}(0,0) + \widetilde{P}_{c,c}(2,0)] + [\widetilde{P}_{c,c}(0,4) + \widetilde{P}_{c,c}(2,4)], \quad (A.3)$$

$$|T_{2,1}|^2 = [\widetilde{P}_{c,c}(0,0) + \widetilde{P}_{c,c}(2,0)] - 3\,[\widetilde{P}_{c,c}(0,4) + \widetilde{P}_{c,c}(2,4)], \quad (A.4)$$

$$|T_{1,2}|^2 = [\widetilde{P}_{c,c}(0,0) - \widetilde{P}_{c,c}(2,0)] + [\widetilde{P}_{c,c}(0,4) - \widetilde{P}_{c,c}(2,4)], \quad (A.5)$$

$$|T_{2,2}|^2 = [\widetilde{P}_{c,c}(0,0) - \widetilde{P}_{c,c}(2,0)] - 3\,[\widetilde{P}_{c,c}(0,4) - \widetilde{P}_{c,c}(2,4)]. \quad (A.6)$$

Then, the phases can be found from the following relations, up to a global phase:

$$T_{2,1}T_{1,1}^* = [i\,\widetilde{P}_{c,s}(0,2) + 2\,\widetilde{P}_{c,s}(0,4)) + [i\,\widetilde{P}_{c,s}(2,2) + 2\,\widetilde{P}_{c,s}(2,4)], \quad (A.7)$$

$$T_{2,2}T_{1,2}^* = [i\,\widetilde{P}_{c,s}(0,2) + 2\,\widetilde{P}_{c,s}(0,4)) - [i\,\widetilde{P}_{c,s}(2,2) + 2\,\widetilde{P}_{c,s}(2,4)], \quad (A.8)$$

$$\mathrm{Re}(T_{1,2}T_{1,1}^*) = \widetilde{P}_{s,c}(2,0) + \widetilde{P}_{s,c}(2,4) \quad (A.9)$$

$$\mathrm{Re}(T_{2,2}T_{2,1}^*) = \widetilde{P}_{s,c}(2,0) - 3\,\widetilde{P}_{s,c}(2,4) \quad (A.10)$$

$$T_{2,2}T_{1,1}^* + T_{2,1}T_{1,2}^* = i\,\widetilde{P}_{s,s}(2,2) + 2\,\widetilde{P}_{s,s}(2,4). \quad (A.11)$$

This analysis establishes the possibility to reconstruct both the amplitude and phase of the transfer matrix elements. However, there can be an ambiguity in determining the phase for a specific case of $T_{2,2}T_{1,1} = T_{2,1}T_{1,2}$ as then the equations are invariant to a simultaneous change of sign in solutions $\arg T_{1,2} = \arg T_{1,1} \pm \rho$, and $\arg T_{2,2} = \arg T_{2,1} \pm \rho$, where ρ is determined from Eq. (A.9). Importantly, since we operate at normal incidence, the chiral effects are weak and the transfer matrix is close to symmetric, such that $T_{2,1} \simeq T_{1,2}$, and the latter condition makes the reconstruction unique by removing the phase ambiguity.

In practice, the reconstruction based on experimental data is performed by finding the transfer matrix elements that provide the best fit between the measured powers at the specific waveplate orientations and the expression according to Eq. (A.1). The accuracy of reconstruction was monitored by checking the mismatch of the least means squares fitting,

$$\delta P^{(\mathrm{fit})}(\mathbf{T}) = \frac{\sum_i^N \left(P_r^{(\mathrm{fit})}(\theta_{in}^{(i)}, \theta_Q^{(i)}; \mathbf{T}) - P_r(\theta_{in}^{(i)}, \theta_Q^{(i)})\right)^2}{\sum_i^N \left(P_r(\theta_{in}^{(i)}, \theta_Q^{(i)})\right)^2}, \quad (A.12)$$

where N is the total number of measurements, $\theta_{in}^{(i)}$ and $\theta_Q^{(i)}$ are the angles at the i-th measurement, and $P_r^{(\mathrm{fit})}$ is the predicted transmission ratio from Eq. (A.1).

Bibliography

[1] Sergey Kruk and Yuri Kivshar. "Functional meta-optics and nanophotonics governed by Mie resonances". *Acs Photonics* 4.11 (2017), pp. 2638–2649.

[2] Taiwan Semiconductor Manufacturing Company Limited. *7nm Technology*. 2021. URL: https://www.tsmc.com/english/dedicatedFoundry/technology/logic/l_7nm (visited on 10/04/2021).

[3] F.J. Dijksterhuis. *Lenses and Waves: Christiaan Huygens and the Mathematical Science of Optics in the Seventeenth Century*. Springer Netherlands, 2004. ISBN: 9781402026973. URL: https://books.google.com.au/books?id=cPFevyomPUIC.

[4] Dave3457. *Circular Polarizer Creating Left Handed Helix View*. 2015. URL: https://commons.wikimedia.org/wiki/File:Circular.Polarization.Circularly.Polarized.Light_Circular.Polarizer_Creating.Left.Handed.Helix.View.svg (visited on 10/04/2021).

[5] Ze'ev Bomzon, Vladimir Kleiner, and Erez Hasman. "Pancharatnam–Berry phase in space-variant polarization-state manipulations with subwavelength gratings". *Opt. Lett.* 26.18 (Sept. 2001), pp. 1424–1426. DOI: 10.1364/OL.26.001424.

[6] Dimitrios Tzarouchis and Ari Sihvola. "Light Scattering by a Dielectric Sphere: Perspectives on the Mie Resonances". *Applied Sciences* 8.2 (2018). ISSN: 2076-3417. DOI: 10.3390/app8020184.

[7] Amir Arbabi and Andrei Faraon. "Fundamental limits of ultrathin metasurfaces". *Scientific reports* 7.1 (2017), pp. 1–9.

[8] Jiao Lin, Patrice Genevet, Mikhail A Kats, Nicholas Antoniou, and Federico Capasso. "Nanostructured holograms for broadband manipulation of vector beams". *Nano letters* 13.9 (2013), pp. 4269–4274.

[9] A. Arbabi, Y. Horie, M. Bagheri, and A. Faraon. "Dielectric metasurfaces for complete control of phase and polarization with subwavelength spatial resolution and high transmission". *Nat. Nanotechnol.* 10.11 (Nov. 2015), 937–U190. DOI: 10.1038/NNANO.2015.186.

[10] Evan W. Wang, David Sell, Thaibao Phan, and Jonathan A. Fan. "Robust design of topology-optimized metasurfaces". *Opt. Mater. Express* 9.2 (Feb. 2019), pp. 469–482. DOI: 10.1364/OME.9.000469. URL: http://opg.optica.org/ome/abstract.cfm?URI=ome-9-2-469.

[11] Zin Lin, Benedikt Groever, Federico Capasso, Alejandro W. Rodriguez, and Marko Lon čar. "Topology-Optimized Multilayered Metaoptics". *Phys. Rev. Applied* 9 (4 Apr. 2018), p. 044030. DOI: 10.1103/PhysRevApplied.9.044030. URL: https://link.aps.org/doi/10.1103/PhysRevApplied.9.044030.

[12] Dianmin Lin, Pengyu Fan, Erez Hasman, and Mark L Brongersma. "Dielectric gradient metasurface optical elements". *science* 345.6194 (2014), pp. 298–302.

[13] Shuming Wang, Pin Chieh Wu, Vin-Cent Su, Yi-Chieh Lai, Mu-Ku Chen, Hsin Yu Kuo, Bo Han Chen, Yu Han Chen, Tzu-Ting Huang, Jung-Hsi Wang, et al. "A broadband achromatic metalens in the visible". *Nature nanotechnology* 13.3 (2018), pp. 227–232.

[14] Z. L. Deng, M. K. Jin, X. Ye, S. Wang, T. Shi, J. H. Deng, N. B. Mao, Y. Y. Cao, B. O. Guan, A. Alu, G. X. Li, and X. P. Li. "Full-Color Complex-Amplitude Vectorial Holograms Based on Multi-Freedom Metasurfaces". English. 30.21 (May 2020), p. 1910610. DOI: 10.1002/adfm.201910610.

[15] D. Neshev and I. Aharonovich. "Optical metasurfaces: new generation building blocks for multi-functional optics". *Light-Sci. Appl.* 7 (Aug. 2018), pp. 58–5. DOI: 10.1038/s41377-018-0058-1.

[16] Thomas Konrad and Andrew Forbes. "Quantum mechanics and classical light". *Contemporary Physics* 60.1 (2019), pp. 1–22. DOI: 10.1080/00107514.2019.1580433.

[17] Alexander S Solntsev, Girish S Agarwal, and Yuri S Kivshar. "Metasurfaces for quantum photonics". *Nature Photonics* 15.5 (2021), pp. 327–336.

[18] E Altewischer, MP Van Exter, and JP Woerdman. "Plasmon-assisted transmission of entangled photons". *Nature* 418.6895 (2002), pp. 304–306.

[19] Pankaj K Jha, Xingjie Ni, Chihhui Wu, Yuan Wang, and Xiang Zhang. "Metasurface-enabled remote quantum interference". *Physical review letters* 115.2 (2015), p. 025501.

[20] Kai Wang, James G Titchener, Sergey S Kruk, Lei Xu, Hung-pin Chung, Matthew Parry, Ivan I Kravchenko, Yen-hung Chen, Alexander S Solntsev, Yuri S Kivshar, Dragomir N Neshev, and Andrey A Sukhorukov. "Quantum metasurface for multiphoton interference and state reconstruction". *Science (80-.).* 361.6407 (Sept. 2018), pp. 1104–1108. ISSN: 0036-8075. DOI: 10.1126/science.aat8196.

[21] Tomer Stav, Arkady Faerman, Elhanan Maguid, Dikla Oren, Vladimir Kleiner, Erez Hasman, and Mordechai Segev. "Quantum entanglement of the spin and orbital angular momentum of photons using metamaterials". *Science* 361.6407 (2018), pp. 1101–1104.

[22] Pankaj K Jha, Nir Shitrit, Jeongmin Kim, Xuexin Ren, Yuan Wang, and Xiang Zhang. "Metasurface-mediated quantum entanglement". *ACS Photonics* 5.3 (2017), pp. 971–976.

[23] Yuto Minami and Eiichiro Komatsu. "New Extraction of the Cosmic Birefringence from the Planck 2018 Polarization Data". *Phys. Rev. Lett.* 125 (22 Nov. 2020), p. 221301. DOI: 10.1103/PhysRevLett.125.221301.

[24] Zhongwen Zhan, Mattia Cantono, Valey Kamalov, Antonio Mecozzi, Rafael Müller, Shuang Yin, and Jorge C Castellanos. "Optical polarization–based seismic and water wave sensing on transoceanic cables". *Science* 371.6532 (2021), pp. 931–936.

[25] Maria-Rosaria Antonelli, Angelo Pierangelo, Tatiana Novikova, Pierre Validire, Abdelali Benali, Brice Gayet, and Antonello De Martino. "Mueller matrix imaging of human colon tissue for cancer diagnostics: how Monte Carlo modeling can help in the interpretation of experimental data". *Optics express* 18.10 (2010), pp. 10200–10208.

[26] Maria Duda, Natalie J Kirkland, Nargess Khalilgharibi, Melda Tozluoglu, Alice C Yuen, Nicolas Carpi, Anna Bove, Matthieu Piel, Guillaume Charras, Buzz Baum, et al. "Polarization of myosin II refines tissue material properties to buffer mechanical stress". *Developmental cell* 48.2 (2019), pp. 245–260.

[27] Harland G Tompkins and James N Hilfiker. *Spectroscopic Ellipsometry: Practical Application to Thin Film Characterization*. Momentum Press, 2015.

[28] Daniel F. V. James, Paul G. Kwiat, William J. Munro, and Andrew G. White. "Measurement of qubits". *Phys. Rev. A* 64 (5 Oct. 2001), p. 052312. DOI: 10.1103/PhysRevA.64.052312.

[29] NIL Technology. *NIL Technology*. 2021. URL: https://www.nilt.com/ (visited on 11/11/2021).

[30] Lumotive. *Lumotive*. 2021. URL: https://www.lumotive.com/ (visited on 11/11/2021).

[31] Nanxi Li, Zhengji Xu, Yuan Dong, Ting Hu, Qize Zhong, Yuan Hsing Fu, Shiyang Zhu, and Navab Singh. "Large-area metasurface on CMOS-compatible fabrication platform: driving flat optics from lab to fab". *Nanophotonics* 9.10 (2020), pp. 3071–3087. DOI: doi:10.1515/nanoph-2020-0063.

[32] Hui-Hsin Hsiao, Cheng Hung Chu, and Din Ping Tsai. "Fundamentals and Applications of Metasurfaces". *Small Methods* 1.4 (2017), p. 1600064. DOI: https://doi.org/10.1002/smtd.201600064.

[33] Christophe Vieu, F Carcenac, A Pepin, Y Chen, M Mejias, A Lebib, L Manin-Ferlazzo, L Couraud, and H Launois. "Electron beam lithography: resolution limits and applications". *Applied surface science* 164.1-4 (2000), pp. 111–117.

[34] Karl S Kunz and Raymond J Luebbers. *The finite difference time domain method for electromagnetics*. CRC press, 1993.

[35] Markus Clemens and Thomas Weiland. "Discrete electromagnetism with the finite integration technique". *Progress In Electromagnetics Research* 32 (2001), pp. 65–87.

[36] Olgierd Cecil Zienkiewicz, Robert Leroy Taylor, Perumal Nithiarasu, and JZ Zhu. *The finite element method*. Vol. 3. McGraw-hill London, 1977.

[37] MG Moharam and TK Gaylord. "Rigorous coupled-wave analysis of planar-grating diffraction". *JOSA* 71.7 (1981), pp. 811–818.

[38] Martin Hammerschmidt. *The Finite-Element Method (FEM) for Nano-Optics Simulations*. 2020. URL: https://jcmwave.com/company/blog/item/1049-fem-for-nano-optics-simulations (visited on 10/29/2021).

[39] Raphaël Pestourie, Carlos Pérez-Arancibia, Zin Lin, Wonseok Shin, Federico Capasso, and Steven G Johnson. "Inverse design of large-area metasurfaces". *Optics express* 26.26 (2018), pp. 33732–33747.

[40] Zhaocheng Liu, Dayu Zhu, Sean P Rodrigues, Kyu-Tae Lee, and Wenshan Cai. "Generative model for the inverse design of metasurfaces". *Nano letters* 18.10 (2018), pp. 6570–6576.

[41] R. Bellman, Rand Corporation, and Karreman Mathematics Research Collection. *Dynamic Programming*. Rand Corporation research study. Princeton University Press, 1957. ISBN: 9780691079516. URL: https://books.google.com.au/books?id=wdtoPwAACAAJ.

[42] A. Cerjan and S. H. Fan. "Achieving Arbitrary Control over Pairs of Polarization States Using Complex Birefringent Metamaterials". *Phys. Rev. Lett.* 118.25 (June 2017), pp. 253902–5. DOI: 10.1103/PhysRevLett.118.253902.

[43] Robert W Boyd. *Nonlinear optics*. Academic press, 2020.

[44] N. F. Yu and F. Capasso. "Flat optics with designer metasurfaces". *Nat. Mater.* 13.2 (Feb. 2014), pp. 139–150. DOI: 10.1038/nmat3839.

[45] Sanzheng Qiao and Xiaohong Wang. "Computing the singular values of 2-by-2 complex matrices". *McMaster University* (2002).

[46] S. V. Zhukovsky, A. V. Novitsky, and V. M. Galynsky. "Elliptical dichroism: operating principle of planar chiral metamaterials". *Opt. Lett.* 34.13 (July 2009), pp. 1988–1990. DOI: 10.1364/OL.34.001988.

[47] E. Plum, X. X. Liu, V. A. Fedotov, Y. Chen, D. P. Tsai, and N. I. Zheludev. "Metamaterials: Optical Activity without Chirality". *Phys. Rev. Lett.* 102.11 (Mar. 2009), pp. 113902–4. DOI: 10.1103/PhysRevLett.102.113902.

[48] J. P. Hu, X. N. Zhao, Y. Lin, A. J. Zhu, X. J. Zhu, P. J. Guo, B. Cao, and C. H. Wang. "All-dielectric metasurface circular dichroism waveplate". *Sci. Rep.* 7 (Jan. 2017), pp. 41893–9. DOI: 10.1038/srep41893.

[49] MR Dennis. "Polarization singularities in paraxial vector fields: morphology and statistics". *Optics Communications* 213.4-6 (2002), pp. 201–221.

[50] Z. Shi, A. Y. Zhu, Z. Li, Y.-W. Huang, W. T. Chen, C.-W. Qiu, and F. Capasso. "Continuous angle-tunable birefringence with freeform metasurfaces for arbitrary polarization conversion". *Science Advances* 6.23 (June 2020), eaba3367. DOI: 10.1126/sciadv.aba3367.

[51] Christoph Menzel, Carsten Rockstuhl, and Falk Lederer. "Advanced Jones calculus for the classification of periodic metamaterials". *Physical Review A* 82.5 (2010), p. 053811.

[52] Q. L. Yang, X. Y. Chen, Q. Xu, C. X. Tian, Y. H. Xu, L. Q. Cong, X. Q. Zhang, Y. F. Li, C. H. Zhang, X. X. Zhang, J. G. Han, and W. L. Zhang. "Broadband terahertz rotator with an all-dielectric metasurface". English. 6.11 (Nov. 2018), pp. 1056–1061. DOI: 10.1364/PRJ.6.001056.

[53] Z. L. Deng, J. H. Deng, X. Zhuang, S. Wang, K. F. Li, Y. Wang, Y. H. Chi, X. Ye, J. Xu, G. P. Wang, R. K. Zhao, X. L. Wang, Y. Y. Cao, X. Cheng, G. X. Li, and X. P. Li. "Diatomic Metasurface for Vectorial Holography". English. *Nano Lett.* 18.5 (May 2018), pp. 2885–2892. DOI: 10.1021/acs.nanolett.8b00047.

[54] Y. J. Bao, J. C. Ni, and C. W. Qiu. "A Minimalist Single-Layer Metasurface for Arbitrary and Full Control of Vector Vortex Beams". English. *Adv. Mater.* 32.6 (Feb. 2020), p. 1905659. DOI: 10.1002/adma.201905659.

[55] P. Lalanne. "Improved formulation of the coupled-wave method for two-dimensional gratings". *J. Opt. Soc. Am. A* 14.7 (July 1997), pp. 1592–1598. DOI: 10.1364/JOSAA.14.001592.

[56] P. Lalanne and G. M. Morris. "Highly improved convergence of the coupled-wave method for TM polarization". *J. Opt. Soc. Am. A* 13.4 (Apr. 1996), pp. 779–784. DOI: 10.1364/JOSAA.13.000779.

[57] Shaun Lung, Kai Wang, Khosro Zangeneh Kamali, Jihua Zhang, Mohsen Rahmani, Dragomir N Neshev, and Andrey A Sukhorukov. "Complex-birefringent dielectric metasurfaces for arbitrary polarization-pair transformations". *ACS Photonics* 7.11 (2020), pp. 3015–3022.

[58] Pauli Virtanen, Ralf Gommers, Travis E. Oliphant, Matt Haberland, Tyler Reddy, David Cournapeau, Evgeni Burovski, Pearu Peterson, Warren Weckesser, Jonathan Bright, Stéfan J. van der Walt, Matthew Brett, Joshua Wilson, K. Jarrod Millman, Nikolay Mayorov, Andrew R. J. Nelson, Eric Jones, Robert Kern, Eric Larson, C J Carey, İlhan Polat, Yu Feng, Eric W. Moore, Jake VanderPlas, Denis Laxalde, Josef Perktold, Robert Cimrman, Ian Henriksen, E. A. Quintero, Charles R. Harris, Anne M. Archibald, Antônio H. Ribeiro, Fabian Pedregosa, Paul van Mulbregt, and SciPy 1.0 Contributors. "SciPy 1.0: Fundamental Algorithms for Scientific Computing in Python". *Nature Methods* 17 (2020), pp. 261–272. DOI: 10.1038/s41592-019-0686-2.

[59] A. V. Burlakov and M. V. Chekhova. "Polarization optics of biphotons". *JETP Lett.* 75.8 (2002), pp. 432–438. DOI: 10.1134/1.1490017.

[60] AV Burlakov, MV Chekhova, OA Karabutova, DN Klyshko, and SP Kulik. "Polarization state of a biphoton: Quantum ternary logic". *Physical Review A* 60.6 (1999), R4209.

[61] T. Roger, S. Vezzoli, E. Bolduc, J. Valente, J. J. F. Heitz, J. Jeffers, C. Soci, J. Leach, C. Couteau, N. I. Zheludev, and D. Faccio. "Coherent perfect absorption in deeply subwavelength films in the single-photon regime". *Nat. Commun.* 6 (May 2015), pp. 7031–5. DOI: 10.1038/ncomms8031.

[62] B. Vest, M. C. Dheur, E. Devaux, A. Baron, E. Rousseau, J. P. Hugonin, J. J. Greffet, G. Messin, and F. Marquier. "Anti-coalescence of bosons on a lossy beam splitter". *Science* 356.6345 (June 2017), pp. 1373–1376. DOI: 10.1126/science.aam9353.

[63] N. Tischler, C. Rockstuhl, and K. Slowik. "Quantum Optical Realization of Arbitrary Linear Transformations Allowing for Loss and Gain". *Phys. Rev. X* 8.2 (Apr. 2018), pp. 021017–13. DOI: 10.1103/PhysRevX.8.021017.

[64] Y. C. Shen, N. C. Harris, S. Skirlo, M. Prabhu, T. Baehr-Jones, M. Hochberg, X. Sun, S. J. Zhao, H. Larochelle, D. Englund, and M. Soljacic. "Deep learning with coherent nanophotonic circuits". *Nature Photonics* 11.7 (July 2017), pp. 441–447. DOI: 10.1038/NPHOTON.2017.93.

[65] T Shi, Shanhui Fan, CP Sun, et al. "Two-photon transport in a waveguide coupled to a cavity in a two-level system". *Physical Review A* 84.6 (2011), p. 063803.

[66] Dirk Bouwmeester and Anton Zeilinger. "The physics of quantum information: basic concepts". In: *The physics of quantum information*. Springer, 2000, pp. 1–14.

[67] Dik Bouwmeester, Jian-Wei Pan, Klaus Mattle, Manfred Eibl, Harald Weinfurter, and Anton Zeilinger. "Experimental quantum teleportation". *Nature* 390.6660 (1997), pp. 575–579.

[68] Artur K Ekert, John G Rarity, Paul R Tapster, and G Massimo Palma. "Practical quantum cryptography based on two-photon interferometry". *Physical Review Letters* 69.9 (1992), p. 1293.

[69] Charles H Bennett. "Quantum cryptography using any two nonorthogonal states". *Physical review letters* 68.21 (1992), p. 3121.

[70] Jan Peřina Jr, Ondřej Haderka, and Jan Soubusta. "Quantum cryptography using a photon source based on postselection from entangled two-photon states". *Physical Review A* 64.5 (2001), p. 052305.

[71] S Magnitskiy, D Frolovtsev, V Firsov, P Gostev, I Protsenko, and M Saygin. "A SPDC-based source of entangled photons and its characterization". *Journal of Russian Laser Research* 36.6 (2015), pp. 618–629.

[72] Christophe Couteau. "Spontaneous parametric down-conversion". *Contemporary Physics* 59.3 (2018), pp. 291–304.

[73] Adeline Orieux, Andreas Eckstein, Aristide Lemaître, Pascal Filloux, Ivan Favero, Giuseppe Leo, Thomas Coudreau, Arne Keller, Pérola Milman, and Sara Ducci. "Direct Bell states generation on a III-V semiconductor chip at room temperature". *Physical review letters* 110.16 (2013), p. 160502.

[74] A. A. Clerk, M. H. Devoret, S. M. Girvin, F. Marquardt, and R. J. Schoelkopf. "Introduction to quantum noise, measurement, and amplification". *Rev. Mod. Phys.* 82.2 (Apr. 2010), pp. 1155–1208. DOI: 10.1103/RevModPhys.82.1155.

[75] Lucien Hardy. "Quantum mechanics, local realistic theories, and Lorentz-invariant realistic theories". *Phys. Rev. Lett.* 68 (20 Apr. 1992), pp. 2981–2984. DOI: 10.1103/PhysRevLett.68.2981.

[76] Kazuhiro Yokota, Takashi Yamamoto, Masato Koashi, and Nobuyuki Imoto. "Direct observation of Hardy's paradox by joint weak measurement with an entangled photon pair". *New Journal of Physics* 11.3 (2009), p. 033011.

[77] Jeff S Lundeen and Aephraim M Steinberg. "Experimental joint weak measurement on a photon pair as a probe of Hardy's paradox". *Physical review letters* 102.2 (2009), p. 020404.

[78] Itai Afek, Oron Ambar, and Yaron Silberberg. "High-NOON States by Mixing Quantum and Classical Light". *Science* 328.5980 (2010), pp. 879–881. DOI: 10.1126/science.1188172.

[79] Yuan Liang Lim and Almut Beige. "Generalized Hong–Ou–Mandel experiments with bosons and fermions". 7 (July 2005), pp. 155–155. DOI: 10.1088/1367-2630/7/1/155.

[80] Ben P Lanyon, Till J Weinhold, Nathan K Langford, Jeremy L O'Brien, Kevin J Resch, Alexei Gilchrist, and AG White. "Manipulating biphotonic qutrits". *Physical review letters* 100.6 (2008), p. 060504.

[81] Andrea Blanco-Redondo, Bryn Bell, Dikla Oren, Benjamin J Eggleton, and Mordechai Segev. "Topological protection of biphoton states". *Science* 362.6414 (2018), pp. 568–571.

[82] Jian-Wei Pan, Zeng-Bing Chen, Chao-Yang Lu, Harald Weinfurter, Anton Zeilinger, and Marek Żukowski. "Multiphoton entanglement and interferometry". *Rev. Mod. Phys.* 84 (2 May 2012), pp. 777–838. DOI: 10.1103/RevModPhys.84.777.

[83] Ryszard Horodecki. "Quantum entanglement". *Rev. Mod. Phys.* 81 (2 June 2009), pp. 865–942. DOI: 10.1103/RevModPhys.81.865.

[84] Alfred B U'Ren, Christine Silberhorn, Reinhard Erdmann, Konrad Banaszek, Warren P Grice, Ian A Walmsley, and Michael G Raymer. "Generation of pure-state single-photon wavepackets by conditional preparation based on spontaneous parametric downconversion". *arXiv preprint quant-ph/0611019* (2006).

[85] Chong-Ki Hong, Zhe-Yu Ou, and Leonard Mandel. "Measurement of subpicosecond time intervals between two photons by interference". *Physical review letters* 59.18 (1987), p. 2044.

[86] Frédéric Bouchard, Alicia Sit, Yingwen Zhang, Robert Fickler, Filippo M Miatto, Yuan Yao, Fabio Sciarrino, and Ebrahim Karimi. "Two photon interference: the hong-ou-mandel effect". *Reports on Progress in Physics* (2020).

[87] Emanuel Knill, Raymond Laflamme, and Gerald J Milburn. "A scheme for efficient quantum computation with linear optics". *nature* 409.6816 (2001), pp. 46–52.

[88] Sergey B Bravyi and Alexei Yu Kitaev. "Fermionic quantum computation". *Annals of Physics* 298.1 (2002), pp. 210–226.

[89] Zaki Leghtas, Steven Touzard, Ioan M Pop, Angela Kou, Brian Vlastakis, Andrei Petrenko, Katrina M Sliwa, Anirudh Narla, Shyam Shankar, Michael J Hatridge, et al. "Confining the state of light to a quantum manifold by engineered two-photon loss". *Science* 347.6224 (2015), pp. 853–857.

[90] Maryam Sakhdari, Mohamed Farhat, and Pai-Yen Chen. "PT-symmetric metasurfaces: wave manipulation and sensing using singular points". *New Journal of Physics* 19.6 (2017), p. 065002.

[91] Paul G Kwiat, Salvador Barraza-Lopez, Andre Stefanov, and Nicolas Gisin. "Experimental entanglement distillation and 'hidden'non-locality". *Nature* 409.6823 (2001), pp. 1014–1017.

[92] Nicholas A Peters, Julio T Barreiro, Michael E Goggin, Tzu-Chieh Wei, and Paul G Kwiat. "Remote state preparation: arbitrary remote control of photon polarization". *Physical review letters* 94.15 (2005), p. 150502.

[93] Marco Ricci, Francesco De Martini, NJ Cerf, R Filip, J Fiurášek, and Chiara Macchiavello. "Experimental purification of single qubits". *Physical review letters* 93.17 (2004), p. 170501.

[94] Daniel E Jones, Brian T Kirby, Gabriele Riccardi, Cristian Antonelli, and Michael Brodsky. "Exploring classical correlations in noise to recover quantum information using local filtering". *New Journal of Physics* 22.7 (2020), p. 073037.

[95] H Gordon Berry, G Gabrielse, and AE Livingston. "Measurement of the Stokes parameters of light". *Applied optics* 16.12 (1977), pp. 3200–3205.

[96] Anders Pors, Michael G Nielsen, and Sergey I Bozhevolnyi. "Plasmonic metagratings for simultaneous determination of Stokes parameters". *Optica* 2.8 (2015), pp. 716–723.

[97] JP Balthasar Mueller, Kristjan Leosson, and Federico Capasso. "Ultracompact metasurface in-line polarimeter". *Optica* 3.1 (2016), pp. 42–47.

[98] Ehsan Arbabi, Seyedeh Mahsa Kamali, Amir Arbabi, and Andrei Faraon. "Full-Stokes imaging polarimetry using dielectric metasurfaces". *Acs Photonics* 5.8 (2018), pp. 3132–3140.

[99] K. Wang, J. G. Titchener, S. S. Kruk, L. Xu, H.-P. Chung, M. Parry, I. I. Kravchenko, Y.-H. Chen, A. S. Solntsev, Y. S. Kivshar, D. N. Neshev, and A. A. Sukhorukov. "Quantum metasurface for multi-photon interference and state reconstruction". *Science* 361 (2018), pp. 1104–1108. DOI: 10.1126/science.aat8196.

[100] T. Stav, A. Faerman, E. Maguid, D. Oren, V. Kleiner, E. Hasman, and M. Segev. "Quantum entanglement of the spin and orbital angular momentum of photons using metamaterials". *Science* 361 (2018), pp. 1101–1104. DOI: 10.1126/science.aat9042.

[101] Leica Microsystems. *Quality as Clear as Glass - Polarizing Microscopy in Glass Production*. 2008. URL: https://www.leica-microsystems.com/science-lab/quality-as-clear-as-glass-polarizing-microscopy-in-glass-production/ (visited on 11/20/2021).

[102] Jürgen Schreiber, Valery Gudelev, and Andrey Smirnov. "New polarization interferometry Approaches for In-situ Process Control and Product Quality Assessment". In: *18th World Conference on Nondestructive Testing*. Vol. 16. 2012, p. 20.

[103] Pallavi Doradla, Karim Alavi, Cecil S Joseph, and Robert H Giles. "Detection of colon cancer by continuous-wave terahertz polarization imaging technique". *Journal of Biomedical Optics* 18.9 (2013), p. 090504.

[104] AN Yaroslavsky, V Neel, and RR Anderson. "Fluorescence polarization imaging for delineating nonmelanoma skin cancers". *Optics letters* 29.17 (2004), pp. 2010–2012.

[105] Zuojia Wang, Feng Cheng, Thomas Winsor, and Yongmin Liu. "Optical chiral metamaterials: a review of the fundamentals, fabrication methods and applications". *Nanotechnology* 27.41 (2016), p. 412001.

[106] Sergei V Zhukovsky, Andrey V Novitsky, and Vladimir M Galynsky. "Elliptical dichroism: operating principle of planar chiral metamaterials". *Optics letters* 34.13 (2009), pp. 1988–1990.

[107] A. Y. Zhu, W. T. Chen, A. Zaidi, Y. W. Huang, M. Khorasaninejad, V. Sanjeev, C. W. Qiu, and F. Capasso. "Giant intrinsic chiro-optical activity in planar dielectric nanostructures". English. *Light-Sci. Appl.* 7 (Feb. 2018), pp. 17158–8. DOI: 10.1038/lsa.2017.158.

[108] Kalyanmoy Deb, Amrit Pratap, Sameer Agarwal, and TAMT Meyarivan. "A fast and elitist multiobjective genetic algorithm: NSGA-II". *IEEE transactions on evolutionary computation* 6.2 (2002), pp. 182–197.

[109] J. Blank and K. Deb. "pymoo: Multi-Objective Optimization in Python". *IEEE Access* 8 (2020), pp. 89497–89509.

[110] Inc. Thorlabs. *Motorized Precision Rotation Mount*. 2021. URL: https://www.thorlabs.com/newgrouppage9.cfm?objectgroup_id=2875 (visited on 10/04/2021).

[111] John Lekner. "Polarization of tightly focused laser beams". *Journal of Optics A: Pure and Applied Optics* 5.1 (2002), p. 6.

[112] Lauren A Warning, Ali Rafiei Miandashti, Lauren A McCarthy, Qingfeng Zhang, Christy F Landes, and Stephan Link. "Nanophotonic approaches for chirality sensing". *ACS nano* 15.10 (2021), pp. 15538–15566.

[113] Mitsuhiro Terakawa, Seiji Takeda, Yuto Tanaka, Go Obara, Tomoya Miyanishi, Tetsuo Sakai, Tetsumi Sumiyoshi, Hitoshi Sekita, Makoto Hasegawa, Pierre Viktorovitch, et al. "Enhanced localized near field and scattered far field for surface nanophotonics applications". *Progress in Quantum Electronics* 36.1 (2012), pp. 194–271.

[114] Ke Chen, Guowen Ding, Guangwei Hu, Zhongwei Jin, Junming Zhao, Yijun Feng, Tian Jiang, Andrea Alù, and Cheng-Wei Qiu. "Directional janus metasurface". *Advanced Materials* 32.2 (2020), p. 1906352.

[115] Augustin Jean Fresnel. *Considérations théoretiques sur la polarisation de la lumiére*. Societé philomathique de Paris, 1829.

[116] E. Plum, X.-X. Liu, V. A. Fedotov, Y. Chen, D. P. Tsai, and N. I. Zheludev. "Metamaterials: Optical Activity without Chirality". *Phys. Rev. Lett.* 102 (11 Mar. 2009), p. 113902. DOI: 10.1103/PhysRevLett.102.113902.

[117] Andriy E. Serebryannikov, Miguel Beruete, Mehmet Mutlu, and Ekmel Ozbay. "Multiband one-way polarization conversion in complementary split-ring resonator based structures by combining chirality and tunneling". *Opt. Express* 23.10 (May 2015), pp. 13517–13529. DOI: 10.1364/OE.23.013517.

[118] E Plum, VA Fedotov, and NI Zheludev. "Optical activity in extrinsically chiral metamaterial". *Applied physics letters* 93.19 (2008), p. 191911.

[119] Benfeng Bai, Yuri Svirko, Jari Turunen, and Tuomas Vallius. "Optical activity in planar chiral metamaterials: Theoretical study". *Physical Review A* 76.2 (2007), p. 023811.

[120] Do-Hoon Kwon, Pingjuan L Werner, and Douglas H Werner. "Optical planar chiral metamaterial designs for strong circular dichroism and polarization rotation". *Optics express* 16.16 (2008), pp. 11802–11807.

[121] Sergey V Golod, Valentin A Seyfi, Anatoly F Buldygin, Alexey E Gayduk, and Victor Ya Prinz. "Large-Area 3D-Printed Chiral Metasurface Composed of Metal Helices". *Advanced Optical Materials* 6.19 (2018), p. 1800424.

[122] TA Raybould, VA Fedotov, N Papasimakis, I Kuprov, IJ Youngs, WT Chen, DP Tsai, and NI Zheludev. "Toroidal circular dichroism". *Physical Review B* 94.3 (2016), p. 035119.

[123] Jiangfeng Zhou, Dibakar Roy Chowdhury, Rongkuo Zhao, Abul K Azad, Hou-Tong Chen, Costas M Soukoulis, Antoinette J Taylor, and John F O'Hara. "Terahertz chiral metamaterials with giant and dynamically tunable optical activity". *Physical Review B* 86.3 (2012), p. 035448.

[124] Sergey Lepeshov and Yuri Kivshar. "Near-field coupling effects in Mie-resonant photonic structures and all-dielectric metasurfaces". *Acs Photonics* 5.7 (2018), pp. 2888–2894.

[125] Andreas E Olk and David A Powell. "Accurate metasurface synthesis incorporating near-field coupling effects". *Physical Review Applied* 11.6 (2019), p. 064007.

[126] Yu Yao, Raji Shankar, Mikhail A Kats, Yi Song, Jing Kong, Marko Loncar, and Federico Capasso. "Electrically tunable metasurface perfect absorbers for ultrathin mid-infrared optical modulators". *Nano letters* 14.11 (2014), pp. 6526–6532.

[127] Andrei Komar, Ramon Paniagua-Dominguez, Andrey Miroshnichenko, Ye Feng Yu, Yuri S Kivshar, Arseniy I Kuznetsov, and Dragomir Neshev. "Dynamic beam switching by liquid crystal tunable dielectric metasurfaces". *ACS Photonics* 5.5 (2018), pp. 1742–1748.

[128] Jin Zhang, Xingzhan Wei, Ivan D Rukhlenko, Hou-Tong Chen, and Weiren Zhu. "Electrically tunable metasurface with independent frequency and amplitude modulations". *ACS Photonics* 7.1 (2019), pp. 265–271.

[129] Khosro Zangeneh Kamali, Lei Xu, Jonathan Ward, Kai Wang, Guixin Li, Andrey E Miroshnichenko, Dragomir Neshev, and Mohsen Rahmani. "Reversible image contrast manipulation with thermally tunable dielectric metasurfaces". *Small* 15.15 (2019), p. 1805142.

[130] Dikla Oren, Maor Mutzafi, Yonina C. Eldar, and Mordechai Segev. "Quantum state tomography with a single measurement setup". *Optica* 4.8 (Aug. 2017), pp. 993–999. DOI: 10.1364/OPTICA.4.000993.

[131] O. Bayraktar, M. Swillo, C. Canalias, and G. Bjork. "Quantum-polarization state tomography". English. *Phys. Rev. A* 94.2 (Aug. 2016), p. 020105. DOI: 10.1103/PhysRevA.94.020105.

[132] James S Fakonas, Anna Mitskovets, and Harry A Atwater. "Path entanglement of surface plasmons". *New Journal of Physics* 17.2 (2015), p. 023002.

[133] N. A. Rubin, A. Zaidi, M. Juhl, R. P. Li, J. P. B. Mueller, R. C. Devlin, K. Leosson, and F. Capasso. "Polarization state generation and measurement with a single metasurface". English. *Opt. Express* 26.17 (Aug. 2018), pp. 21455–21478. DOI: 10.1364/OE.26.021466.

[134] A. Pors, M. G. Nielsen, and S. I. Bozhevolnyi. "Plasmonic metagratings for simultaneous determination of Stokes parameters". *Optica* 2.8 (Aug. 2015), pp. 716–723. DOI: 10.1364/OPTICA.2.000716.

[135] D. F. V. James, P. G. Kwiat, W. J. Munro, and A. G. White. "Measurement of qubits". English. *Phys. Rev. A* 64.5 (Nov. 2001), p. 052312. DOI: 10.1103/PhysRevA.64.052312.

[136] J. G. Titchener, A. S. Solntsev, and A. A. Sukhorukov. "Two-photon tomography using on-chip quantum walks". English. *Opt. Lett.* 41.17 (Sept. 2016), pp. 4079–4082. DOI: 10.1364/OL.41.004079.

[137] D. Oren, M. Mutzafi, Y. C. Eldar, and M. Segev. "Quantum state tomography with a single measurement setup". English. *Optica* 4.8 (Aug. 2017), pp. 993–999. DOI: 10.1364/OPTICA.4.000993.

[138] J. G. Titchener, M. Grafe, R. Heilmann, A. S. Solntsev, A. Szameit, and A. A. Sukhorukov. "Scalable on-chip quantum state tomography". English. *npj Quant. Inform.* 4 (Mar. 2018), p. 19. DOI: 10.1038/s41534-018-0063-5.

[139] M. Ziman. "Process positive-operator-valued measure: A mathematical framework for the description of process tomography experiments". English. *Phys. Rev. A* 77.6 (June 2008), p. 062112. DOI: 10.1103/PhysRevA.77.062112.

[140] P. Kok and B. W. Lovett. *Introduction to Optical Quantum Information Processing*. Cambridge: Cambridge University Press, 2010. ISBN: 9781139193658. DOI: 10.1017/CBO9781139193658.

[141] K. Wang, S. V. Suchkov, J. G. Titchener, A. Szameit, and A. A. Sukhorukov. "Inline detection and reconstruction of multiphoton quantum states". English. *Optica* 6.1 (Jan. 2019), pp. 41–44. DOI: 10.1364/OPTICA.6.000041.

[142] Y. I. Bogdanov, S. P. Kulik, E. V. Moreva, I. V. Tikhonov, and A. K. Gavrichenko. "Optimization of a quantum tomography protocol for polarization qubits". English. *JETP Lett.* 91.12 (June 2010), pp. 686–692. DOI: 10.1134/S0021364010120143.

[143] A. Miranowicz, K. Bartkiewicz, J. Perina, M. Koashi, N. Imoto, and F. Nori. "Optimal two-qubit tomography based on local and global measurements: Maximal robustness against errors as described by condition numbers". English. *Phys. Rev. A* 90.6 (Dec. 2014), pp. 062123–12. DOI: 10.1103/PhysRevA.90.062123.

[144] S. N. Filippov and V. I. Man'ko. "Inverse spin-s portrait and representation of qudit states by single probability vectors". English. *J. Russ. Laser Res.* 31.1 (Jan. 2010), pp. 32–54. DOI: 10.1007/s10946-010-9122-x.

[145] Y. I. Bogdanov, G. Brida, M. Genovese, S. P. Kulik, E. V. Moreva, and A. P. Shurupov. "Statistical Estimation of the Efficiency of Quantum State Tomography Protocols". English. *Phys. Rev. Lett.* 105.1 (July 2010), pp. 010404–4. DOI: 10.1103/PhysRevLett.105.010404.

[146] H. E. Brandt. "Positive operator valued measure in quantum information processing". English. *Am. J. Phys.* 67.5 (Apr. 1999), pp. 434–439. DOI: 10.1119/1.19280.

[147] S. Hamieh, R. Kobes, and H. Zaraket. "Positive-operator-valued measure optimization of classical correlations". English. *Phys. Rev. A* 70.5 (Nov. 2004), p. 052325. DOI: 10.1103/PhysRevA.70.052325.

[148] James G Titchener, Markus Gräfe, René Heilmann, Alexander S Solntsev, Alexander Szameit, and Andrey A Sukhorukov. "Scalable on-chip quantum state tomography". *npj Quantum Information* 4.1 (2018), pp. 1–6.